ฟลูออเรสเซนต์เซ็นเซอร์ชนิดใหม่ที่มีหน่วยรับ 8-แอมิโนควิโนลีน

นางสาวกรรณิการ์ วงษ์นาม

วิทยานิพนธ์นี้เป็นส่วนหนึ่งของการศึกษาตามหลักสูตรปริญญาวิทยาศาสตรดุษฎีบัณฑิต
สาขาวิชาปิโตรเคมี
คณะวิทยาศาสตร์ จุฬาลงกรณ์มหาวิทยาลัย
ปีการศึกษา 2559
ลิขสิทธิ์ของจุฬาลงกรณ์มหาวิทยาลัย

NOVEL FLUORESCENT SENSORS BASED ON 8-AMINOQUINOLINE RECEPTOR

Miss Kunnigar Vongnam

A Dissertation Submitted in Partial Fulfillment of the Requirements

for the Degree of Doctor of Philosophy Program in Petrochemistry

Faculty of Science

Chulalongkorn University

Academic Year 2016

Thesis Title   NOVEL FLUORESCENT SENSORS BASED ON 8-AMINOQUINOLINE RECEPTOR

By   Miss Kunnigar Vongnam

Field of Study   Petrochemistry

Thesis Advisor   Associate Professor Paitoon Rashatasakhon, Ph.D.

Thesis Co-Advisor   Professor Mongkol Sukwattanasinitt, Ph.D.

Accepted by the Faculty of Science, Chulalongkorn University in Partial Fulfillment of the Requirements for the Doctoral Degree

　　　　　　　　　　　　　　　　　　　　　Dean of the Faculty of Science

(Associate Professor Polkit Sangvanich, Ph.D.)

THESIS COMMITTEE

　　　　　　　　　　　　　　　　　　　　　Chairman

(Assistant Professor Warinthorn Chavasiri, Ph.D.)

　　　　　　　　　　　　　　　　　　　　　Thesis Advisor

(Associate Professor Paitoon Rashatasakhon, Ph.D.)

　　　　　　　　　　　　　　　　　　　　　Thesis Co-Advisor

(Professor Mongkol Sukwattanasinitt, Ph.D.)

　　　　　　　　　　　　　　　　　　　　　Examiner

(Numpon Insin, Ph.D.)

　　　　　　　　　　　　　　　　　　　　　Examiner

(Chatr Panithipongwut, Ph.D.)

　　　　　　　　　　　　　　　　　　　　　External Examiner

(Assistant Professor Nantanit Wanichacheva, Ph.D.)

กรรณิการ์ วงษ์นาม : ฟลูออเรสเซนต์เซ็นเซอร์ชนิดใหม่ที่มีหน่วยรับ 8-แอมิโนควิโนลีน (NOVEL FLUORESCENT SENSORS BASED ON 8-AMINOQUINOLINE RECEPTOR) อ.ที่ปรึกษา วิทยานิพนธ์หลัก: ไพฑูรย์ รัชตะสาคร, อ.ที่ปรึกษาวิทยานิพนธ์ร่วม: มงคล สุขวัฒนาสินิทธิ์, 99 หน้า.

การออกแบบและสังเคราะห์อนุพันธ์ของอะมิโดควิโนลีนสองชุด สำหรับการตรวจวัดกลูโคซามีน และไอออนซิงค์ในตัวกลางที่เป็นน้ำ สำหรับการตรวจวัดกลูโคซามีน พัฒนาอนุพันธ์ของอะมิโดควิโนลีน-แน พธาลิไมด์ด้วยการทำปฏิกิริยา 3 ขั้นตอน ได้ผลผลิตร้อยละ 67–73% อนุพันธ์ของอะมิโดควิโนลีน-แนพธาลิ ไมด์ที่ไม่มีหมู่แทนที่และมีหมู่แทนที่เป็นหมู่ไนโตรสามารถตรวจวัดกลูโคซามีนได้อย่างจำเพาะเจาะจง มีการ เพิ่มขึ้นของสัญญาณควอนตัมยิลด์ถึง 14 เท่า ในการศึกษาระดับออร์บิทัลของโมเลกุลที่มีพลังงานต่ำที่สุดที่ ไม่มีอิเล็คตรอนบรรจุอยู่ (LUMO) และออร์บิทัลของโมเลกุลที่มีพลังงานสูงที่สุดที่มีอิเล็คตรอนบรรจุอยู่ (HOMO) โดยเทคนิคลีเนียร์สวีปโวลแทมเมทรี พบว่ากลไกการตรวจวัดกลูโคซามีนเกี่ยวข้องกับการยับยั้ง กระบวนการถ่ายโอนอิเล็กตรอนที่ถูกกระตุ้นด้วยแสง (PET) ระหว่างอะมิโดควิโนลีนและแนพธาลิไมด์โดยกลู โคซามีน มีค่าคงที่ในการจับกัน (K_a) เท่ากับ 1.55x10^4 และ 1.45x10^4 M^{-1} และให้ค่าต่ำสุดที่สามารถ ตรวจวัดได้ (LOD) คือ 1.06 และ 0.29 ไมโครโมลาร์ตามลำดับ นอกจากนี้อนุพันธ์ของอะมิโดควิโนลีน-แน พธาลิไมด์ที่มีหมู่แทนที่เป็นหมู่ไนโตรยังสามารถนำไปตรวจวัดกลูโคซามีนในเซลล์สิ่งมีชีวิต (Caco-2 cells) ได้ ในระดับไมโครโมลาร์อีกด้วย

สำหรับการตรวจวัดไอออนซิงค์ได้พัฒนาชุดของอนุพันธ์อะมิโดควิโนลีนสี่ตัว โดยการขยายระบบ คอนจูเกตบนวงแหวนควิโนลีนร่วมกับหมู่ซาลิไซลอลดิมีนและอะมิโนเมทิลฟีนอล อนุพันธ์อะมิโดควิโนลีนทั้ง สี่ตัวมีความจำเพาะเจาะจงกับไอออนซิงค์แบบเพิ่มสัญญาณฟลูออเรสเซนซ์เนื่องมาจาก chelation-enhanced fluorescence (CHEF) effects ซึ่งเกิดจากการสูญเสียโปรตอนร่วมกับการยับยั้งการเกิดพันธะ ไฮโดรเจนภายในโมเลกุลของฟลูออโรฟอร์ทำให้เกิดกระบวนการถ่ายเทประจุภายในโมเลกุล (ICT) ส่งผลต่อ การคายแสงของซิงค์คอมเพล็กซ์ในช่วงความยาวคลื่นที่ยาวขึ้น การคายแสงของอนุพันธ์อะมิโดควิโนลีนทั้งสี่ ชนิดอยู่ในช่วง 320-390 นาโนเมตร ขึ้นอยู่กับระบบคอนจูเกตภายในโมเลกุล กลไกการเกิดคอมเพล็กซ์ ระหว่างเซ็นเซอร์และไอออนซิงค์สามารถยืนยันโดยวิธีการทางสเปกโทรสโกปี ได้แก่ ^{1}H NMR, MS และ เทคนิคเอกซ์เรย์คริสตอลโลกราฟี (x-ray crystallography) อัตราส่วนในการจับกันเป็น 1:1 ให้ค่าต่ำสุดที่ สามารถตรวจวัดได้ (LOD) อยู่ในช่วง 0.024-0.431 ไมโครโมลาร์ และค่าคงที่ในการจับกันของลิแกนด์กับ ซิงค์ไอออออน อยู่ในช่วง 7.0x 10^3- 1.2x 10^4 M^{-1}

สาขาวิชา ปิโตรเคมี	ลายมือชื่อนิสิต	-------------------------------------
ปีการศึกษา 2559	ลายมือชื่อ อ.ที่ปรึกษาหลัก	-------------------------------------
	ลายมือชื่อ อ.ที่ปรึกษาร่วม	-------------------------------------

5672867623 : MAJOR PETROCHEMISTRY

KEYWORDS: GLUCOSAMINE; ZINC; NAPHTHALIDE; AMINOQUINOLINE; FLUORESCENCE SENSOR; CELL-IMAGING

KUNNIGAR VONGNAM: NOVEL FLUORESCENT SENSORS BASED ON 8-AMINOQUINOLINE RECEPTOR. ADVISOR: ASSOC. PROF. PAITOON RASHATASAKHON, Ph.D., CO-ADVISOR: PROF. MONGKOL SUKWATTANASINITT, Ph.D., 99 pp.

Two series of amidoquinoline-based fluorescent sensors are designed and synthesized for the selective detection of glucosamine and zinc ion in aqueous media. For the glucosamine sensors, three amidoquinoline-naphthalimide dyads are designed and synthesized in 67–73% overall yields in 3 steps from commercially available starting materials. Compounds with unsubstituted and nitro-naphthalimide show excellent selective fluorescent responses towards glucosamine with the enhancement of fluorescence quantum yields by 14 folds. The determination of HOMO-LUMO levels by linear sweep voltammetry suggests that the sensing mechanism likely involves the inhibition of photo-induced electron transfer (PET) between the aminoquinoline and naphthalimide moieties by glucosamine. The association constants of 1.55×10^4 and 1.45×10^4 M^{-1}, along with the glucosamine detection limits of 1.06 and 0.29 µM are determined for unsubstituted and nitro-naphthalimide, respectively. The application of the nitro-naphthalimide derivative as a fluorescent probe for real-time detection of cellular glucosamine at micromolar level in living Caco-2 cells is also demonstrated.

For the zinc ion sensors, four derivatives of 8-amidoquinolines have been successfully synthesized by extension of the p-conjugated system on the quinoline ring and incorporation of either the salicylaldimine or its reduced amino form. All four compounds show selective fluorescence enhancement by zinc (II) ion, attributing to chelation-enhanced fluorescence (CHEF) effects, in which the deprotonation of the amido –NH and phenolic -OH causes the internal charge transfer (ICT) process and results in the bathochromic shift of the emission spectra. The fluorescent signals of the four compound are observed at different wavelengths in the range of 320 to 390 nm depending on the p-conjugated systems. The sensing mechanism is verified by ^{1}H-NMR titration, Mass Spectrometry, and the X-ray crystal structure of the sensor with salicylaldimine and unsubstituted aminoquinoline, which suggests a 1:1 binding stoichiometry between this fluorophore and zinc ion. The detection limits of 0.024 to 0.431 µM and the association constants ranging from 7.0×10^3 to 1.2×10^4 M^{-1} are estimated for the four sensors.

Field of Study: Petrochemistry   Student's Signature ------------------------------

Academic Year: 2016   Advisor's Signature ------------------------------

                                          Co-Advisor's Signature ------------------------------

ACKNOWLEDGEMENTS

CONTENTS

LIST OF FIGURES

จุฬาลงกรณ์มหาวิทยาลัย
CHULALONGKORN UNIVERSITY

LIST OF TABLES

LIST OF SCHEMES

LIST OF ABBREVIATIONS

Ar	aromatic
calcd	calculated
CCA	α-cyano-4-hydroxycinnamic acid
^{13}C NMR	carbon-13 nuclear magnetic resonance
$CDCl_3$	deuterated chloroform
CH_2Cl_2	dichloromethane
CH_3CN	acetronitrile
CV	cyclic voltammetry
DMAP	4-Dimethylaminopyridine
DMSO- d_6	deuterated dimethyl sulfoxide
EDCI	1-Ethyl-3-(3-dimethylaminopropyl)carbodiimide
E_{gap}	energy gaps
E_{ox}	onset oxidation potential
$E_{1/2}$	average of the anodic and cathodic peak potentials
EtOAc	ethyl acetate
ESI-MS	electrospray ionization mass spectrometry
equiv	equivalent (s)
g	gram (s)
HOMO	highest occupied molecular orbital
^{1}H NMR	proton nuclear magnetic resonance
Hz	Hertz
h	hour (s)
J	coupling constant
Ka	Association constant
LUMO	lowest unoccupied molecular orbital
MALDI-TOF MS	matrix assisted laser desorption/ionization-time of flight mass spectrometry
m	multiplet (NMR)

MeOH	methanol
mg	milligram (s)
mL	milliliter (s)
mmol	millimole (s)
Mp	melting point
m/z	mass per charge
M.W.	molecular weight
M	molar
MHz	megahertz
nm	nanomater
rt	room temperature
s	singlet (NMR)
THF	tetrahydrofuran
TLC	thin layer chromatography
UV	ultraviolet
v/v	volume by volume
δ	chemical shift
ε	Molar extinction coefficient
λ	wavelength
°C	degree Celsius
μL	microliter (s)
μM	micromolar (s)
Φ	quantum yield
% yield	percentage yield

CHAPTER I

INTRODUCTION

1.1 Fluorescence

The fluorescence phenomenon is an emission of light from an excited molecule after the absorption of electromagnetic or electrical energy. The fluorescent process is usually described by the Jablonski diagram as shown in Figure 1.1 [1]. After the absorption of light, the molecule will have an unusually high amount of energy and become less stable. This state of molecule is often called "the excited state" which can be visualized as a molecule residing in a higher electronic state (S_1 or S_2 or higher). Consequently, it will release some energy as thermal (heat) or kinetic energy (molecular rotation and vibration) to become the molecule in the lowest vibrational level of S1 state. The release of this first portion of energy is known as "geometrical relaxation" and this process is non-radiative. The release of the remaining portion of energy will be occurred in the form of fluorescence light as the molecule completely return to the ground state (S_0). The difference between the excitation and emission wavelengths is called the Stokes shift which reflects the degree of geometrical relaxation and can be a distinct characteristic of each fluorophore.
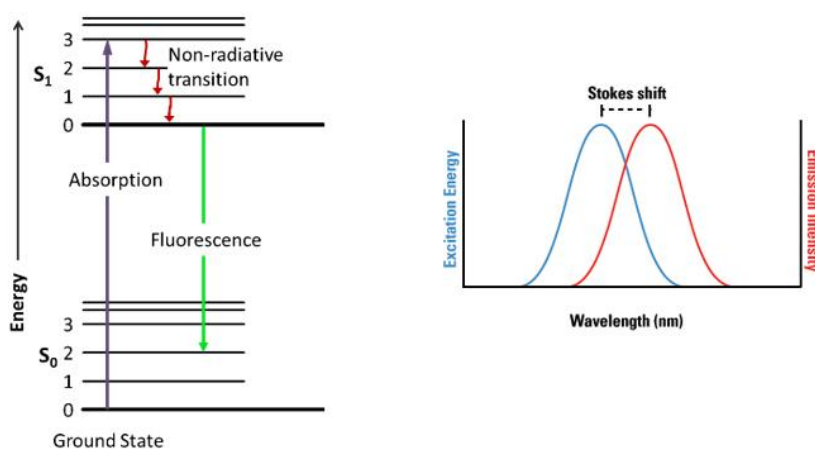
Figure 1.1 Jablonski diagram (left) and the Stokes shift (right)

1.2 Fluorescent chemosensor

Nowadays, fluorescent chemosensors play an important role as detectors in chemical, biological, and environmental fields, for examples, the detection of metal ions in waste water and the monitoring of biological substances in living cells. Fluorescence technique has several advantages over other analytical methods such as high selectivity, high sensitivity, short response time, cost-effective instrumentation, and simple operation. This non-destructive technique is also suitable for analysis of unknown substances in exquisite samples. In general, a fluorescent sensor contains two major components: a fluorophore which serves as a signal transducer, and a binding site or a receptor which function as a selective probe towards the analyte of interest. Upon the interaction or reaction between the receptor and the analyte, the fluorescence signal of the fluorophore will be altered and can be observed from the read out as changes in fluorescence intensities or emission wavelengths.
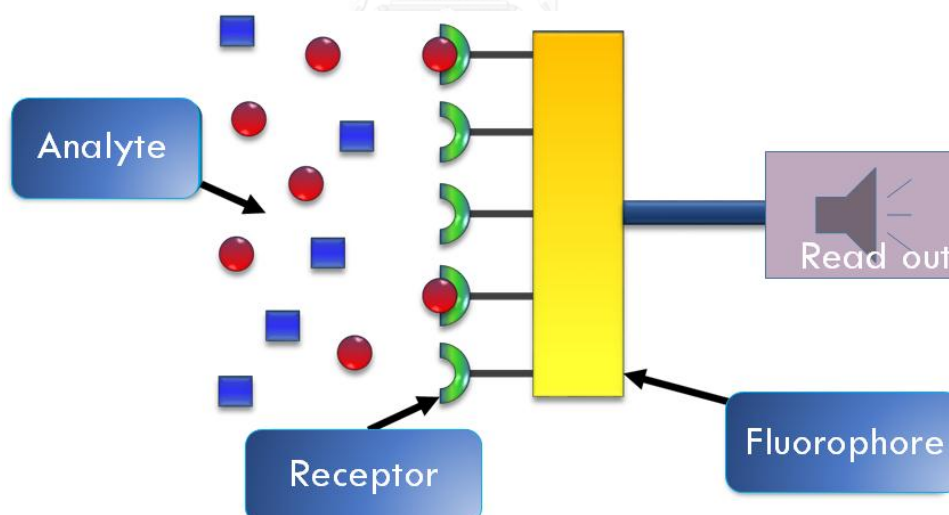
Figure 1.2 The component of fluorescent chemosensors

1.3 Sensing mechanisms

Fluorescent sensors can be designed on the basis of what the interaction between analyte and receptor unit brings about, which could be the photo-induced electron transfer (PET) [2-8], internal charge transfer (ICT) [6-8], fluorescence

resonance energy transfer (FRET) [9, 10], excited-state intramolecular proton transfer (ESIPT) [11, 12], structural isomerization [13], aggregation-induced enhancement fluorescence (AIE) [14, 15] and aggregation-caused quenching (ACQ). In addition, a chemosensor may be designed based on more than one mechanism above in order to enhance sensitivity and selectivity.

- Photo-induced electron transfer (PET) effect

Photo-induced electron transfer (PET) is a well-known cause for fluorescence signal quenching. It can occur when either the HOMO or the LUMO of the analyte or binding site is located between the HOMO-LUMO gap of the fluorophore. For the first case, when an electron of the fluorophore is excited to its LUMO level, one electron from the HOMO the analyte or binding site will be transferred to the singly occupied HOMO level of the fluorophore (Figure 1.3, left). This electron transferring process prohibits the energy release from LUMO to HOMO for the fluorophore, thus weakens the fluorescence intensity. In this scenario, the fluorophore can be considered as the PET-acceptor while the analyte or the binding site behaves as the PET-donor. For the case where the LUMO of the analyte or binding site and the HOMO-LUMO gap of the fluorophore are situated as depicted in Figure 1.3 (right), the empty LUMO functions as a stepping stone for the excited electron. The transferring of excited electron from the LUMO of the fluorophore to the LUMO of the analyte or binging site could facilitate the energy release to the ground state, but the overall process is usually non-radiative. The fluorophore is considered as the PET-donor and the analyte is the PET-acceptor.
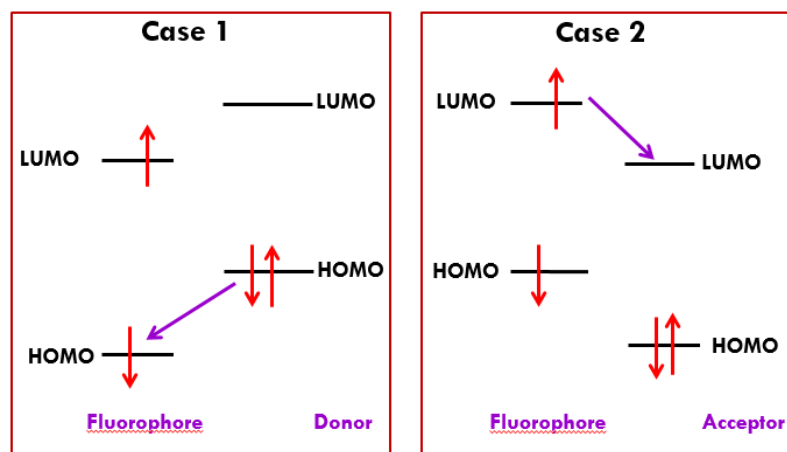
Figure 1.3 Photo-induced electron transfer (PET) effect

- Internal charge transfer (ICT) effect

For molecules containing both electron-donating and electron-withdrawing groups, electrons can delocalize via the pi-conjugated system. The excited molecules at the locally-excited (LE) state can adapt into a more stable state called intramolecular charge-transfer (ICT) state following the Frank-Condon principle (Figure 1.4). Then, the fluorescence intensity will be lower and the molecules show a large Stoke shift because the emission wavelength will be shifted toward longer wavelength as often called "red shift".
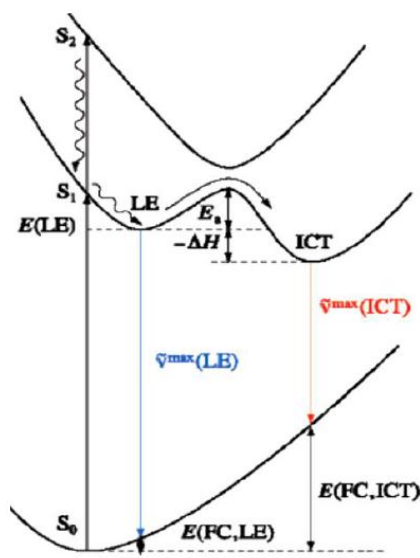
Figure 1.4 Principle of the ICT quenching mechanism

- C=N isomerization process

C=N bond isomerization is a fluorescence quenching mechanism that occurs through the rotation of the double bond. The process occurs after the ground state geometry of the fluorophore is excited to a higher energy level [16, 17]. For the fluorophores with an unbridged double bond structure, the predominant decay processes of the excited fluorophore are often non-fluorescent. On the other hand, their analogs containing covalently bridged double bond structure usually exhibit dramatic increases in fluorescence intensities due to the suppression of double bond isomerization in the excited states as seen in Figure 1.5.
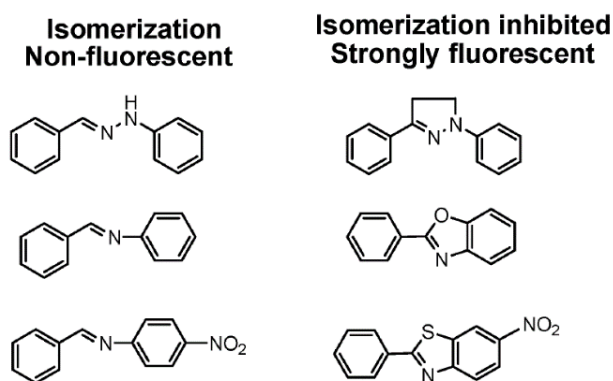
Figure 1.5 Molecular structures of unbridged and bridged C=N compounds [18].

1.4 Fluorescent sensors based on 8-aminoquinoline

8-Aminoquinoline and its derivatives are very important fluorogenic chelators for transition metal ions, especially Cd^{2+} and Zn^{2+}, which are based on either a photo-induced electron transfer (PET) or an internal charge-transfer (ICT) mechanism. Previous works on fluorescent sensors from 8-aminoquinoline derivatives are reviewed below in a chronological order.

An aryl sulfonamide derivative of 8-aminoquinoline (TSQ) was the first introduced by Frederickson et al. in 1987. It is the first zinc-selective fluorescent sensor for imaging Zn^{2+} in biological samples even in the presence of high concentrations of Ca^{2+} and Mg^{2+} [19]. However, TSQ has a poor water-solubility and it is membrane-permeable. To improve the water solubility and membrane permeability, a carboxylic acid or an ester group was introduced into TSQ instead of the 6-methoxyl group to produce chemosensor Zinquin A and Zinquin E, respectively [20].
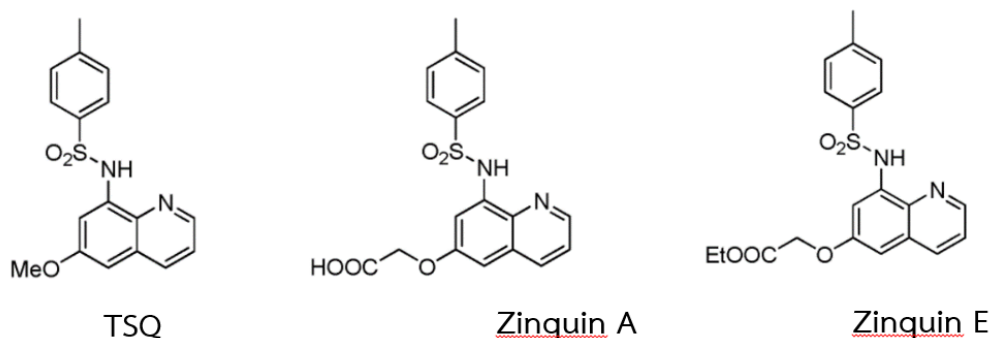
Figure 1.6 Structures of aryl sulfonamide derivatives.

8-Amidoquinoline derivatives has then become one of the most widely used ionophores for Zn^{2+} ion. Probes (**1**-**15**) were designed and synthesized for detection of Zn^{2+} ion [21-35] and the sensitivities and detection limits are tabulated in Table 1.1. In most cases, the intramolecular hydrogen bond of 8-aminoquinoline is broken after binding with Zn^{2+}, and the intramolecular electron-transfer process is prohibited thus enhancing fluorescence emission. Simultaneously, the deprotonation process strengthens the electron-donating ability from the nitrogen atom of the 8-amino group to the quinoline ring and the electron transfer from the nitrogen atom of the heterocycle to the metal ion further enhances the ICT process. As a result, a red-shift in both emission and absorption wavelength could be observed.

The fluorescent sensor based on 8-aminoquinoline bearing the 8-hydroxyquinoline pendant (**14**) and picolylamine (**12**) has the abilities to discriminate cadmium ions from zinc ions. Moreover, the introduction of anthracene fluorophore of sensor **13** was reported for improvement the selectivity toward Zn^{2+} over Cd^{2+} based on ICT and fluorescence resonance energy transfer (FRET).

Besides Zn^{2+}, 8-aminoquinoline derivatives (**16**-**21**) have also been studied as the selective sensors for other metal ions such as Cu^{2+}, Al^{3+}, Cr^{3+} and Hg^{2+} [36-41]. The information on sensing system, solvent media, sensitivity and detection limits are summarized in Table 1.2. Most interestingly, the incorporation of 8-aminoquinoline into graphene oxide (**21**) could lead to a turn-on fluorescent sensor towards glucosamine.

Figure 1.7 Structures of amidoquinoline sensors (**1-21**)

Table 1.1 Summary of some amidoquinoline fluorescent chemosensors for Zn^{2+} detection

Sensor	Testing media	LOD (M)	Φ_F/Φ_{FC} (%)	I/I_0	K_a (M^{-1})	Ref.
1	MeOH/ tris-HCl (10 mM 1:9, v/v, pH 7.22)	-	0.8/6.37	8	6.7×10^6	21
2	MeOH/ tris-HCl (10 mM 1:9, v/v, pH 7.02)	-	18/21	-	9.2×10^5	22
3	10 mM Tris-HCl buffer, pH 7.22.	-	3.2/10.6	3	5.7×10^3	23
4	MeOH/ HEPES (50 mM 1:1, v/v, pH 7.4)	2.8×10^{-8}	-	12	1.8×10^6	24
5	CH_3CN	3.3×10^{-8}	-	-	10.8×10^6	25
6	Tris-HCl, pH 7.22	2.0×10^{-8}	-	-	8.7×10^5	26
7	Ethanol/water (1:1, v/v)	0-2.0 nmol	1.8/8.2	29.5	-	27
8	CH_3CN	-	0.6/7.4	15.7	3.2×10^4	28
9	MeOH/ Tris-HCl (10 mM 4:1, v/v, pH 7.4)	2.56×10^{-7}	-	5	5.2×10^5	35
10	HEPES (10 mM, pH 7.2)	6.6×10^{-8}	-	45.2	5.47×10^4	29
11	CH_3CN/ HEPES (100 mM 1:3, v/v, pH 7.0)	1.3×10^{-7}	-	10	5.9×10^4	30
12	Tris-HCl (50 mM, pH 7.24)	8.85×10^{-8}	-	15	1.4×10^{11}	31
13	MeOH/ Tris-HCl (50 mM 1:9, v/v, pH 7.0)	1.4×10^{-7}	-	5	-	32
15	DMSO/HEPES (10 mM 1:1 v/v, pH 7.4)	3.36×10^{-8}	-	-	1.9×10^4	34

Table 1.2 Summary of some aminoquinoline fluorescent chemosensors for other analytes detection

Sensor	analyte	Testing media	LOD (M)	Φ_F/Φ_{FC} (%)	K_a (M^{-1})	Ref.
14	Cd^{2+}, Zn^{2+}	Ethanol	-	Cd^{2+}: 0.8,16 Zn^{2+}: 0.8,1.9	9.8×10^5 1.8×10^4	33
16	Cu^{2+}	CH_3CN	9×10^{-9}	0.24,4	3.2×10^4	36
17	Cu^{2+}	PBS (10 mM, pH 7.4)	1.44×10^{-7}	-	1.3×10^4	37
18	Cr^{3+}, Al^{3+}	MeOH	1.1×10^{-5} 2.5×10^{-7}	- 0.4,26	- 2.0×10^{10}	38
19	Al^{3+}	DMF	1.0×10^{-6}	-	5.0×10^8	39
20	Hg^{2+}	CH_3CN	1.05×10^{-7}	-	3.2×10^4	40
21	glucosamine	1:1 ethanol–water	5.6×10^{-6}			41

1.5 Glucosamine sensing

Glucosamine is an amino sugar precursor in biosynthesis of glycoaminoglycans – a substance necessary for construction of joint-controlling cartilage [42-44]. It has become the second most popular non-vitamin dietary supplement after fish oil, especially for people with arthritis. The glucosamine level is usually low for most elderlies, and eventual joint deterioration will occur as the result. Some studies found that glucosamine probably reduced osteoarthritis-related pain, improved function in patients with knee or hip osteoarthritis, and reduced stiffness and swelling in the joints [45, 46]. The normal cellular concentration of glucosamine is 1-2 μM, but can reach 10 μM when taken orally. Recently, high concentrations of glucosamine and its derivatives have shown growth inhibitory effects against certain cancers [47-49]
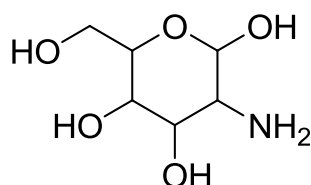
Figure 1.8 Structure of glucosamine

1.5.1 Glucosamine fluorescent sensors

A number of techniques such as high-performance liquid chromatography [50, 51], liquid chromatography [52-56], capillary zone electrophoresis [57, 58], thin layer chromatography [59, 60], spectrophotometry [61], and potentiometry [62] have been used for qualitative and quantitative analysis of glucosamine. Fluorescence spectroscopy has also been a method of choice for analyses of biological samples owing to its high sensitivity and selectivity with simple instrument operation. The selectivity of this method has generally been significantly enhanced by applying appropriate selective sensing probes. Examples of selective fluorescent sensors for glucosamine include boronic acids containing monoaza-18-crown-6 or monoaza-15-crown-5 pendants [63, 64], o-phthalic hemithioacetal functionalized silica [65], amidoquinoline-functionalized graphene oxide [41] , and most recently, a boronic acid containing coumarin aldehyde [66].

In 1997 and 2000, Cooper and James [63, 64] synthesized fluorescent sensors **11a** and **11b** consisting of monoaza-18-crown-6 ether or monoaza-15-crown-5 and boronic acid receptor as a binding site for the ammonium terminal of d-glucosamine hydrochloride, while a boronic acid serves as a binding site for the diol (carbohydrate) part of d-glucosamine hydrochloride. Their fluorescence signals were selectively enhanced by D-glucosamine hydrochloride in ethanol-buffer (1:2, v/v) pH 7.18 with stability constant (K) of 18 and 17 mol dm^{-3}, respectively. The sensing mechanism involved the inhibition of PET process between the anthracene and the aza-crown nitrogen lone pair.
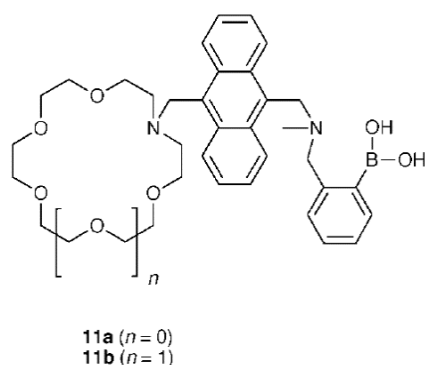
Figure 1.9 Structure of sensor **11a** and **11b**

In 2001, Lin et al. [65] synthesized *o*-phthalic hemithioacetal functionalized silica material (OPTA). Glucosamine can diffuse into the pores and react with the OPTA group to give rise to highly fluorescent isoindole products as depicted in Figure 1.10.
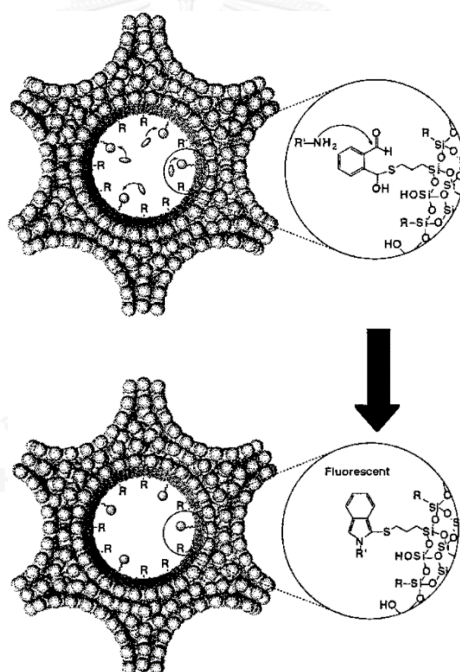
Figure 1.10 The OPTA functionalized mesoporous silica material

Cheng and coworker [41] demonstrated 8-aminoquinoline covalently grafted onto graphene oxide (GAQ) for detection of D-glucosamine with a high sensitivity and selectivity through a photo-induced electron transfer (PET) signaling mechanism. In PET process, aminoquinoline fluorophore acts as an electron acceptor, conversely graphene oxide is an electron donor. A linear response between the amount of D-

glucosamine and the luminescent intensity was obtained with detection limit of 5.6 μM.

Figure 1.11 8-Aminoquinoline functionalized graphene oxide for glucosamine detection

Recently, a new fluorescent chemical sensor based on a boronic acid-containing coumarin aldehyde was reported by Tran and coworker [66] for glucosamine by forming a boronic ester with the sugar diol as well as an iminium ion with the amine group of glucosamine. It showed the strongest binding affinity for glucosamine (K_a= 4100 M^{-1}) compared to other primary amines.
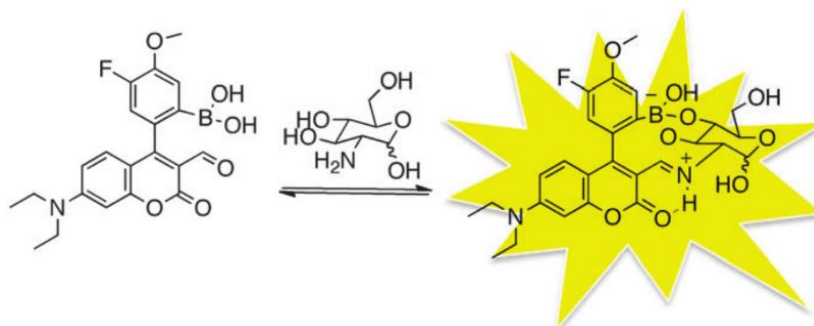
Figure 1.12 A boronic acid-containing coumarin aldehyde sensor for glucosamine.

During our work on development of new fluorescent chemosensors, we also became interested in the photophysical properties of 1,8-naphthalimides due to its highly fluorescent behavior along with excellent thermal and photochemical stabilities. They have been used as optical brighteners [67, 68] and optoelectronic materials [69]. We previously studied the effect of substituent on fluorescence quantum efficiencies for this class of compounds [70] and demonstrated the application of 1,8-naphthalimides as signal transducer in a selective fluorescent sensor for Au(III) ion [71], while others have functionalized this material to become sensors for Cu(II) [72], Hg(II) [73], Cd(II) [74], Zn(II) [75], and trivalent cations [76].

Although naphthalimide and 8-aminoquinoline derivatives are among the most widely studied fluorescent dyes, there are still very few investigations on molecules carrying both fragments [77-80] (Figure 1.13). Therefore, combination of both parts is one of the more attractive targets in the design and their photophysical behavior of the fluorescent sensors.
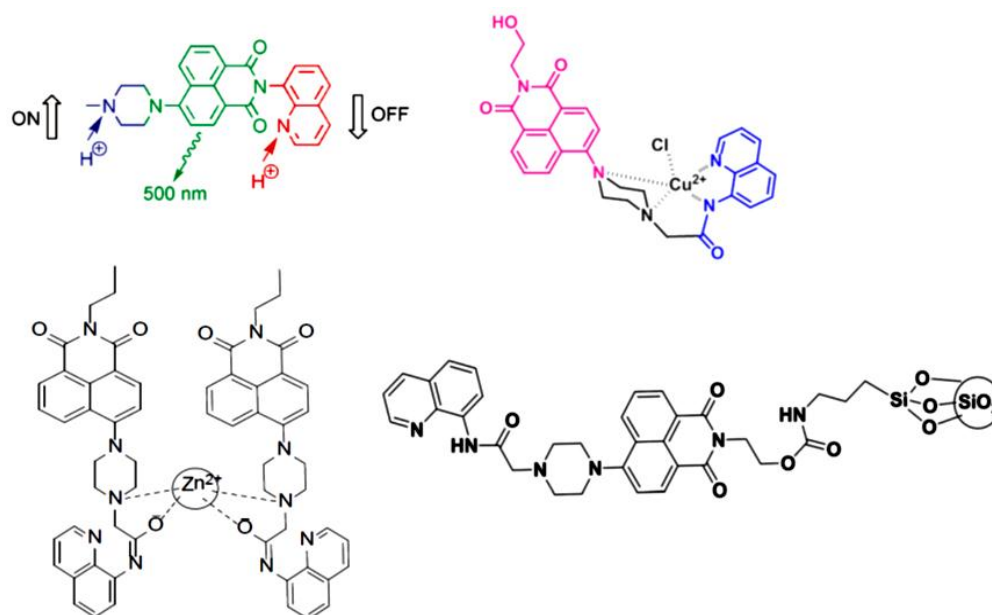
Figure 1.13 Structure of aminoquinoline-naphthalimide analogues

1.5.2 Objectives of this research

In this work, we describe our synthesis of three new amidoquinoline-napthalimide dyads (**A1**–**A3**, Figure 1.14) and demonstrate the selectivities and sensitivities of these compounds towards glucosamine, which will also be compared to the precedent works in this field. In addition, determination of intracellular glucosamine concentration and fluorescent imaging of living cells using one of these compounds will be investigated.
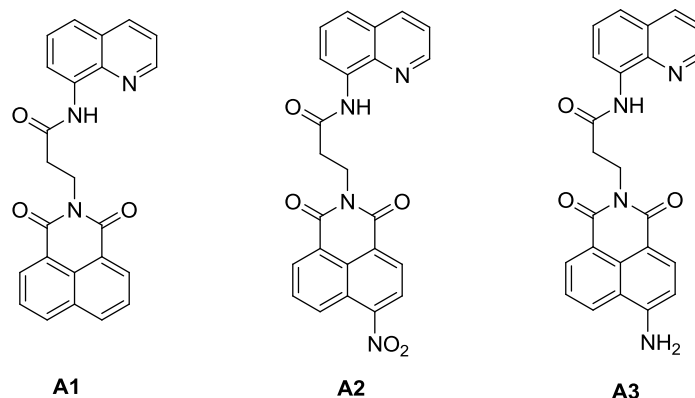
Figure 1.14 Target molecules **A1**-**A3**

1.6 Zinc ion Sensing

Zinc ion is the second most abundant transition metal ions in living organism after iron. It plays crucial roles in many important biological processes like structural and catalytic cofactors, neural signal transmitters or modulators, and regulator of gene expression and apoptosis [81-83]. Moreover, it is known that a disorder of zinc metabolism is closely associated with many severe neurological diseases such as Alzheimer's disease (AD), amyotrophic lateral sclerosis (ALS), Parkinson's disease, hypoxiaischemia and epilepsy [84-86]. In the environment, an excessive concentration of zinc may reduce the soil microbial activity resulting in phytotoxic effect [87, 88]. Therefore, the development of detection methods for metal ions has received considerable attention.

Several analytical techniques such as inductively coupled plasma mass spectroscopy [89], atomic absorption spectroscopy [90], gel electrophoresis [91], and reverse-phase liquid chromatography [92] have been used for the trace-quantity determination of zinc ions. Nevertheless, most of those methods are expensive, complicated operation and time-consuming in practice. Fluorescence spectroscopy has also been a method of choice for analyses of metal ions due to its high sensitivity and selectivity with simple instrument operation. Although a number of fluorescent sensors based on various fluorophores including quinolone [19, 21, 37, 38, 93, 94], fluorescein [95, 96], coumarin [97, 98], naphthalimide [99, 100], BODIPY [101, 102], and others [103, 104] were developed for detection of zinc ions, it is still

desirable to develop new zinc-selective fluorescent sensors with extremely high affinity and good selectivity over other relevant metal ions, especially Cd^{2+}.

1.6.1 Zinc fluorescent sensors

Zhang and coworker [21] reported ratiometric and water-soluble fluorescent Zn^{2+} sensor (AQZ), based on 8-amidoquinoline for detection of Zn^{2+}. It showed 8-fold increase in fluorescence quantum yield along with a red-shift of the emission peak from 440 to 515 nm. The association constant (K_a) was determined of 6.7×10^6 M^{-1} in methanol/water (1:9, v/v pH 7.22) with a mole ratio (AQZ/Zn^{2+}) of 1:1.
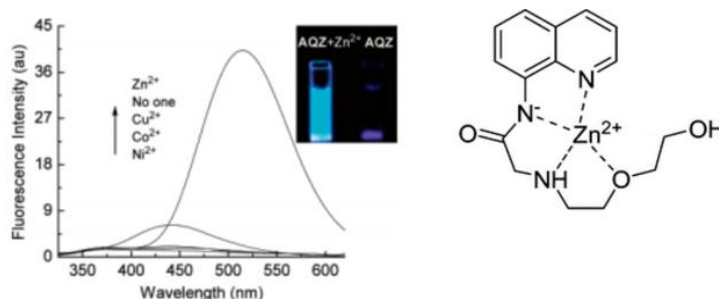
Figure 1.15 Fluorescence spectra of AQZ in the presence of different metal ions.

Moreover, they also designed and synthesized the family of AQZ by varying the substituents onto the quinoline ring for improve their fluorescent properties. It is found that the sensitivity of these sensors for sensing Zn^{2+} was significantly improved by the presence of the electron-donating substituent at the 4-position, AQZ4MO, AQZ4MP, and AQZ4PP. In particular, AQZ4MP showed very high sensitivity for Zn^{2+}. There was an about 220-fold enhancement in the fluorescence quantum yield upon addition of Zn^{2+} based on ICT process.

R = (**AQZ4Cl**) 4-Cl, (**AQZ**) 4-H, (**AQZ4MO**) 4-OCH$_3$, (**AQZ4MP**) 4-morpholino, (**AQZ4PP**) 4-piperidinyl, (**AQZ2MP**) 2-morpholino, (**AQZ5MP**) 5-morpholino
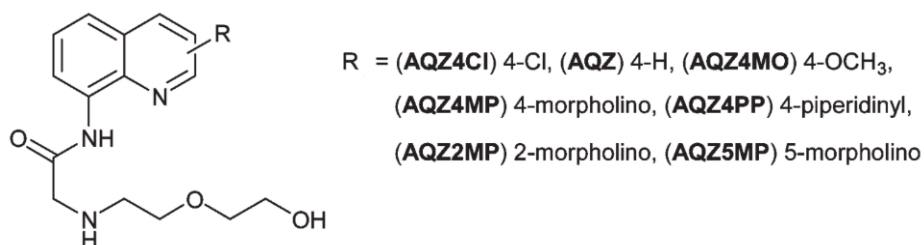
Figure 1.16 The amidoquinoline-based AQZ family.

In addition, Zhu and coworker developed fluorescent Zn^{2+} sensor (DAQZ), which derived from AQZ, by extending π-system of amidoquinoline through an

alkyne group. Based on the zinc-containing [DAQZ@2Zn^{2+}] complex, among common monocarboxylic acids, long-chain dicarboxylic acids and phosphate anions, it specifically responded to the presence of oxalic acid with high sensitivity in aqueous solution.
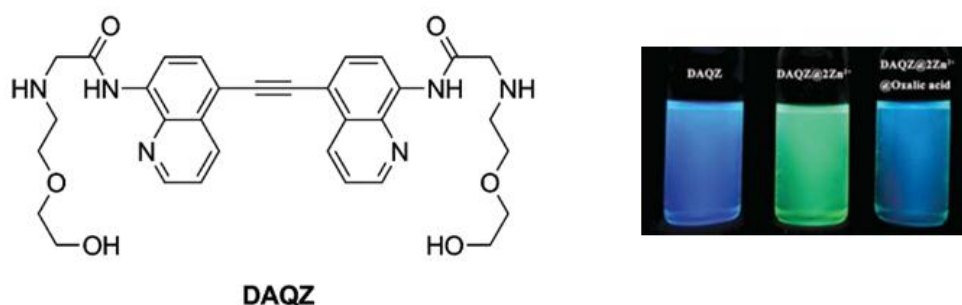
Figure 1.17 Structure of DAQZ and its fluorescent response upon adding Zn^{2+} and oxalic acid, respectively.

8-Amidoquinoline derivatives bearing with picolylamine, dipicolylamine, and anthracene (PMQA, QZn1, and QA, respectively) were also developed as zinc (II) sensors. Upon binding with zinc, PMQA and QZn1 emit bright green fluorescence based on ICT mechanism. On the other hand, green fluorescence from QA-Zn^{2+} complex occurred not only from ICT process, but FRET mechanism also.
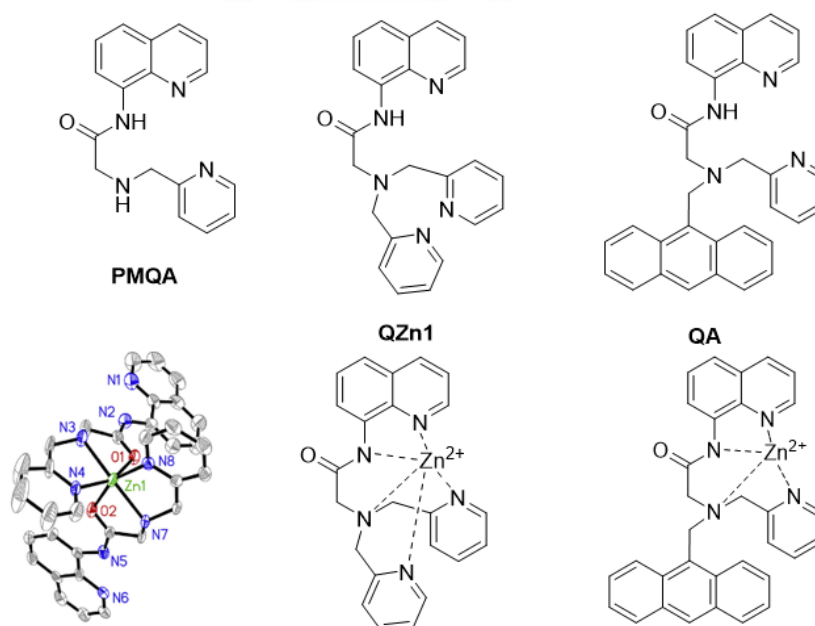
Figure 1.18 Picolyl-aminoquinoline derivatives and their complexes with Zn^{2+}

In 2013, Lee and coworker [105] reported the synthesis of a Zn^{2+} sensor (QP) and investigated compound NA which are closely related to QZn1. Upon addition of Zn^{2+}, the fluorescence of QP and QZn1 are greatly enhanced. When Zn^{2+} is added to NA, no significant change in fluorescence was observed. Thus, the nitrogen in the quinoline ring is important to fluorescence enhancement.
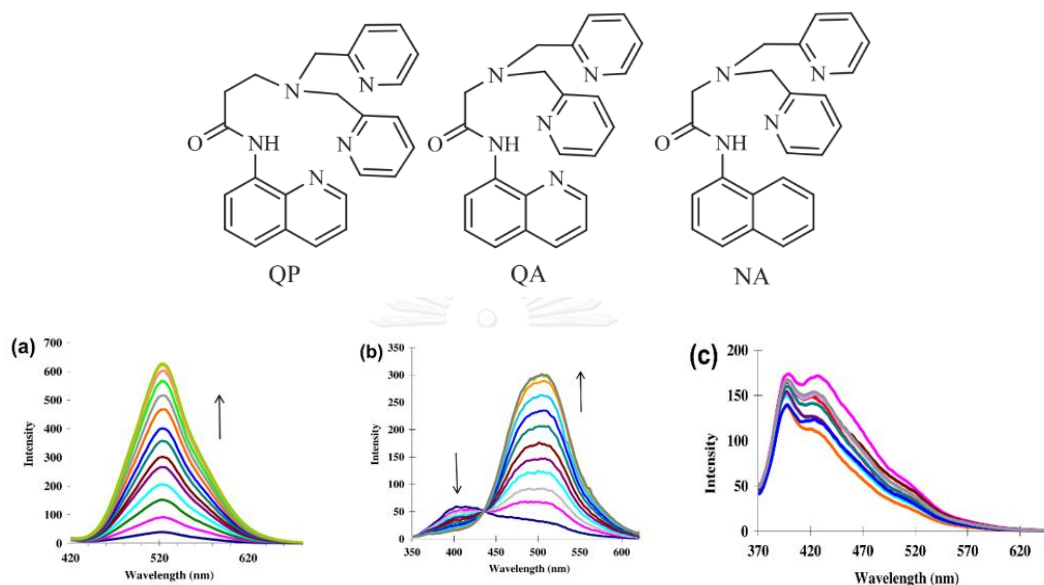
Figure 1.19 Fluorescence response of a) QP, b) QZn1, and c) NA upon gradual addition of Zn^{2+}.

Aminoquinolines based a tripodal receptor TAQ and dipodal receptor NQA were also developed for inducing a large chelation-enhanced fluorescence (CHEF) effect. Coordination of tripodal/dipodal linked nitrogen along with the participation of amide groups along with quinoline moiety that possible forms a semi-rigid cavity which is well arranged for the target zinc ion.
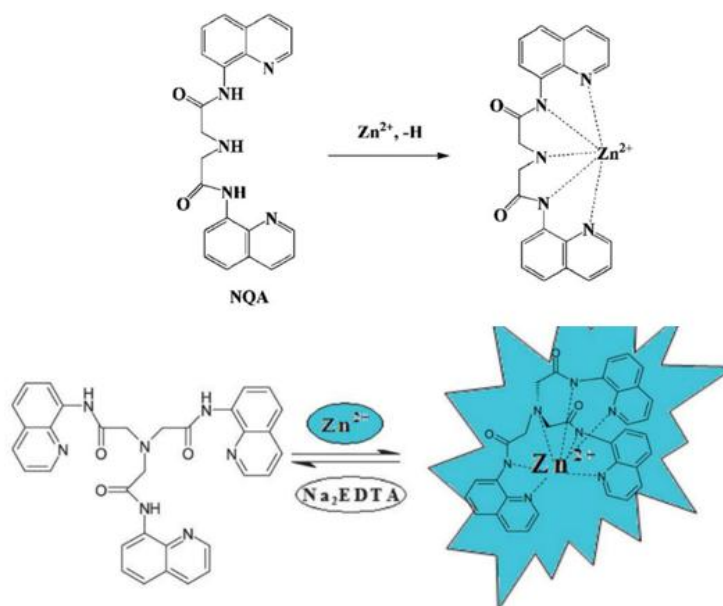
Figure 1.20 Probable Zn^{2+}–Ligand complex binding mode of NAQ and TAQ

8-amidoquinoline derivatives (L1 and HAQT) bearing the *ortho*-aminophenol group as an additional chelating moiety, which showed high sensitivity and selectivity for Zn^{2+} based on an ICT and CHEF mechanism.
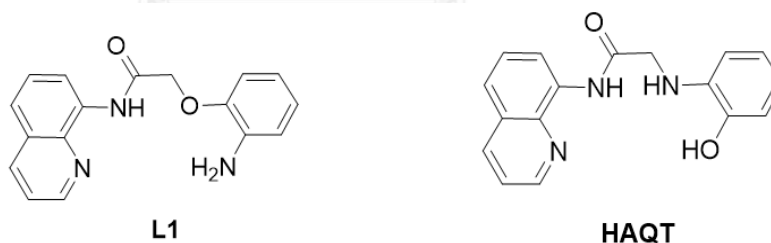
Figure 1.21 Structures of L1 and HAQT

From the literature reviews, it is thus summarized that these amidoquinoline ligands showed high sensitivity and sensitivity toward Zn^{2+} giving remarkably fluorescence turn-on based on the deprotonation of NH amide on 8-amidoquinoline moiety, which increased the electron donating ability of the amine group to the quinoline moiety, then further enhanced the intramolecular charge transfer (ICT) process from the nitrogen atom of heterocycle to the Zn^{2+} ion and thus led to red-shifted emission. In addition, the intramolecular hydrogen bond between the

heterocyclic nitrogen atom and the $-NH_2$ group at 8-substituted group position is interrupted, then allowed fluorescence enhancement as well.

1.6.2 Objectives of this research

For this part of our work, we develop a series of new turn-on fluorescent sensors with high selectivity towards Zn^{2+} ion (F1–F4, Figure 1.22). These compounds bear either a salicylaldimine or its reduced amino-phenol form, and the extended π-conjugation through an aminoarylethynyl group. The structural variation would result in sensors of variously tuned emission wavelengths and the sensitivities towards Zn^{2+} ion.
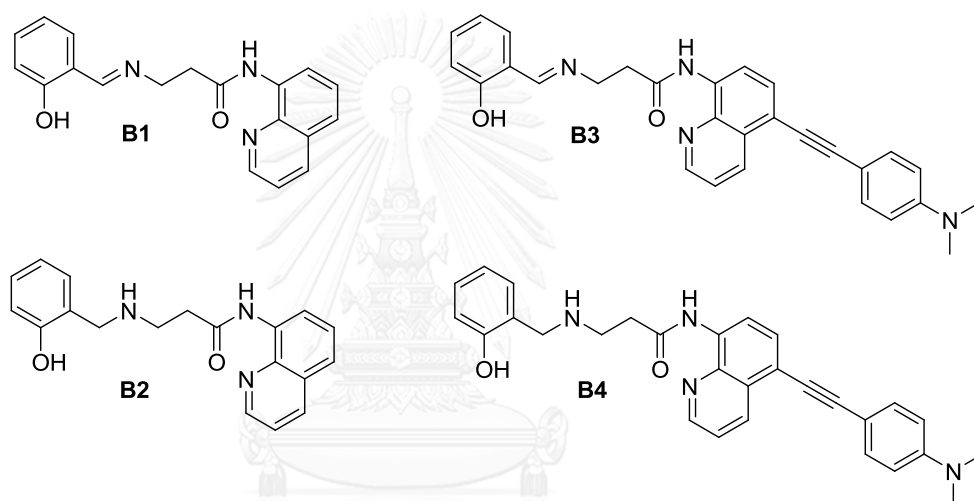
Figure 1.22 Target fluorophores (**B1**-**B4**)

CHAPTER II

EXPERIMENTAL

2.1 Chemicals and materials

All reagents were purchased from Sigma-Aldrich. Metal ions were prepared from their commercially available inorganic salts purchased from Sigma-Aldrich. For most reactions, solvents such as methylene chloride (CH_2Cl_2) and methanol (MeOH) were reagent grade stored over molecular sieves. In anhydrous reactions, solvents such as THF and toluene were dried before use according to the standard procedures. Solvents used for extraction and chromatography such as CH_2Cl_2, hexane, EtOAc and MeOH were commercial grade. Column chromatography was operated using Merck silica gel 60 (70-230 mesh). Thin layer chromatography (TLC) was performed on silica gel plates (Merck F245). Milli-Q water was used in all experiments unless specified otherwise. The most reactions were carried out under positive pressure of N_2 filled in rubber balloons.

2.2 Analytical instruments

Mass spectra were recorded on a Microflex MALDI-TOF mass spectrometer (Bruker Daltonics) using dithanol and α-cyano-4-hydroxycinnamic acid (CCA) as a matrix. As for ESI-Mass, spectra were recorded on electrospray ionization (ESI) Micro mass Quattro Micro API. ^{1}H- and ^{13}C-NMR spectra were acquired from sample solution in $CDCl_3$, DMSO-d_6, and acetone-d_6 on Varian Mercury NMR spectrometer (Varian, USA) at 400 MHz and 100 MHz, respectively. The UV-visible absorption spectra were obtained from a Varian Cary 50 UV-Vis spectrophotometer (Varian, USA) and the fluorescence emission spectra were recorded on a Varian Cary Eclipse spectrofluorometer (Varian, USA). The melting points of all products were acquired from a melting point apparatus (Electrothermal 9100, Fisher Scientific, USA). Elemental (C, H, N) analyses were performed on a PE 2400 series II analyzer (Perkin-Elmer, USA).

2.3 Synthesis of fluorophores

2.3.1 Synthesis of probe **A1**-**A3**

2.3.1.1 tert-butyl 3-oxo-3-(quinolin-8-ylamino)propylcarbamate
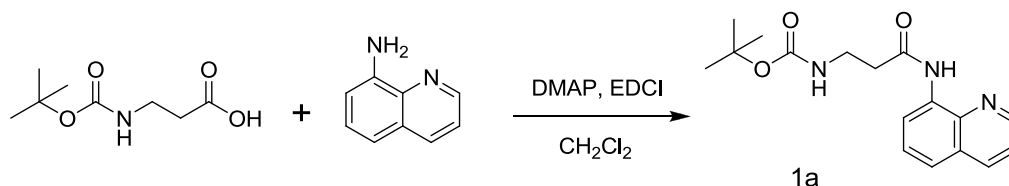
To a slurry mixture of 8-aminoquinoline (1.00 g, 6.94 mmol), DMAP (0.42 g, 3.47 mmol) and CH_2Cl_2 (10 mL) under nitrogen atmosphere chilled in an ice bath for 15 min, Boc-β-Ala-OH (3.94 g, 20.81 mmol) was added. After the mixture was stirred for 2 h, EDCI (3.99 g, 20.81 mmol was added, and the mixture was stirred while the temperature was gradually returned to room temperature for overnight. When reaction completed, the mixture was extracted with CH_2Cl_2 (2 × 20 mL) and washed with saturated $NaHCO_3$ solution. The combined organic phase was dried over anhydrous Na_2SO_4. The crude product after evaporation of solvent was purified by silica gel chromatography using gradient eluents from EtOAc/hexane (1:3) to afford **1a** as a white solid in 91% yield [106].

2.3.1.2 3-amino-N-(quinolin-8-yl) propanamide
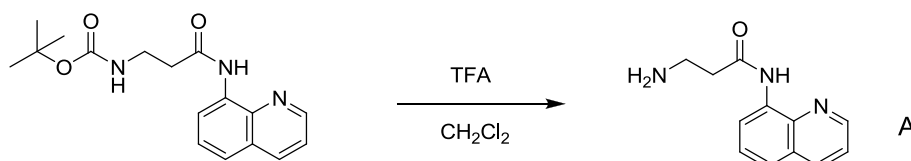
The solution of **1a** (0.15 g, 0.48 mmol) in CH_2Cl_2 (3 mL) was stirred under N_2 atmosphere, then slowly add trifluoroacetic acid 0.5 mL into the solution. After the reaction completed, the mixture was concentrated under reduced pressure. The residue was re-dissolved in CH_2Cl_2 and the solution was sequentially washed with saturated $NaHCO_3$ solution. After drying of the organic solution over anhydrous Na_2SO_4 and evaporation of the solvent, a brown solid was obtained in 92% yield [106].

2.3.1.3 3-(1,3-dioxo-1H-benzo[de]isoquinolin-2(3H)-yl)-N-(quinolin-8-yl)propanamide
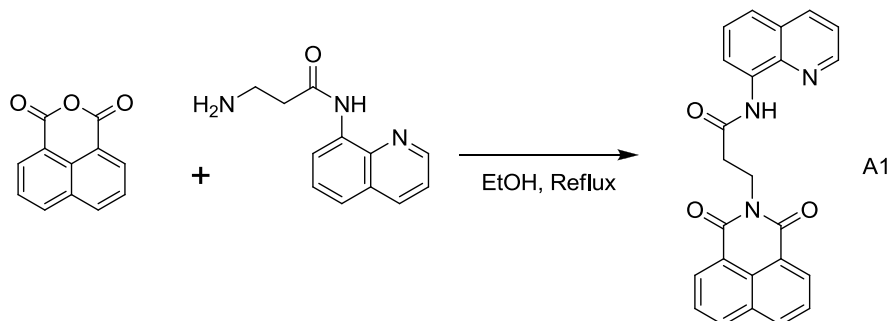
A commercially available 1,8-naphthalic anhydride (0.17 g, 0.87 mmol) and **A** (0.19 g, 0.87 mmol), which was prepared according to the literature report[106], were added into a round bottom flask, then the mixture was heated under refluxing conditions in ethanol for 12 h. After the reaction was allowed to cool to room temperature, the mixture was poured into water and the resulting precipitate was filtered, washed with cool water, and dried to obtain compound **A1** as white crystalline solid (84%). ^{1}H NMR (400 MHz, DMSO) δ 10.18 (s, 1H), 8.72 (d, J = 4.0 Hz, 1H), 8.55 (d, J = 7.4 Hz, 1H), 8.47 (dd, J = 7.2, 4.4 Hz, 4H), 8.37 (d, J = 8.1 Hz, 1H), 7.86 (t, J = 7.8 Hz, 2H), 7.65 (d, J = 8.1 Hz, 1H), 7.61 – 7.51 (m, 2H), 4.43 (t, J = 7.0 Hz, 2H), 2.98 (t, J = 7.2 Hz, 2H). ^{13}C NMR (101 MHz, CDCl$_3$) δ 169.1, 164.1, 147.9, 136.5, 134.3, 134.0, 131.6, 131.3, 128.2, 127.9, 127.5, 126.9, 122.6, 121.51, 121.46, 116.9, 36.8, 36.1. MS (MALDI-TOF) Calcd for C$_{24}$H$_{17}$N$_3$O$_3$: 395.13; Found: 395.62. Elemental Analysis: C, 72.90; H, 4.33; N, 10.63. Found: C, 70.90; H, 4.33; N, 9.63.

2.3.1.4 3-(6-nitro-1,3-dioxo-1H-benzo[de]isoquinolin-2(3H)-yl)-N-(quinolin-8-yl)propanamide
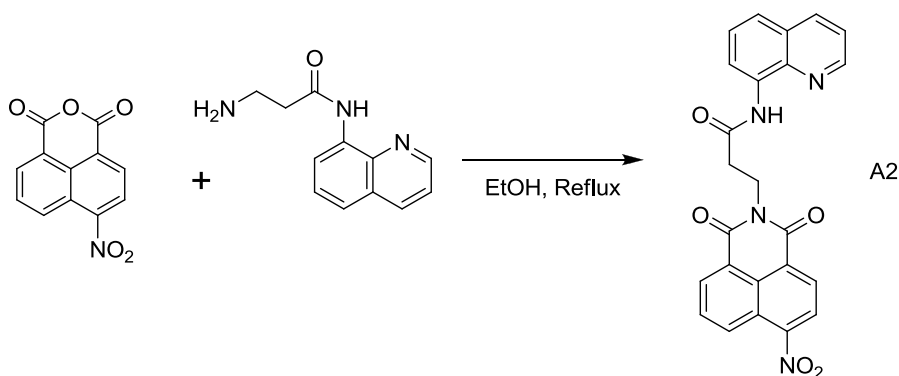
A commercially available 4-nitro-1,8-naphthalic anhydride (0.10 g, 0.41 mmol), **A** (0.09g, 0.41 mmol) and ethanol 3 ml were added into a seal tube, then the mixture was heated under refluxing conditions for 12 h. After the reaction was allowed to cool to room temperature, the mixture was poured into water and the resulting precipitate was filtered, washed with cool water, and dried to obtain **A2** as pale yellow solid (87%). ^{1}H NMR (400 MHz, DMSO) δ 10.17 (s, 1H), 8.72 (dd, J = 8.7, 0.6 Hz, 1H), 8.67 (dd, J = 3.9, 1.2 Hz, 1H), 8.62 (d, J = 7.3 Hz, 1H), 8.60 − 8.51 (m, 3H), 8.37 (d, J = 8.1 Hz, 1H), 8.09 (t, J = 8.0 Hz, 1H), 7.65 (dd, J = 8.4, 0.7 Hz, 1H), 7.60 − 7.52 (m, 2H), 4.44 (t, J = 7.0 Hz, 2H), 2.99 (t, J = 6.9 Hz, 2H). ^{13}C NMR (101 MHz, CDCl3) δ 168.9, 163.2, 162.4, 149.6, 147.3, 132.5, 129.9, 129.4, 129.2, 128.1, 127.9, 126.9, 123.83 123.7, 123.0, 121.8, 121.4, 37.2, 35.8. MS (MALDI-TOF) Calcd for $C_{24}H_{17}N_3O_3$: 440.11; Found: 440.44. Elemental Analysis: C, 65.15; H, 4.10; N, 12.66. Found: C, 65.45; H, 3.66; N, 12.72.

2.3.1.5 3-(6-amino-1,3-dioxo-1H-benzo[de]isoquinolin-2(3H)-yl)-N-(quinolin-8-yl)propanamide (3)
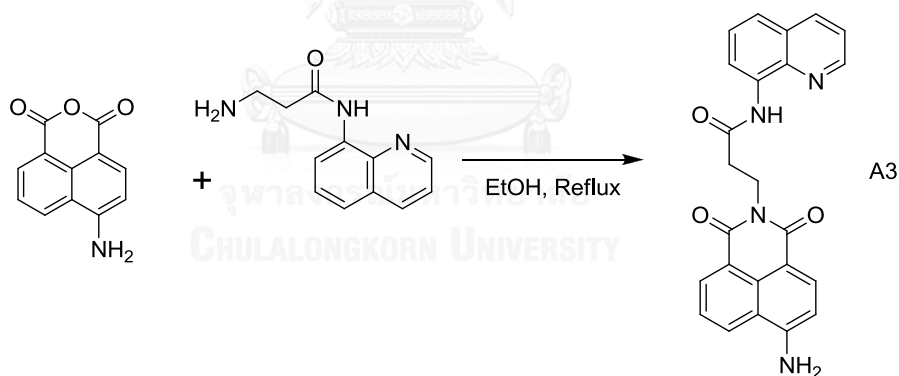
A commercially available 4-amino-1,8-naphthalic anhydride (0.10 g, 0.47 mmol), **A** (0.10 g, 0.47 mmol) and ethanol 3 ml were added into a seal tube, then the mixture was heated under refluxing conditions for 12 h. After the reaction was allowed to cool to room temperature, the mixture was poured into water and the resulting precipitate was filtered, washed with cool water, and dried to obtain **A3** as yellow solid (81%). ^{1}H NMR (400 MHz, DMSO) δ 10.16 (s, 1H), 8.79 (d, J = 4.1 Hz, 1H), 8.63 (d, J = 8.3 Hz, 1H), 8.58 (d, J = 7.3 Hz, 1H), 8.42 (d, J = 7.3 Hz, 1H), 8.39 (d, J = 8.1 Hz, 1H), 8.19 (d, J = 8.3 Hz, 1H), 7.66 (t, J = 8.0 Hz, 2H), 7.62 − 7.56 (m, 2H), 7.47 (s, 2H), 6.85 (d, J = 8.4 Hz, 1H), 4.39 (t, J = 7.4 Hz, 2H), 2.94 (t, J = 7.4 Hz, 2H). ^{13}C NMR

(101 MHz, DMSO) δ 169.6, 163.8, 162.8, 152.7, 148.7, 138.1, 136.5, 134.5, 133.9, 131.0, 129.8, 129.3, 127.8, 126.9, 124.0, 122.0, 121.9, 121.8, 119.4, 116.9, 108.2, 107.6, 36.0, 35.4. MS (MALDI-TOF) Calcd for $C_{24}H_{17}N_3O_3$: 410.14; Found: 410.42. Elemental Analysis: C, 70.23; H, 4.42; N, 13.65. Found: C, 70.88; H, 4.72; N, 13.87.

2.3.2 Synthesis of **B1**-**B4**

2.3.2.1 (E)-3-(2-hydroxybenzylideneamino)-N-(quinolin-8-yl) propanamide
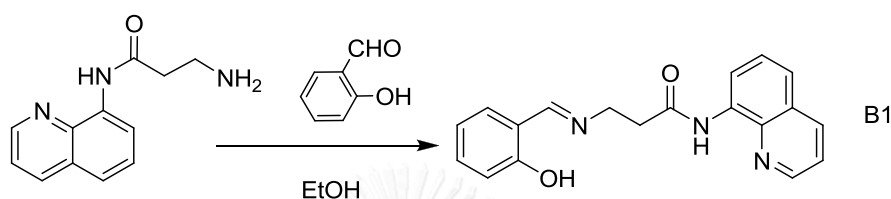
A mixture of 2-hydroxybenzaldehyde (0.14 g, 1.16 mmol) and **A** (0.30 g, 1.39 mmol) in 3 mL ethanol was refluxed for 3 hours. After cooling the reaction, the yellow precipitate was obtained then filtered and washed several time with cold ethanol to yield **B1** as a bright yellow solid in 87%. ^{1}H NMR (400 MHz, acetone) δ 13.19 (s, 1H), 10.01 (s, 1H), 8.88 – 8.71 (m, 2H), 8.64 (s, 1H), 8.34 (dd, *J* = 8.3, 1.6 Hz, 1H), 7.64 – 7.53 (m, 2H), 7.40 (dd, *J* = 7.6, 1.5 Hz, 1H), 7.34 – 7.23 (m, 1H), 6.91 – 6.77 (m, 2H), 4.07 (t, *J* = 6.1 Hz, 2H), 3.09 (t, *J* = 6.5 Hz, 2H). ^{13}C NMR (101 MHz, CDCl₃) δ 169.2, 166.5, 161.1, 148.2, 138.3, 136.3, 134.3, 132.3, 131.5, 127.9, 127.3, 121.64, 121.61, 118.8, 118.6, 116.9, 116.6, 55.4, 38.9. Elemental Analysis: C, 71.46; H, 5.37; N, 13.16. Found: C, 70.39; H, 5.33; N, 12.90.

2.3.2.2 3-(2-hydroxybenzylamino)-N-(quinolin-8-yl)propanamide
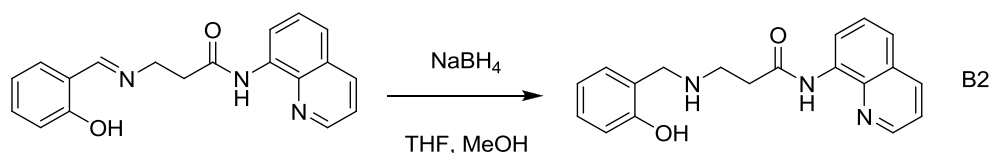
B1 (0.10 g, 0.31 mmol) in mixed solvent, methanol and tetrahydrofuran, was reduced by using NaBH₄ (0.12 g, 3.13 mmol). The mixture was stirred at room temperature for overnight, then mixture was concentrated under reduced pressure. the mixture was extracted with CH₂Cl₂ (2 × 20 mL) and DI water. Organic solution was dried over anhydrous Na₂SO₄ and evaporated to achieved a brown solid (**B2**) in 82%

yield. ^{1}H NMR (400 MHz, CDCl$_3$) δ 9.86 (s, 1H), 8.80 (d, J = 3.4 Hz, 1H), 8.73 (d, J = 6.3 Hz, 1H), 8.15 (d, J = 8.2 Hz, 1H), 7.56 – 7.49 (m, 2H), 7.45 (dd, J = 8.2, 4.2 Hz, 1H), 7.16 (t, J = 7.6 Hz, 1H), 7.01 (d, J = 7.3 Hz, 1H), 6.83 (d, J = 8.0 Hz, 1H), 6.78 (t, J = 7.4 Hz, 1H), 4.06 (s, 2H), 3.09 (t, J = 5.9 Hz, 2H), 2.81 (dd, J = 12.0, 6.2 Hz, 2H). ^{13}C NMR (101 MHz, CDCl$_3$) δ 169.1, 157.2, 147.2, 137.3, 135.4, 133.2, 127.7, 127.5, 127.0, 126.3, 121.4, 120.8, 120.7, 118.0, 115.6, 115.4, 51.5, 43.1, 35.8. Elemental Analysis: C, 71.01; H, 5.96; N, 13.08. Found: C, 70.87; H, 5.90; N, 12.74.

2.3.2.3 5-iodoquinolin-8-amine
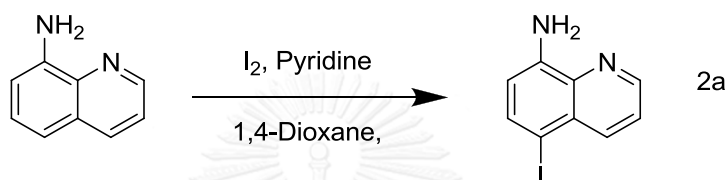
The 8-aminoquinoline (0.72 g, 4.99 mmol) was dissolved in dioxane (30 mL) and pyridine (30 mL) and the solution was cooled to 0 $^{\circ}$C. The first one portion of iodine (1.90 g, 15 mmol) was added. The solution progressively took a dark brown color. After 1 h, the ice bath was removed and a supplementary portion of iodine (630 mg, 5 mmol) was added. The solution was further stirred for one hour at room temperature. A saturated solution of sodium thiosulfate was then added until the brown color disappeared. The mixture was extracted with dichloromethane and washed with water. After evaporation, the product was filtered through a short plug of silica, eluted with the dichloromethane/hexane (3:1, v/v) to afford 5-iodoquinolin-8-amine (85%) [22].

2.3.2.4 tert-butyl 3-(5-iodoquinolin-8-ylamino)-3-oxopropylcarbamate
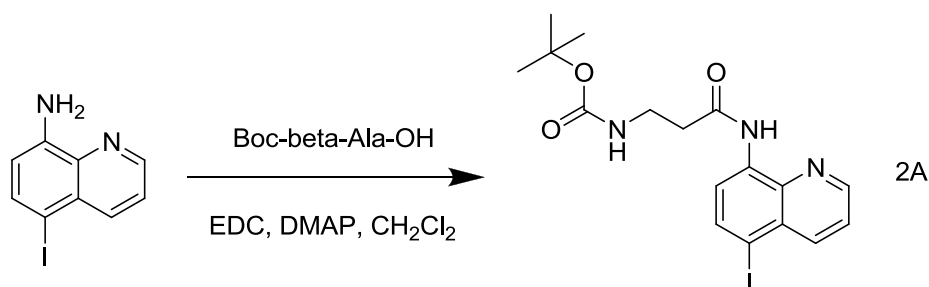
To a slurry mixture of 5-iodo-8-aminoquinoline (0.20 g, 0.74 mmol), DMAP (45 mg, 0.37 mmol) and CH$_2$Cl$_2$ (5 mL) under nitrogen atmosphere chilled in an ice bath for 15 min, Boc-beta-Ala-OH (0.42 g, 2.22 mmol) was added. After the mixture was

stirred for 2 h, EDC (0.43 g, 2.22 mmol was added, and the mixture was further stirred while the temperature was gradually returned to room temperature for overnight. When reaction completed, the mixture was extracted with CH_2Cl_2 (2 × 20 mL) and washed with saturated $NaHCO_3$ solution. The combined organic phase was dried over anhydrous Na_2SO_4. The crude product after evaporation of solvent was purified by silica gel chromatography using gradient eluents from EtOAc/hexane (1:3) to afford **2A** as a white solid in 91% yield ^{1}H NMR (400 MHz, acetone) δ 10.01 (s, 1H), 8.90 (d, *J* = 2.9 Hz, 1H), 8.60 (d, *J* = 8.3 Hz, 1H), 8.43 (d, *J* = 8.6 Hz, 1H), 8.18 (d, *J* = 8.3 Hz, 1H), 7.75 (dd, *J* = 8.5, 4.2 Hz, 1H), 6.11 (s, 1H), 3.50 (dd, *J* = 12.7, 6.4 Hz, 2H), 2.86 (t, *J* = 5.7 Hz, 2H), 1.39 (s, 9H). ^{13}C NMR (101 MHz, Acetone) δ 171.0, 150.2, 141.2, 139.8, 139.1, 137.0, 130.4, 124.6, 118.40, 118.36, 89.1, 38.5, 37.7, 28.6.

2.3.2.5 Tert-butyl 3-(5-((4-(dimethylamino) phenyl)ethynyl)quinolin-8-ylamino)-3-oxopropylcarbamate
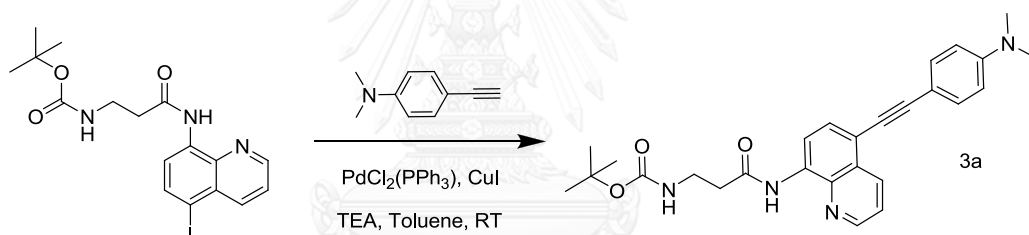
A mixture of **2A** (0.2 g, 0.45 mmol), 4-ethynyl-N,N-dimethylaniline (0.13 g, 0.91 mmol), $PdCl_2(PPh_3)_2$ (32 mg, 0.045 mmol), CuI (8 mg, 0.045 mmol) and triethylamine (1 mL) in toluene (2 mL) was stirred at room temperature under nitrogen atmosphere for 4 h. After reaction completed, the mixture was then work-up by using EtOAc (25 ml x 3) and washed with saturated NH_4Cl solution. The combined organic phase was dried over anhydrous Na_2SO_4. The crude product after evaporation of solvent was purified by silica gel chromatography using gradient eluents from EtOAc/hexane (1:3) to afford **3a** as an orange solid in 84% yield. ^{1}H NMR (400 MHz, acetone) δ 10.02 (s, 1H), 8.93 (d, *J* = 4.2 Hz, 1H), 8.80 (d, *J* = 8.4 Hz, 1H), 8.77 (d, *J* = 8.2 Hz, 1H), 7.76 (d, *J* = 8.1 Hz, 1H), 7.72 (dd, *J* = 8.4, 4.2 Hz, 1H), 7.50 (d, *J* = 8.9 Hz, 2H), 6.78 (d, *J* = 8.9 Hz, 2H), 6.12 (s, 1H), 3.50 (dd, *J* = 12.5, 6.3 Hz, 2H), 3.02 (s, 6H), 2.86 (t, *J* = 6.5 Hz, 2H), 1.38 (s, 9H). ^{13}C NMR (101 MHz, Acetone) δ 171.0, 151.8, 149.9, 139.1, 135.8, 133.5, 131.3, 128.8, 123.4, 116.7, 112.8, 110.5, 96.5, 84.9, 40.2, 38.5, 37.8, 28.6.

2.3.2.6 3-amino-N-(5-((4-(dimethylamino) phenyl) ethynyl) quinolin-8-yl)propanamide
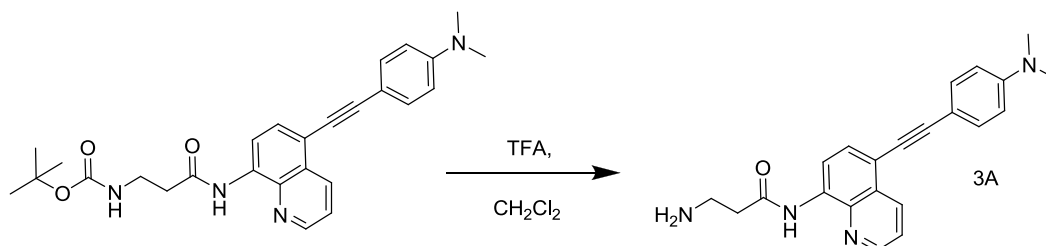
A solution of **3a** (0.16 g, 0.35 mmol) in CH_2Cl_2 (3 mL) was stirred under N_2 atmosphere, then slowly add trifluoroacetic acid (1 mL) into the solution. After the reaction completed, the mixture was concentrated under reduced pressure. The residue was re-dissolved in CH_2Cl_2 and the solution was sequentially washed with saturated $NaHCO_3$ solution. After drying of the organic solution over anhydrous Na_2SO_4 and evaporation of the solvent, **3A** was obtained as a yellow solid. ^{1}H NMR (400 MHz, acetone) δ 11.30 (s, 1H), 8.94 (d, *J* = 4.1 Hz, 1H), 8.84 (d, *J* = 8.1 Hz, 1H), 8.78 (d, *J* = 8.5 Hz, 1H), 7.75 (d, *J* = 8.1 Hz, 1H), 7.70 (dd, *J* = 8.4, 4.2 Hz, 1H), 7.50 (d, *J* = 8.9 Hz, 2H), 6.78 (d, *J* = 8.8 Hz, 2H), 3.59 (t, 2H), 3.02 (s, 6H), 2.80 (t, 2H). ^{13}C NMR (101 MHz, Acetone) δ 172.1, 151.5, 149.6, 149.5, 135.6, 133.4, 131.4, 128.9, 123.2, 117.0, 116.7, 112.8, 110.5, 96.2, 84.9, 47.7, 40.2, 40.0, 38.9, 38.6.

2.3.2.7 (E)-N-(5-((4-(dimethylamino) phenyl) ethynyl) quinolin-8-yl)-3-(2-hydroxybenzylideneamino)propanamide
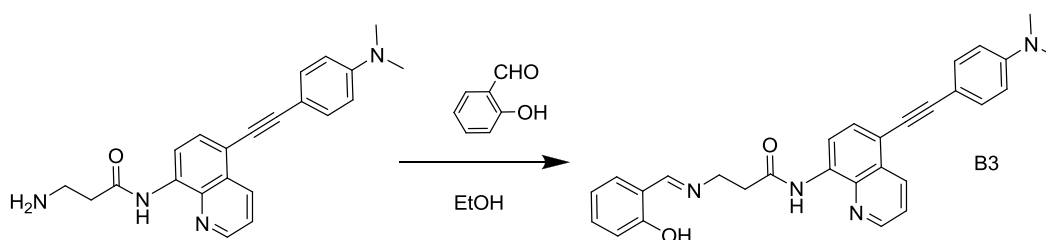
A mixture of 2-hydroxybenzaldehyde (0.044 g, 0.36 mmol) and **3A** (0.13g, 0.36 mmol) in 3 mL ethanol was refluxed for 3 hours. After cooling the reaction, the yellow precipitate was obtained then filtered and washed several time with cold ethanol to yield **B3** as a bright yellow solid in 87%. ^{1}H NMR (400 MHz, DMSO) δ 13.31 (s, 1H), 10.34 (s, 1H), 8.94 (s, 1H), 8.72 (d, *J* = 8.0 Hz, 1H), 8.65 (s, 2H), 7.77 (d, *J* = 7.3

Hz, 2H), 7.51 – 7.40 (m, 3H), 7.30 (t, J = 7.7 Hz, 1H), 6.88 (t, J = 7.8 Hz, 1H), 6.83 (d, J = 7.6 Hz, 1H), 6.75 (d, J = 7.5 Hz, 2H), 3.95 (t, J = 6.5 Hz, 2H), 3.04 (t, 2H), 2.98 (s, 6H). ^{13}C NMR (101 MHz, DMSO) δ 170.1, 166.4, 160.5, 150.3, 149.2, 137.9, 134.7, 134.6, 132.5, 132.3, 131.6, 130.3, 127.5, 122.9, 118.7, 118.5, 116.4, 114.9, 111.9, 108.4, 95.7, 84.2, 54.5, 37.8. Elemental Analysis: C, 75.30; H, 5.67; N, 12.11. Found: C, 74.85; H, 5.66; N, 11.60.

2.3.2.8 N-(5-((4-(dimethylamino) phenyl) ethynyl) quinolin-8-yl)-3-(2-hydroxybenzylamino)propanamide
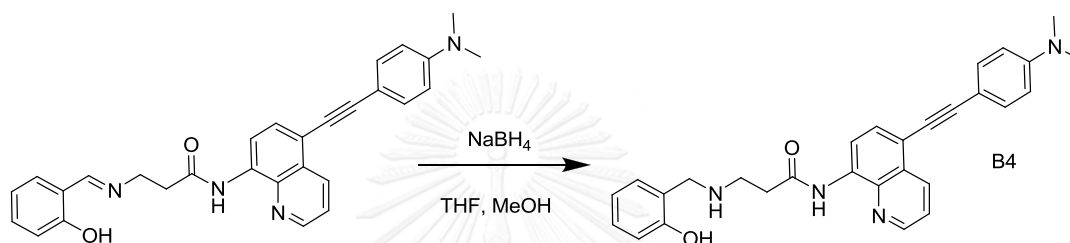
B3 (0.10 g, 0.22 mmol) in mixed solvent, methanol and tetrahydrofuran, was reduced by using NaBH$_4$ (82 mg, 2.16 mmol). The mixture was stirred at room temperature for overnight, then mixture was concentrated under reduced pressure. Crude was extracted with CH$_2$Cl$_2$ (2 × 20 mL) and DI water. Organic solution was dried over anhydrous Na$_2$SO$_4$ and evaporated to achieved a yellow solid (**B4**) in 89% yield ^{1}H NMR (400 MHz, DMSO) δ 11.05 (s, 1H), 8.89 (d, J = 4.2 Hz, 1H), 8.71 (d, J = 8.5 Hz, 1H), 8.67 (d, J = 8.2 Hz, 1H), 7.81 – 7.71 (m, 2H), 7.49 (d, J = 8.7 Hz, 2H), 7.23 (d, J = 6.9 Hz, 1H), 7.05 (t, J = 6.8 Hz, 1H), 6.80 – 6.67 (m, 4H), 3.85 (s, 2H), 2.98 (s, 6H), 2.89 (t, J = 5.9 Hz, 2H), 2.73 (t, J = 6.0 Hz, 2H). ^{13}C NMR (101 MHz, DMSO) δ 171.18, 156.47, 150.25, 149.16, 137.97, 135.03, 134.59, 132.49, 130.39, 128.81, 127.66, 127.53, 124.96, 122.80, 118.50, 116.24, 115.11, 114.59, 111.90, 108.39, 95.58, 84.18, 49.40, 44.57, 36.90.

2.4 Photophysical property study

2.4.1 UV-Visible spectroscopy

The stock solution of fluorophores were prepared with concentration of 1.0 mM. The UV-Visible absorption spectra of the stock solutions of fluorophores were recorded from 200 to 600 nm at ambient temperature.

2.4.1.1 Molar extinction coefficient (ε)

The molar extinction coefficient (ε) of each fluorophore were calculated from the UV absorption spectra in DMSO for the naphthalimide-aminoquinoline sensors and in CH_3CN for amidoquinolines sensors at various concentrations. The absorption intensity of maximum wavelengths (A) of each compound was plotted against the concentrations (C) at the respective excitation wavelengths. Each plot should be a straight line goes through origin-point. The molar extinction coefficient (ε) represented into the following equation:

$$A = \varepsilon bC$$

*b is the cell path length.

2.4.2 Fluorescence spectroscopy

The stock solution of fluorophores were diluted to 20 μM. The emission spectra of fluorophores were recorded at ambient temperature using an excitation wavelength of each fluorophore.

2.4.2.1 Fluorescence quantum yield (Φ_F)

The fluorescence quantum yield of **A1**-**A3** were performed in CH_3CN by using 2-amino pyridine (Φ_F = 0.60) in 0.1 M H_2SO_4 for **A1** and **A2** and quinine sulphate (Φ_F = 0.54) in 0.1 M H_2SO_4 for **A3** as references. For Zn^{2+} selective fluorophores, their fluorescence quantum yield were determined in EtOH by using quinine sulphate (Φ_F = 0.54) in 0.1 M H_2SO_4 as references. The UV-visible absorption spectra of fluorophores that maximum intensity should never be above 0.1 were recorded at varied concentrations. The fluorescence spectra of the same concentration using appropriate excitation wavelengths selected were recorded based on the absorption maximum wavelength (λ_{max}) of each compound. The integrated fluorescence

intensities were plotted versus the absorbance at the respective excitation wavelengths. Each plot should be a straight line with 1 intercept. In addition, the fluorescent quantum yield (Φ_F) was obtained from graph of integrated fluorescence intensity *vs* absorbance represented into the following equation:

$$\Phi_X = \Phi_{ST}\left(\frac{Grad_X}{Grad_{ST}}\right)\left(\frac{\eta_X^2}{\eta_{ST}^2}\right)$$

Φ_{ST} is the fluorescence quantum yield of a standard reference and Φ_X is the fluorescence quantum yield of sample. η_X is the refractive index of that solvent and η_{ST} is the refractive index of the standard reference.

2.5 Fluorescent sensor study

2.5.1 Glucosamine sensing

2.5.1.1 Selectivity screening

Glucosamine and various ions/molecules including: (1) myoglobin, (2) papain, (3) histone, (4) BSA, (5) lipase, (6) hemoglobin, (7) Human Serum Albumin, (8) risozyme, (9) cysteine, (10) glycine, (11) glucose, (12) sucrose, (13) caffeine, (14) ethanolamine, (15) Na^+, (16) K^+, (17) Mg^{2+}, (18) Ca^{2+}, (19) Zn^{2+}, and (20) N-acetylglucosamine were examined. The final volumes of the mixtures were adjusted to 300 μL in 96-well plate to afford the final concentration of 10 μM for the fluorophore and 1.0 mM for analytes. After the solution was mixed, fluorescence spectra were measured with an excitation wavelength of each fluorophore at room temperature.

2.5.1.2 Interference test

Fluorescence response of **A1**-**A3** with addition of a 5-fold excess concentration of those various ions/molecules were investigated under the same measurement conditions.

2.5.1.3 Fluorescence titration

The stock solution of fluorophore in DMSO (1 mM) was diluted with PBS buffer solution in a 1 mL quartz cuvette. Designated concentrations (0-1 mM) of the glucosamine was added into the sensor solution. The final volumes were adjusted to

1 mL by adding PBS buffer solution. The final concentration of each fluorophore is 10 µM in PBS aqueous buffer pH 7.4 solution. The emission spectra were recorded from 300 nm to 700 nm at ambient temperature using an excitation wavelength of each fluorophores

2.5.1.3.1 Detection limit

The limit of detection was estimated by plotting of fluorescence change of **A1** and **A2** in the range of glucosamine concentration 0.0- 50.0 µM. The detection limit is then calculated with the equation: detection limit = $3\delta/m$, where δ is the standard deviation of blank measurements; m is the slope between intensity versus sample concentration.

2.5.1.3.2 Benesi-Hilderbrand plot

The association constant was determined to obtain binding efficiency by the fluorescence spectral changes using Benesi-Hildebrand equation. The Benesi-Hildebrand equations for 1:1 complex formation are given by Equation:
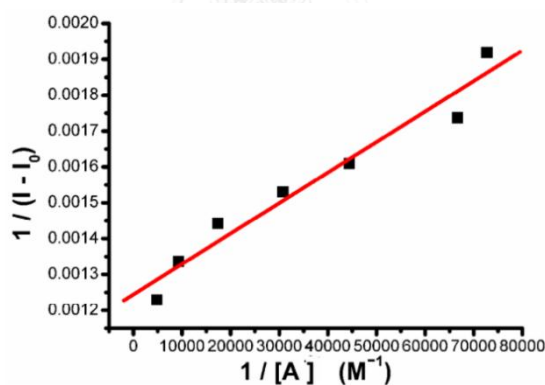
Figure 1.23 Benesi-Hilderbrand plot

$$Y = BX + A, \quad K_a = A/B$$

Where, Y is $1/(I-I_0)$, X is 1/[analyte], and K_a is the association constant.

2.5.1.4 pH effect study

The pH effect on fluorescence response of both free fluorophore and their Glucosamine complex was investigated by measuring of fluorescence emission spectra in the series of buffer between pH 3.0-10.0. The pH of the solution was fixed

by using acetate buffer (pH 3.0-6.0), phosphate (7.0-8.0) and tris-HCl (9.0-10.0). Final concentrations of probes, glucosamine and each buffer solution were 10 μM, 1.0 mM and 10 mM, respectively.

2.5.2 Zn^{2+} sensing

2.5.2.1 Selectivity Screening

Stock solution of each fluorophore (1mM) were prepared in CH_3CN. Stock solutions of metal ions (2mM) were prepared in Milli-Q water by dissolving of perchlorate, acetate, chloride or nitrate form of Li^+, Na^+, Ag^+, Ba^{2+}, Ca^{2+}, Cd^{2+}, Co^{2+}, Cr^{3+}, Cu^{2+}, Fe^{3+}, Hg^{2+}, Fe^{2+}, Ni^{2+}, Pb^{2+}, Ni^{2+}, Al^{3+} and Zn^{2+} ions.

In typical experiment, test solutions were prepared by placing 20 **μ**l of the probes stock solution in a 1 ml quartz cuvette, adding an aliquot of each metal stock. The final volumes were adjusted to 1 mL by adding HEPES-EtOH (1:9, v/v). The final concentrations of each fluorophore and metal ions were 20 μM and 200 μM, rescpectively.

2.5.2.2 Interference test

Under the same measurement conditions, competitive signaling behavior of **B1** toward Zn^{2+} in the presence of coexistence metal ions as background were studied. Final concentration of **B1**, Zn^{2+}, and the other various competing metal ions were 20 μM, 200 μM and 2.0 mM, respectively, in EtOH-HEPES buffer (9:1, v/v, pH 7.4).

2.5.2.3 Effect of solvent

The stock solutions are diluted into 20 **μ**M by varied solvents including, EtOH, THF, CH_3CN, and DMSO. The emission spectra of fluorophores with and without analyte were recorded at room temperature using an excitation wavelength.

2.5.2.4 Effect of water content

The stock solutions are diluted into 20 **μ**M by varied water content between 10% - 90% water in EtOH. The emission spectra of fluorophores with and without analyte were recorded at room temperature using an excitation wavelength.

2.5.3.5 pH effect

The pH effect on fluorescence signaling of fluorophores with and without analyte were investigated by measuring of fluorescence emission spectra in the series of buffer between pH 4.0-10.0. The pH of the solution was fixed by using acetate buffer (pH 4.0-6.0), phosphate (7.0-8.0) and tris-HCl (9.0-10.0). Final concentrations of fluorophore, analyte and each buffer solution were 20 μM, 200 μM and 10 mM, respectively.

2.6 Electrochemical measurements

Cyclic voltammetry (CV) experiments were carried out in a three-electrode system consisting of Ag/Ag$^+$ (0.01 M AgNO$_3$) as the reference electrode, glassy carbon as the working electrode and the platinum-wire as the counter electrode using a scan rate of 100 mV/s under nitrogen atmosphere to find HOMO levels of the fluorophores. The ferrocene was used as external standard for calibration CV curves. Fluorophores **A1**, **A2**, **A3**, **A,** and the external standard were dissolved in the supporting electrolyte (0.1 M of tetra-n-butylammonium hexafluorophosphate in anhydrous acetronitrile) to give final concentrations of 1 mM. The HOMO energy levels of the fluorophores were calculated from cyclic voltammetry using the equations:

$$E_{HOMO} = - [E_{ox} - E_{1/2} + 4.8] \text{ eV} \qquad (1)$$

Where E_{ox} is the onset oxidation potential, $E_{1/2}$ is the average of the anodic and cathodic peak potentials. The LUMO energy levels were calculated according to the equation:

$$E_{LUMO} = E_{HOMO} + E_{gap} \qquad (2)$$

The energy gaps (E_{gap}) were determined by using the onset of the longest wavelength absorption ($\lambda_{cut\ off}$) following equation:

$$E_{gap} = 1240/ \lambda_{cut\ off} \qquad (3)$$

2.7 Optimization of the fluorescence probe for cell imaging

Caco-2 cells were seed in 96-well plate at a density of 5x10^3 cells/200 µl of complete medium per well and incubated at 37 $^\circ$C in a humidified atmosphere enriched which 5% (v/v) CO$_2$. After seeding for 24 h, cultured cells were washed and

added with 200 µl of serum free medium. Subsequently, 2 µl of **A2** dissolved in DMSO was added to obtain the final concentrations of 0.01-4 µM and DMSO was used as a control. Treated cells were incubated for 24 h prior to an addition of 20 µl of a 5 mg/ml of 3-(4,5-dimethylthiazol-2-yl)-2, 5-diphenyltetrazolium bromide (MTT) solution. The incubation was continued for another 4 h. The media was removed and a mixture of DMSO (175 µl) and glycine (25 µl) was then added to each well to dissolve the formazan crystals. Absorbance of formazan at 540 nm was measured using a microplate reader (CLARIOstar® BMG LABTECH). Experiments were performed in quadruplicate. The suitable **A2** concentration for the study of qualitative internalization of glucosamine by Caco-2 cells was obtained at the cell viability of greater than 80% compared to the control.

2.8 Qualitative internalization of glucosamine by Caco-2 cells

Cultured cells were seed in 6-well plate at a density of 4×10^4 cells/2 ml of complete medium per well and incubated at 37 $^\circ$C in a humidified atmosphere enriched which 5% v/v CO_2. After seeding for 5 days (cell confluence), cultured cells were washed and added with 2 ml of serum free medium. Subsequently, 20 µl of the glucosamine solution dissolved in medium was added to each well to obtain the final glucosamine concentrations in the range of 0.1-1000 µM. Treated cells were incubated for 4 h. After incubation, cells were washed with 2 ml of serum free medium and subsequently added with 1 µM of **A2** prior to an additional incubation for 1 h. Cells were washed and added with 2 ml of PBS. Qualitative internalization of glucosamine into Caco2 cell was performed using fluorescence microscope (Nikon ECLIPSE Ti-U) at 10X of lens using excitation filter block 330-380nm and emission filter 435 nm.

2.8 X-ray crystallography

B1 (5.0 mg, 0.016 mmol) and $Zn(OAC)_2 \cdot 2H_2O$ (3.4 mg, 0.016 mmol) were dissolved in 2 ml MeOH. The mixture was stirred in air for 1 h, whereby a yellow precipitate was formed. It was filtered and then dissolved in hot MeOH. A single-crystal of F1-Zn^{2+} complex suitable for single crystal XRD was obtain on slow evaporation of the filtrate within 7 days.

CHAPTER III

RESULTS AND DISCUSSION

3.1 Glucosamine sensing (Part A)

3.1.1 Synthesis and characterization of fluorophores (**A1**-**A3**)

For our molecular design, 1,8-naphthalimide was used as a fluorophore and 8-amidooquinoline unit was installed as a binding cite for glucosamine. The synthesis began with the coupling between 8-aminoquinoline and *N*-Boc-alanine to afford an amide in a good yield of 91%. Treatment of with trifluoroacetic acid cleanly removed the *tert*-butoxycarbonyl group and provided the β-amino amide **A** in 92%. The spectroscopic data of **A** was in good agreement with the literature reports [106]. When **A** reacted with naphthalic anhydrides in refluxing ethanol, target compounds (**A1**-**A3**) were produced in good yields of 81-87 % after purification by flash chromatography on silica gel (Scheme 3.1). All these new compounds were characterized using standard NMR spectroscopy, mass spectrometry, and elemental analysis.
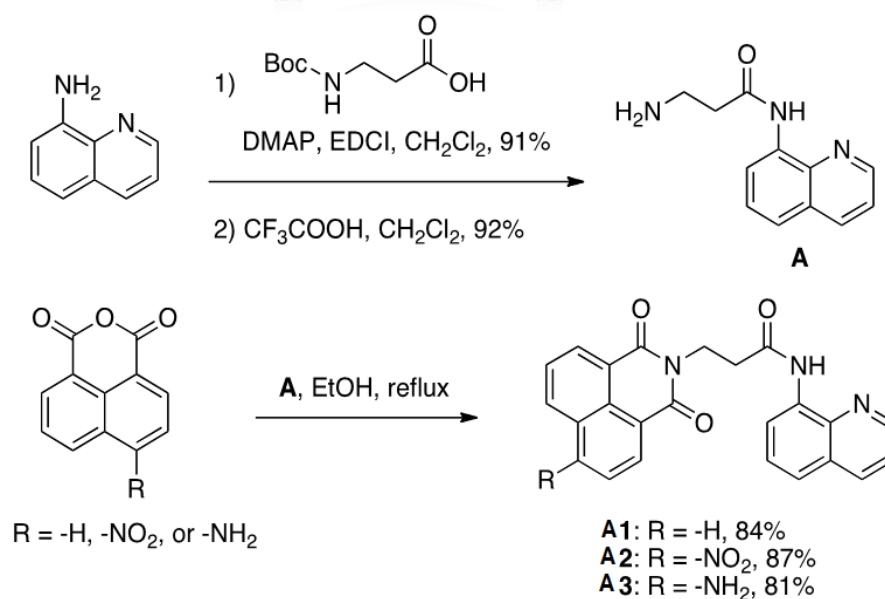
Scheme 3.1 Synthesis of **A1**-**A3**

The ¹H NMR spectra of compound **A** in CDCl₃ is shown in Figure 3.1 All signals can be assigned as labelled in the structure. The characteristic signals include the amide proton (-CONH) which appears as a broad singlet at 10.3 ppm and the two adjacent methylene protons (a, b) appearing as two triplets at 3.5 and 2.8 ppm, respectively. The spectrum indicated a successful preparation of the β-amino amide **A**.
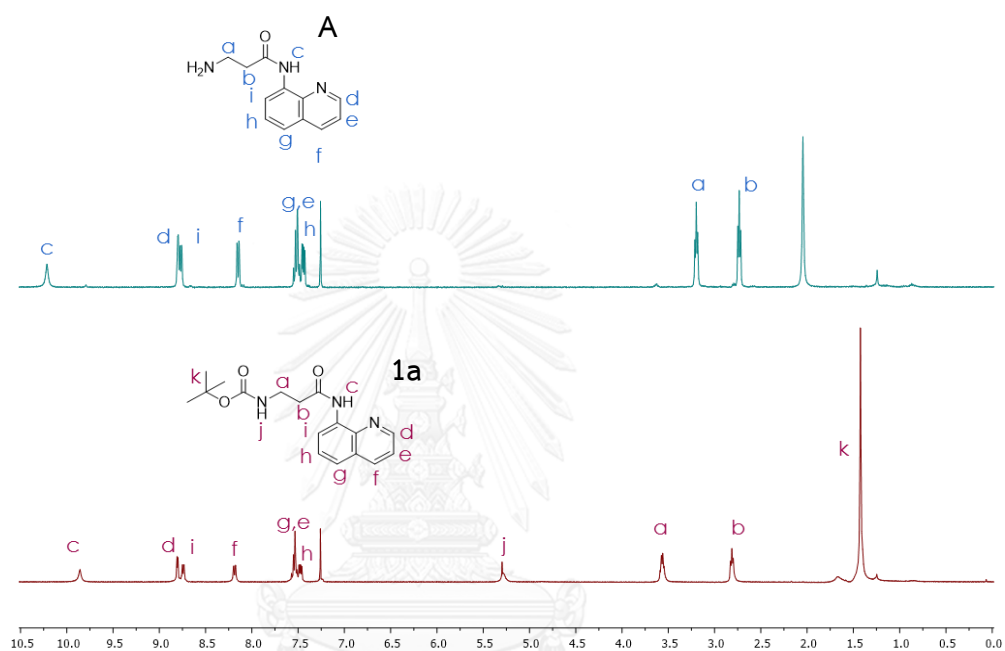
Figure 3.1 ¹H NMR spectra of **A** and **1a** in CDCl₃

The condensation reaction of **A** with naphthalic anhydrides gave target compound **A1**, **A2**, and **A3**. Their structures were confirmed by NMR spectroscopy as shown in Figure 3.2. The appearance of napthalimide (j-o) and aminoquinoline protons (a-g) in the spectrum suggested successful coupling reactions. For all compounds, the two methylene protons (i, h) have moved down-field to around 4.5 and 3.0 ppm, respectively, as a result of electron-withdrawing imide groups. However, the signal for aromatic proton k in **A1**, **A2**, and **A3** appears at different positions (7.7, 8.4, and 6.8 ppm, respectively) due to the different substituent at the 4-position of napthalimide moieties (-H, -NO₂, and -NH_{2,} respectively).

The molecular masses of **A1**-**A3** were determined by MALDI-TOF-MS and the results are shown in Figure 3.3. Elemental analysis also agreed with the calculated data, and they are included in the experimental section (see Chapter II).
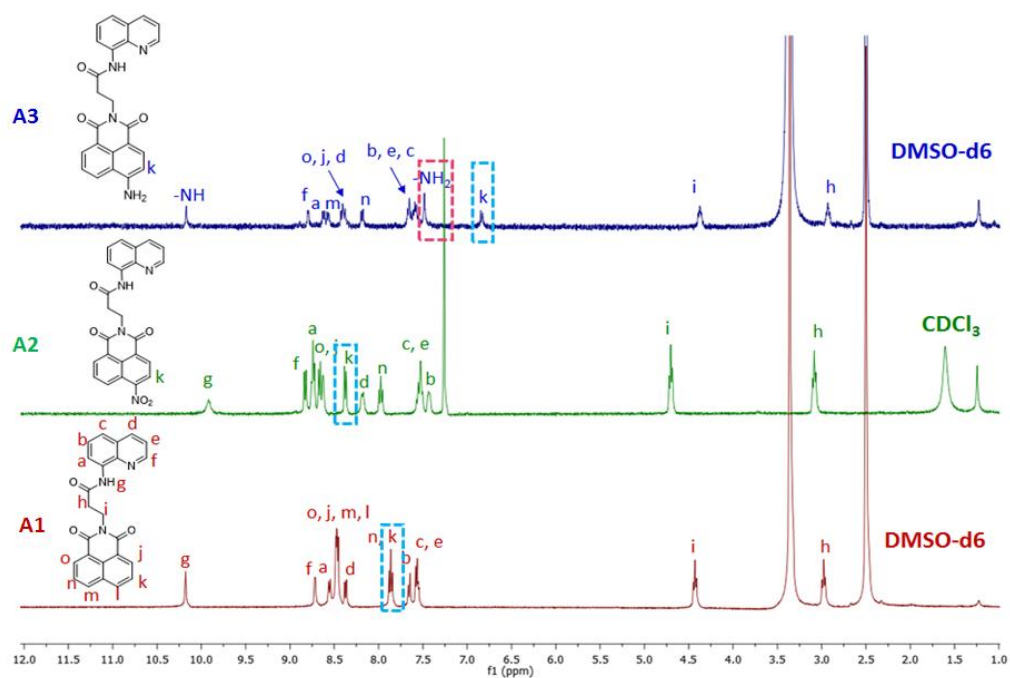
Figure 3.2 ^{1}H NMR spectra of **A1-A3**
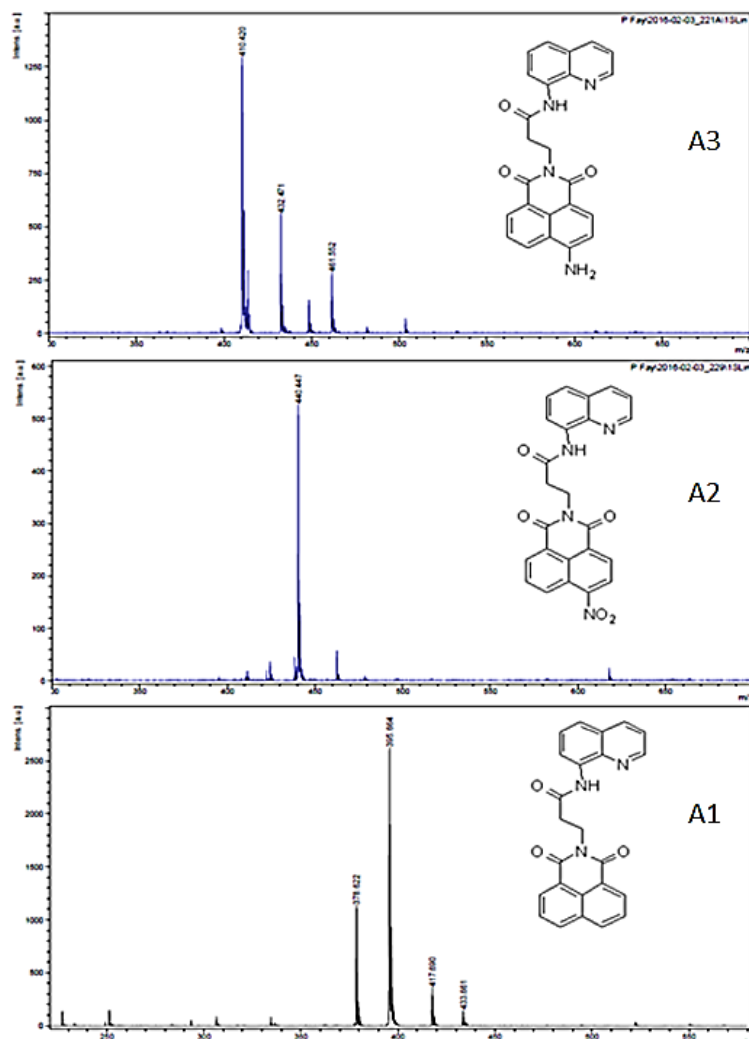
Figure 3.3 MALDI-TOF-MS spectra of **A1-A3**

3.1.2 Photophysical properties studies

The photophysical properties of **A1-A3** were investigated in PBS buffer pH 7.4. The photophysical properties are summarized in Table 3.1, while the UV-Vis and fluorescence spectra are shown Figure 3.4.
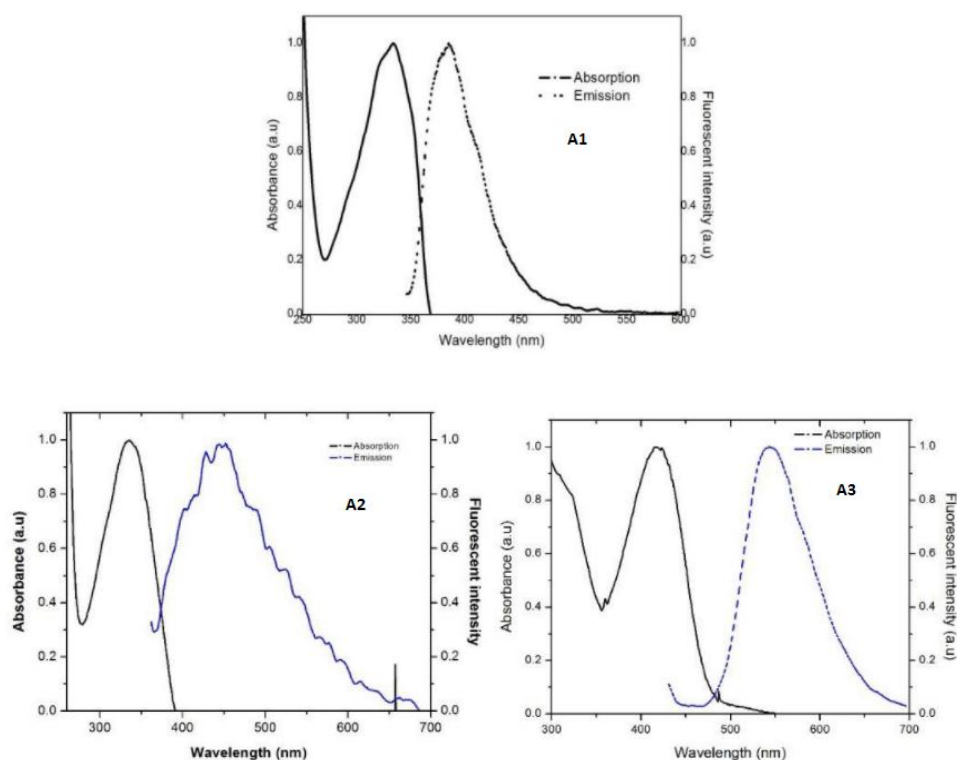
Figure 3.4 Normalized absorption and emission spectra of **A1**-**A3** in PBS buffer pH 7.4.

Based on the larger molar extinction coefficients of an isolated 1,8-naphthalimide (~16,000 M^{-1}) compared to that of the isolated 8-aminoquinoline (~4,000 M^{-1}) and the fact that their emission maxima closely resembled those of naphthalimides, it is likely that the naphthalimide moieties are likely to be the fluorescence signal transducers in these naphthalimide-aminoquinoline dyads (**A1**-**A3** Therefore, the amidoquinoline should only function as a receptor for the prospective analysts. Each fluorophore showed a broad absorption band with λ_{max} around 330-420 nm with molar extinction coefficients of 8.3 x 10^3 – 9.8 x 10^3 M^{-1} cm^{-1}. The maximum emission wavelengths of **A1**-**A3** appeared at 385, 435, and 542 nm, respectively. The longest emission maxima in **A3** may result from the internal charge transfer from the electron-donating NH_2 group to the electron-withdrawing naphthalimide C=O. The presence of a strong electron-withdrawing NO_2 group in **A2** could perhaps narrow the HOMO-LUMO gap of the naphthalimide, but the quenching properties of such group may result in a unquantifiable quantum efficiency as

resulted from the pre-decomposition of the NO_2 group or the formation of radiationless transition state [107].

Table 3.1 Photophysical properties of **A1**-**A3**

	Absorption		Emission			M_p (^{o}C)
	λ_{max} (nm)	ε ($M^{-1}cm^{-1}$)	λ_{max} (nm)	Φ_F	Φ_{FC}	
A1	334	9600	385	0.0027[a]	0.042	214-215
A2	348	8300	435	<0.0027[a]	0.038	232-234
A3	418	9800	542	0.066[b]	-	321-323

[a]2- Aminopyridine in 0.1 M H_2SO_4 (Φ_F = 0.60) was used as the reference.

[b]Quinine sulfate in 0.1 M H_2SO_4 (Φ_F = 0.54) was used as the reference.

3.1.3 Selectivity screening of compound **A1**-**A3** toward analytes

The selectivities of **A1**-**A3** (10 µM) towards analytes (1 mM) like glucosamine and various biochemical components such as proteins, amino acids, monosaccharide (glucose), disaccharide (sucrose), physiological ions (Na^+, Ca^{2+}, K^+), naturally-occurring compound (caffeine), amines, as well as *N*-acetylglucosamine were examined in phosphate buffer at pH 7.4. In Figure 3.5, it was found that both **A1** and A**2** exhibited a selective fluorescence enhancement in the presence of glucosamine as their quantum yields were over 14-fold increased. In addition, we observed that glucosamine could cause nearly 4-fold fluorescence enhancement on amidoquinoline **A** as well (Figure 3.6). This information suggested that the amidoquinoline moiety in **A1** and **A2** can interact with glucosamine with high selectivity, while the naphthalimide can enhance the sensitivity of these sensors.
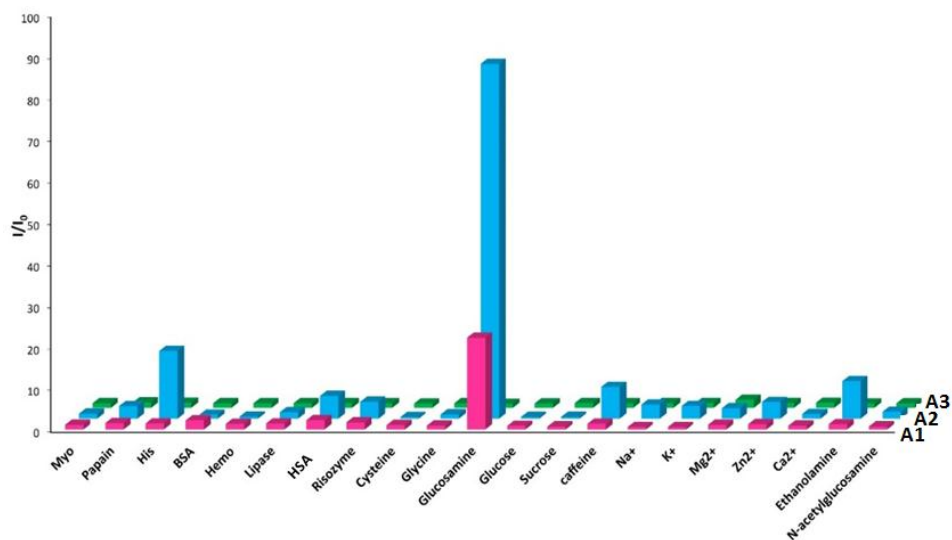
Figure 3.5 Fluorescence response of **A1**-**A3** (10 µM) towards various analytes (1.0 mM).
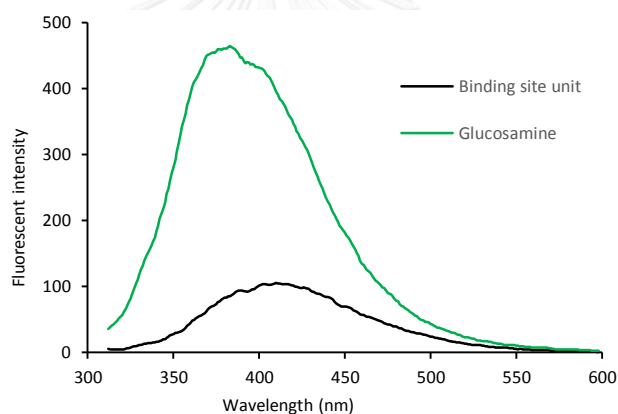
Figure 3.6 Fluorescence response of amidoquinoline **A** with addition of glucosamine

3.1.4 Glucosamine binding properties

The fluorescence responses of free fluorophores (**A1** and **A2**) and their glucosamine complexes were analyzed under various pH's to evaluate their applicable pH range as shown in Figure 3.7. In the absence of glucosamine, there was no significant difference in fluorescence response of sensor **A1** and **A2** under pH between 3 to 10. We then assume that the initial fluorescence intensities (I_0) for **A1** and **A2** are pH-independent. Upon addition of glucosamine, the enhanced fluorescence intensities were observed particularly at pH higher than 8.0. It could be

rationale that at pH 8.0 and above the d-glucosamine hydrochloride predominantly exists in free amine form (pKa 7.58) and could bind strongly with the sensors.
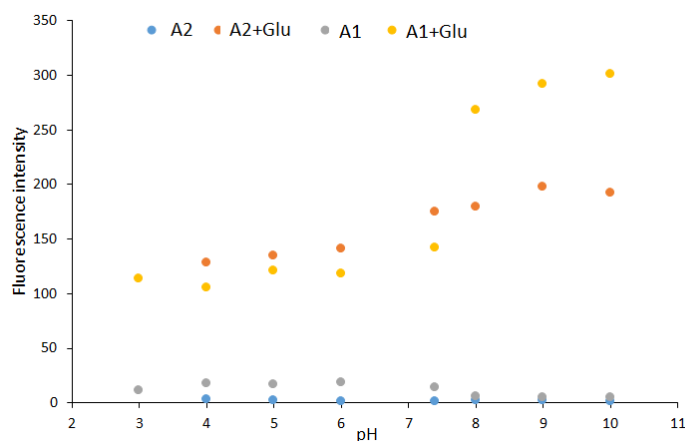
Figure 3.7 Effect of pH on the emission intensity of **A1**-**A2** and their glucosamine complexes.

The detection limits were calculated with the Eq. (DL=3σ/m). In the Equation, σ is the standard deviation of blank measurement, which can be acquired by ten times measurements of emission spectrum of each sensor, m is the slope from plotting the fluorescence intensity versus various glucosamine concentrations. As shown in Figure 3.8, it shows a good linear relationship in the range of 0 to 40 μM for **A1** (R^2=0.9668) and in the range of 0 to 50 μM for **A2** (R^2=0.9988). From above data, the detection limits at three-time noise were of 1.06 µM and 0.29 µM, respectively.

From the Benesi-Hildebrand plots (Figure 3.9) the association constants (K_a) were determined from the fluorescence titration curves of **A1** and **A2** to be 1.55×10^4 M^{-1} and 1.45×10^4 M^{-1}, respectively.
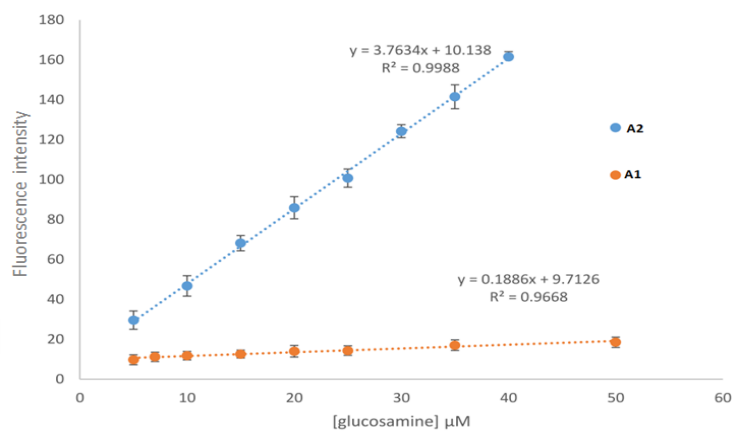
Figure 3.8 Linear plot of **A1** and **A2**
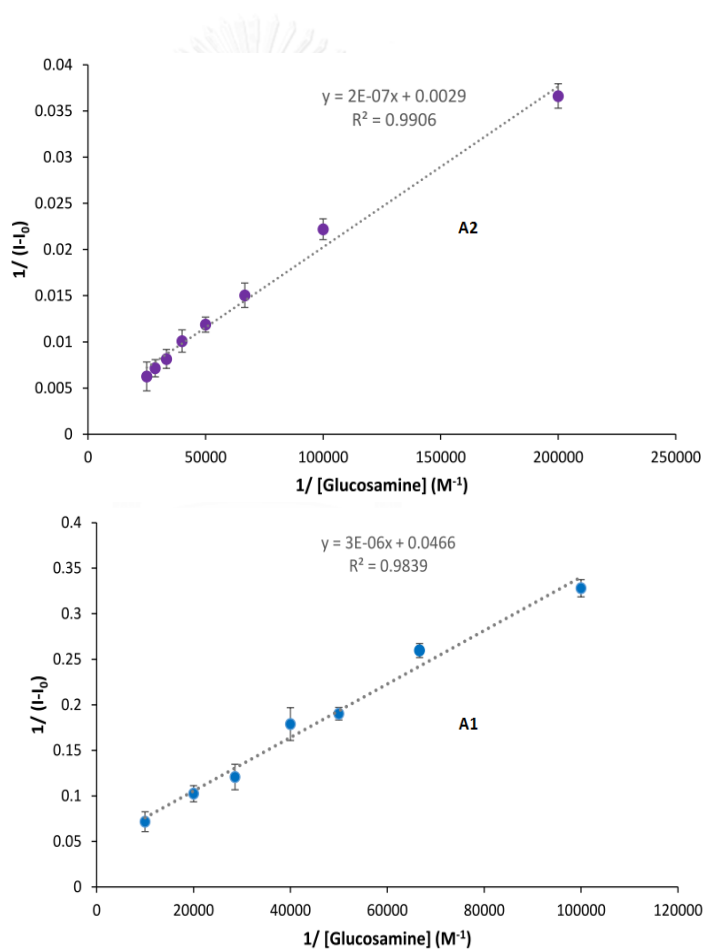
Figure 3.9 Benesi-Hildebrand plots of **A1** and **A2**

The impressive selectivity of **A1** and **A2** towards glucosamine may be attributed to multiple hydrogen bonding between amidoquinoline and gluocosamine as previously suggested by Cheng et al. in 2012 [41]. In fact, the analysis of a mixture between **A1** and glucosamine by mass-spectrometry revealed the m/z of 685.53 belonging to the mass of $[(C_6H_{13}NO_5 \cdot HCl \cdot A1) + MeOH + H_2O + Na]^+$ (Figure 3.10).
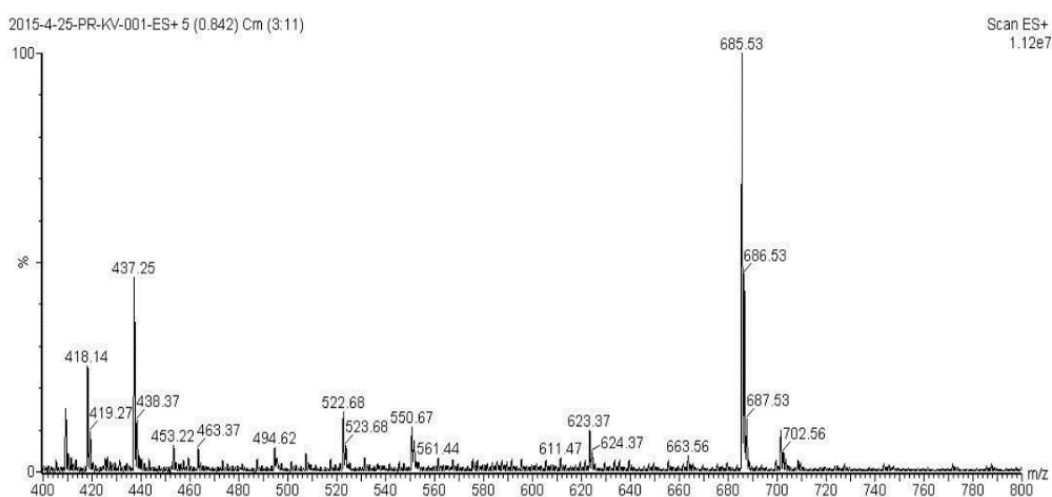
Figure 3.10 ESI-MS spectrum of **A1**-glucosamine complex

From this observation, the fluorescence enhancement may involve the inhibition of photo-induced electron transfer (PET) between the excited naphthalimides and the amidoquinoline moiety. The fact that only **A1** and **A2** show fluorescence enhancement suggested that the half-filled HOMO orbital of the excited states of these unactivated or electron-poor naphthalimide moieties function as the electron acceptors in the PET process. The electron-donating group such as –NH_2 in **A3** probably elevates the HOMO energy levels of naphthalimide, leading to ineffective PET process as evidenced by its higher fluorescence quantum efficiency. Without the initially installed PET process, its binding with glucosamine did not enhance the fluorescence signal. In order to verify the statements described above, the HOMO energy levels for **A1**–**A3** and the amidoquinoline **A** were determined from their onset oxidation potentials observed in linear sweep voltammograms (Figure 3.11). Based on the HOMO-LUMO energy gaps calculated from the onset absorption bands, the HOMO and LUMO levels of all compounds are depicted in Figure 3.12 and summarized in Table 3.2. The LUMO levels of **A1**–**A3** lie below the LUMO of the

amidoquinoline **A** implies that the naphthalimide fragments behave as the electron acceptor in the PET process. As expected, the HOMO level of **A3** is higher than that of **A1** and **A2** due to the electron donating –NH$_2$ group. Most importantly, the HOMO level of **A** (-5.10 eV) lies above those of **A1** (-5.40 eV) and **A2** (-5.45 eV), but below that of **A3** (-5.07 eV), suggested that the PET process is perceptible in **A1** and **A2**. This lack of PET process in **A3** was also evidenced by a much higher fluorescence quantum efficiency of this compound comparing with **A1** and **A2**.
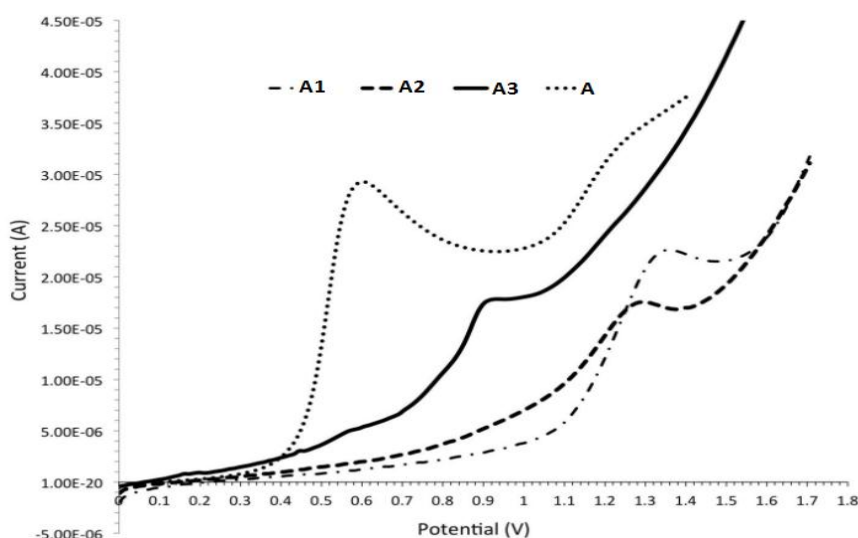
Figure 3.11 Linear sweep voltammogram of amidoquinoline **A** and compounds **A1**-**A3** (1 mM, scan rate = 100 mV/sec).

Table 3.2 Electrochemical properties of amidoquinoline **A** and compounds **A1**-**A3**

	E^a_{ox} (V)	E^b_g (eV)	HOMO^c (eV)	LUMO^d (eV)
A	0.39	3.14	-5.10	-1.96
A1	0.69	3.37	-5.40	-2.03
A2	0.74	3.13	-5.45	-2.32
A3	0.36	2.53	-5.07	-2.54

^{a}Onset oxidation potential obtained from linear sweep voltammogram;

^{b}HOMO-LUMO energy gap estimated from the onset absorption wavelength using a formula: $E_g = 1242/\lambda_{onset}$;

^{c}HOMO energy level calculated from E_{ox} using a formula: HOMO = $-(E_{ox} + E_{FC/FC+})$ where $E_{FC/FC+}$ is the corrected oxidation potential of ferrocene (4.71 eV);

^{d}LUMO energy level calculated using a formula: LUMO = HOMO + E_g.

Figure 3.12 HOMO-LUMO energy levels of amidoquinoline **A** and **A1**–**A3**

3.1.5 Application of **A2** as fluorescent probe in living cell

Due to its poor oral bioavailability, a very high dose of glucosamine of 1.5–3.0 g/day is recommended as a dietary supplement for people with osteoarthritis [108]. Various oral formulations for improvement of bioavailability of glucosamine have continuously been developed and tested for the cellular uptake and permeability [109]. The human epithelial colorectal adenocarcinoma (Caco-2) cell line originated from human colonic carcinoma exhibits some morphological and functional characteristics similar to those of differentiated epithelial cells that line the intestinal mucosa [110]. Therefore, the Caco-2 cell line has often been used for studies of cellular uptake and permeability of drugs [111, 112]. HPLC has been used as the standard method for quantitation of glucosamine in Caco-2 cells, but this method involves cell lysis and derivatization process [51, 113]. Recently, the development of fluorescent dyes for detecting or probing chemicals inside living cells has received considerable attention [114-117], but the spectrofluorometric methods for determination of glucosamine in living cells has never been investigated. We therefore demonstrate that **A2** can serve as a fluorescent imaging probe for detection of cellular glucosamine, which could further be applied for the real-time quantitative determination of cellular uptake and permeation studies as an alternative to HPLC.

Since **A2** may be harmful to the Caco-2 cells, it is important to optimize its concentration to avoid cellular cytotoxicity. To determine the effect of **A2** on the cell viability, MTT cytotoxicity assay was performed against Caco-2 cells exposed with different concentrations (0.01–4 µM) of **A2** for 24 h. The concentration of **A2** between 0.01 and 1 µM provided the cell viability of greater than 80% (Figure 3.13), therefore, 1 µM of **A2** was selected for the cell imaging. Fluorescence images in Figure 3.14 indicated that **A2** could be used as an intracellular glucosamine probe for Caco-2 cells that was internalized by glucosamine at the concentration of greater than 1 µM. We postulate that the detection limit for glucosamine inside the Caco-2 cells is possibly less than 1 µM since the cellular uptake of glucosamine might not be completed. Nevertheless, this work clearly demonstrates the potential use of **A2** as a real-time probe for cellular glucosamine in living cells.
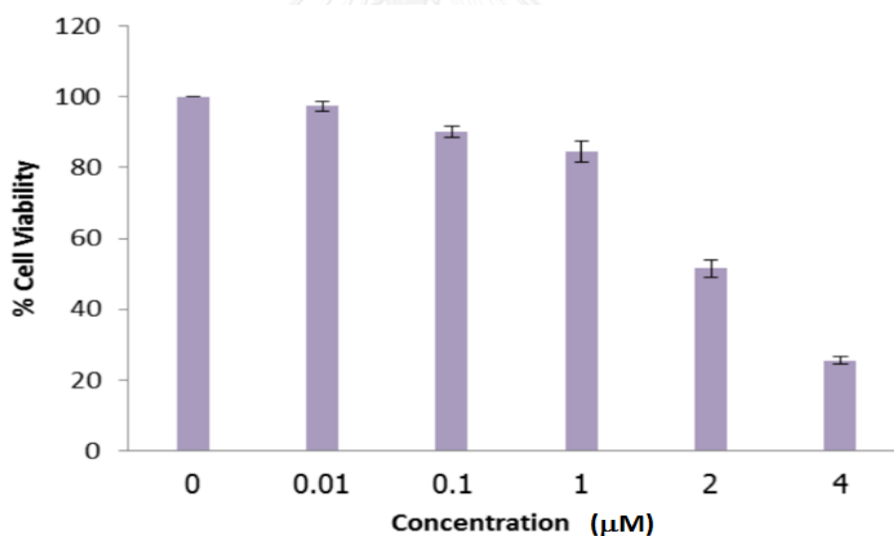
Figure 3.13 Cytotoxic effect of different concentrations of **A2** on the viability of Caco-2 cell
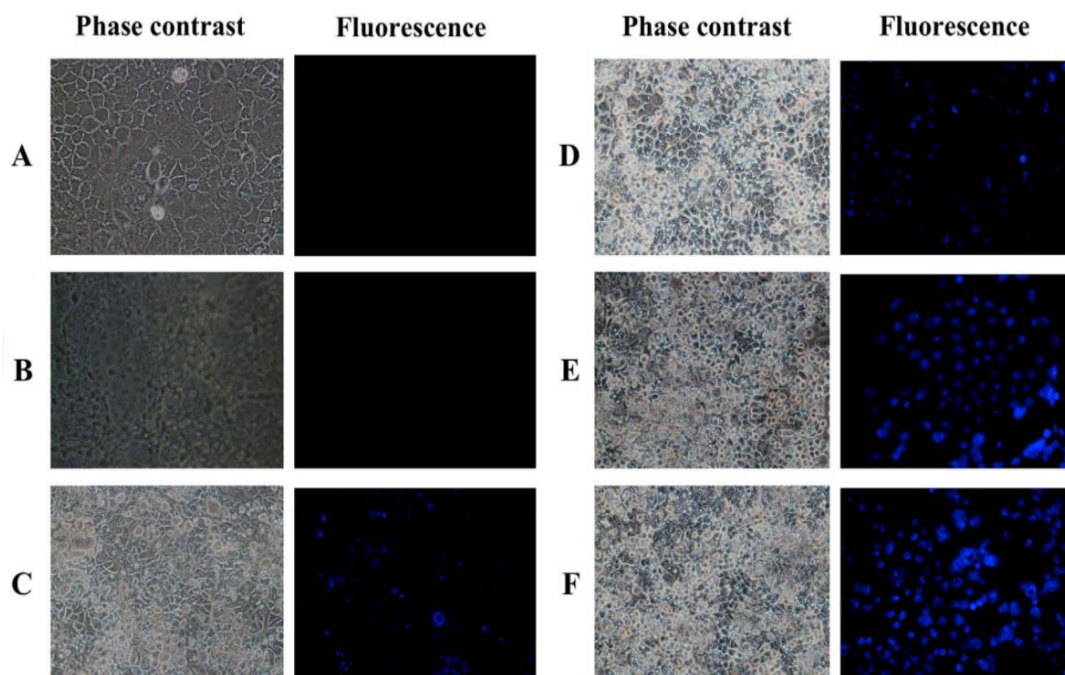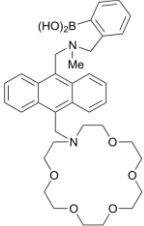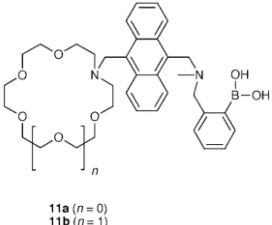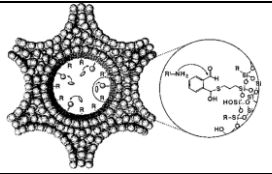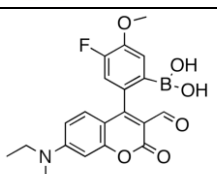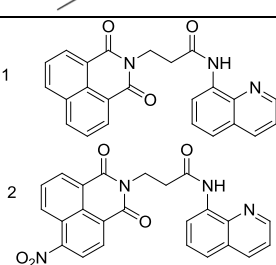
Figure 3.14 A–F Microscope images of Caco-2 cells internalized by glucosamine at 0, 0.1, 1, 10, 100 and 1000 µM respectively. The fluorescence images were visualized by 1 µM of **A2**.

3.1.6 Benchmarking of the glucosamine fluorescent sensors.

In comparison with previously reported glucosamine fluorescent sensors, both **A1** and **A2** display superior sensitivities in terms of detection limit and association constant (Table 3.3). Another advantage of these sensors is that they can be used in aqueous media without interference from other biological components including the structurally related *N*-acetylglucosamine, which leads us to achieve the fluorescence detection of glucosamine in living cells at micromolar level.

Table 3.3 Benchmarking of the glucosamine fluorescent sensors

	Solvent	Detection limit	Association constant, K_a	Ref.
	1:2 Ethanol: buffer pH 7.18	n.a.	0.5 mol dm^{-3}	Cooper and James, 1997
	1:2 Ethanol: H$_2$O	n.a.	18 mol dm^{-3} 17 mol dm^{-3}	Cooper and James, 2000
	Aqueous buffer	n.a.	n.a.	Lin et al., 2001
	1:1 Ethanol: H$_2$O	5.6 μM	n.a.	Cheng et al., 2012
	HEPES buffer pH 7.4	n.a.	4100	Tran et al., 2015
	PBS buffer pH 7.4	1.06 μM 0.29 μM	1.55×10^4 M^{-1} 1.45×10^4 M^{-1}	This work

3.2 Metal ion sensing (Part B)

3.2.1 Synthesis and characterization of **B1**-**B4**

The preparation of 8-aminoquinoline-containing fluorescent sensors for zinc (II) ion (**B1**-**B4**) was outlined in Scheme 3.2 . Compound **A** was prepared according to literature procedure as mention previously [106]. Condensation of **A** and

salicylaldehyde afforded **B1** (87%), followed by reductive amination with NaBH$_4$ to give compound **B2** in good yield (82%). As for **B3** and **B4**, the synthesis started with iodination of 8-aminoquinoline, then installation of a β-amino amide by using *N*-Boc-alanine provided the corresponding amide **2A** in 77% yield. Subsequently, the Sonogashira coupling of **2A** with 4-ethynyl-*N*,*N*-dimethylaniline and further treatment with trifluoroacetic acid cleanly removed the *tert*-butoxycarbonyl group to afford the key intermediate **3A** in a good yield of 72%. Finally, the condensation of **3A** with salicylaldehyde generated compound **B3** (87%), and then be reduced with NaBH$_4$ to obtain **B4** in good yield of 89%. The molecular structure of **B1**-**B4** were characterized by ^{1}H NMR, ^{13}C NMR, and mass spectroscopy, which were in full agreement with the expected structures.
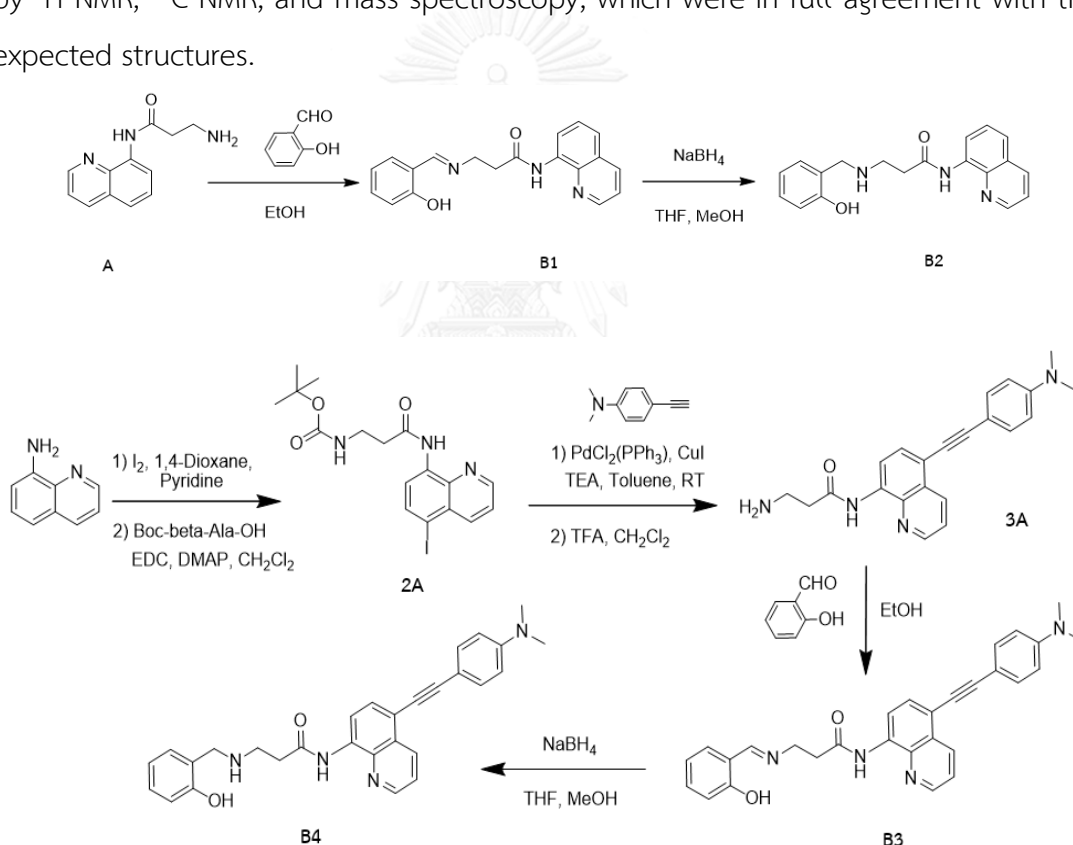
Scheme 3.2 Synthesis of **B1**-**B4**

For the NMR characterization, 1H NMR spectra of fluorophores B1-B4 is shown in Figure 3.15. B1 showed imine proton signal (HC=N) around 8.6 ppm, amide proton (NH) around 12.0 ppm and the characteristic aminoquinoline peaks (f, g, h, i, j, and k) around 8.8, 7.4, 7.5, 8.2, 7.6 and 8.7 ppm, respectively. **B2** showed methyl protons (b) at 4.0 ppm, which mean imine proton of **B1** was completely reduced. As for

extension of π-conjugate system of **B3** and **B4**, aromatic protons (n, o) and methyl protons (p) of 4-ethynyl-N, N-dimethylaniline were observed around 7.5, 6.7, and 3.0 ppm, respectively.
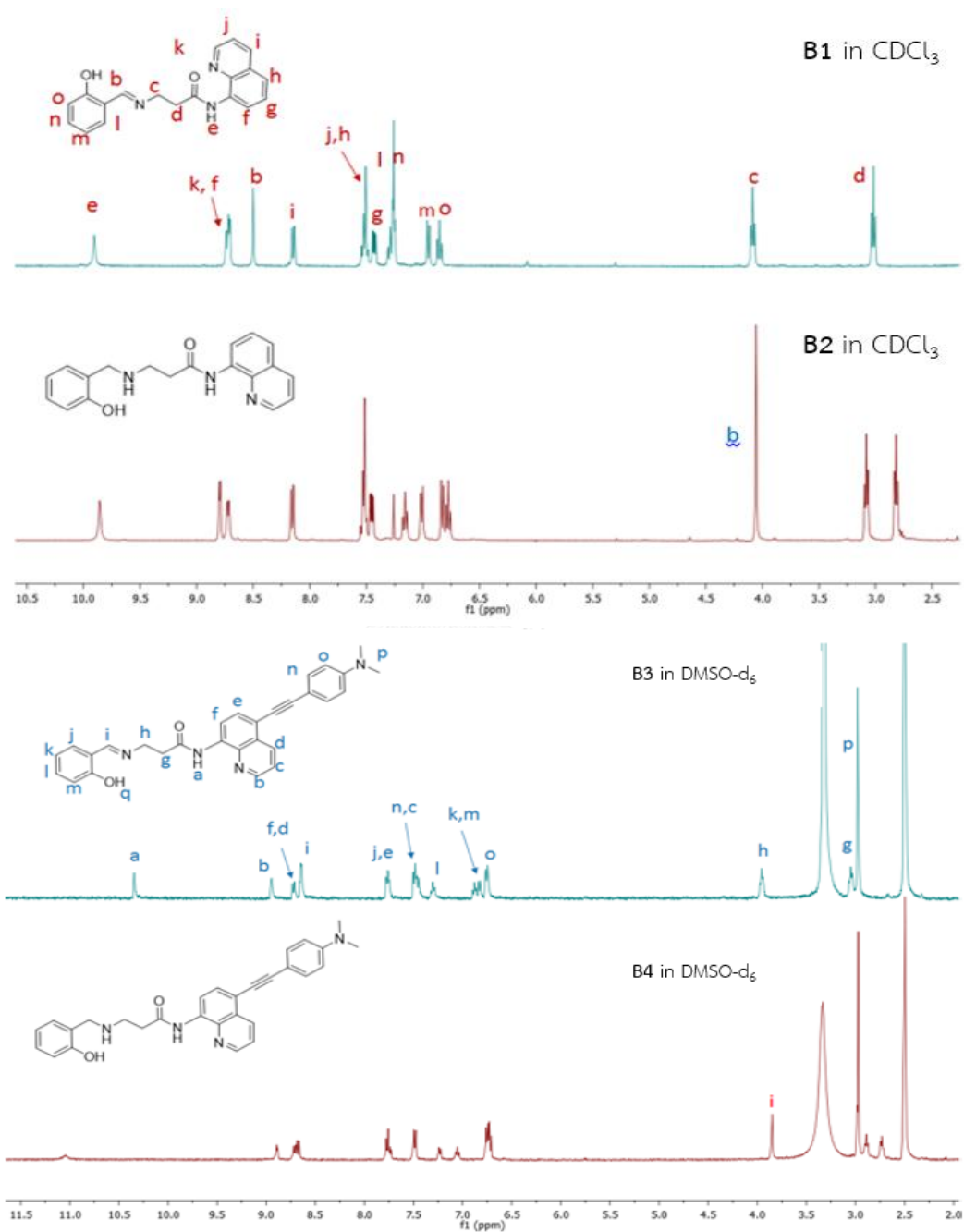
Figure 3.15 ^{1}H NMR spectra of compound **B1**-**B4**

3.2.2 Photophysical properties of **B1**-**B4**

The absorption and emission spectra of compounds **B1**-**B4** in EtOH- H_2O (9:1, v/v) (20µM) were presented in Figure 3.16 and their photophysical data are summarized in Table 3.4. The obtained results indicated that the absorption properties of **B1** and **B2** closely resembled those of 8-aminoquinoline with the maximum absorption wavelengths appeared around 320 nm and maximum emission wavelengths around 390 nm. Compared to **B1**- **B2**, **B3** and **B4** presented pronounced red-shifted in both absorption and emission due to the extension of π-conjugation and their spectra showed the similar spectral shapes with absorption and emission bands about at 389 nm and 550 nm, respectively. The extension of the π-system by the ethynyl aryl group (in **B3** and **B3**) could increase both the molar extinction coefficients and the fluorescent quantum yields.
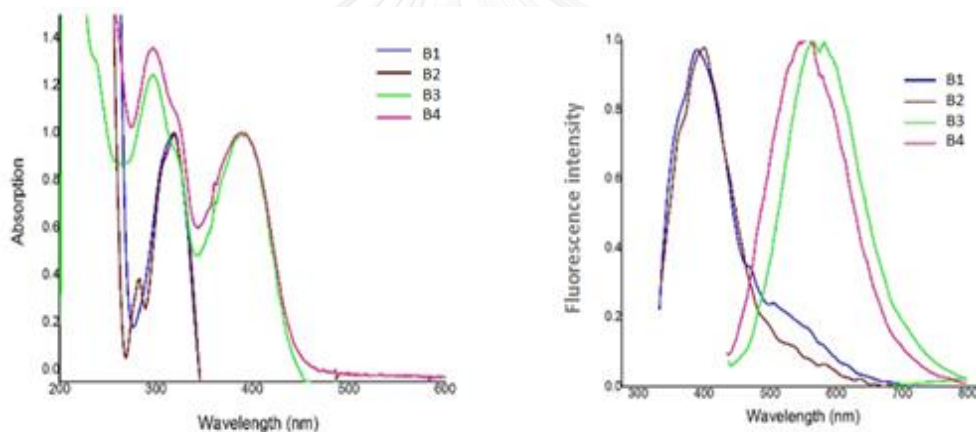
Figure 3.16 (a) UV-Vis (b) and fluorescence emission spectra of **B1**-**B4** (20 µM)

Table 3.4 Photophysical properties of sensor B1-B4 in EtOH-H2O (9:1, v/v).

Cpd.	Absorption		Emission		Mp (^{o}C)
	λ_{max} (nm)	ε ($M^{-1}cm^{-1}$)	λ_{max} (nm)	Φ_F, Φ_{FC}	
B1	318	5200	391	0.0022, 0.429	114-115
B2	320	5100	398	0.0031, 0.324	106-107
B3	389	12400	554	0.026, 0.202	238-239
B4	389	12100	562	0.033, 0.109	178-179

Quinine sulfate in 0.1 M H_2SO_4 (Φ_F = 0.54) was used as the reference.

3.2.3 Fluorescence studies of **B1**-**B4** toward Zn^{2+} ion and other metal ions.

Next, the selectivities of fluorophores (**B1**-**B4**) towards various metal ions such as Zn^{2+}, Mn^{2+}, Ba^{2+}, Hg^{2+}, Ni^{2+}, Cu^{2+}, Co^{2+}, Pb^{2+}, Mg^{2+}, Cd^{2+}, Fe^{2+}, Cr^{3+}, Al^{3+}, Fe^{3+}, Li^{+}, K^{+} and Na^{+} were determined. Upon addition of the metal ions to the solution of **B1**-**B4**, it was found that only Zn^{2+} could induce remarkable red-shifts of emission spectra as shown in Figure 3.17-3.18. The addition of Zn^{2+} ion to **B1**, a slight decrease in fluorescent intensity and a 140 nm red-shift from 391 to 535 nm of fluorescence emission were observed. The red-shift of emission spectra of **B1** was attributed to the deprotonation of the amide (-NH) upon binding with Zn^{2+}. Meanwhile, significant fluorescence quenching was detected with the addition of $Cu^{2+}$, Co^{2+}, Fe^{2+}, and Ni^{2+} due to their well-known paramagnetic effect [118, 119]. The other ions produced minor changes in the fluorescence intensity ratio value. The results showed that the addition of Cd^{2+} did not induce the increase of fluorescence intensity at 535 nm, even though it is in the same group with Zn^{2+} on the periodic table. Indeed, our quinoline-based sensors provided better selectivity towards Zn^{2+} over Cd^{2+} than those derivatives reported previously [24, 27, 31, 120-122].

Under the identical conditions, however, Al^{3+} also induced a significant fluorescence enhancement for compound **B1**. It was found that the salicylaldimine double bond (C=N) was possibly hydrolyzed by Al^{3+} which behaves as a hard Lewis acid, to give aldehyde and amine compound. As shown in Figure 3.19, the cleavage of imine in a presence of Al^{3+} is not taking place with **B1** only, but it also happens in case of compound **B3**, albeit rather slowly (2 hours). According to the proposed model, fluorescence studies of hydrolyzed compounds toward Al^{3+} were carried out. Upon addition of Al^{3+} to a salicylaldehyde solution, an obvious fluorescence signal on around 440 nm was observed, whereas there is no effect to the amine solution as shown in Figure 3.20. The result suggested that salicylaldimine could undergo hydrolysis under the acidic condition, which confirmed by ^{1}H NMR titration spectra as shown in Figure 3.21. Upon gradual addition of Al^{3+} to the D_2O/Acetone-d_6 solution of **B1**, the imine proton at 8.63 ppm was slightly decreased along with the appearance of aldehyde proton of salicylaldehyde moiety at 10.0 ppm. Remarkably,

this selectivity by **B1** and **B3** to turn on fluorescence in the presence of Al^{3+} is not seen for **B2** and **B4**. In this work, we so conducted all further experiments after mixing of the fluorophore with metal ions immediately.
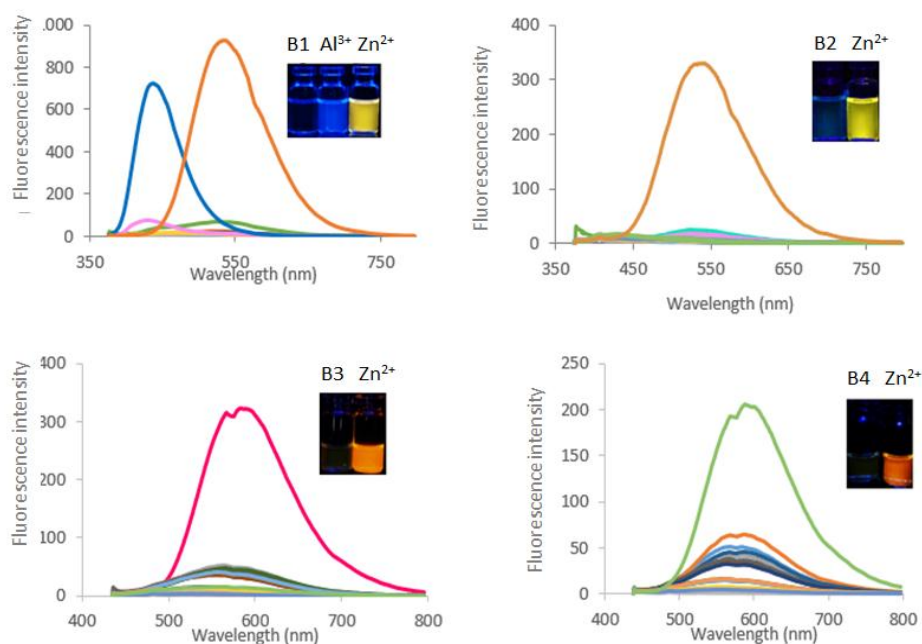
Figure 3.17 Fluorescence spectra of **B1**-**B4** (20 µM in EtOH-H_2O (9:1, v/v)) before and after addition 10 equiv. of metal ions.
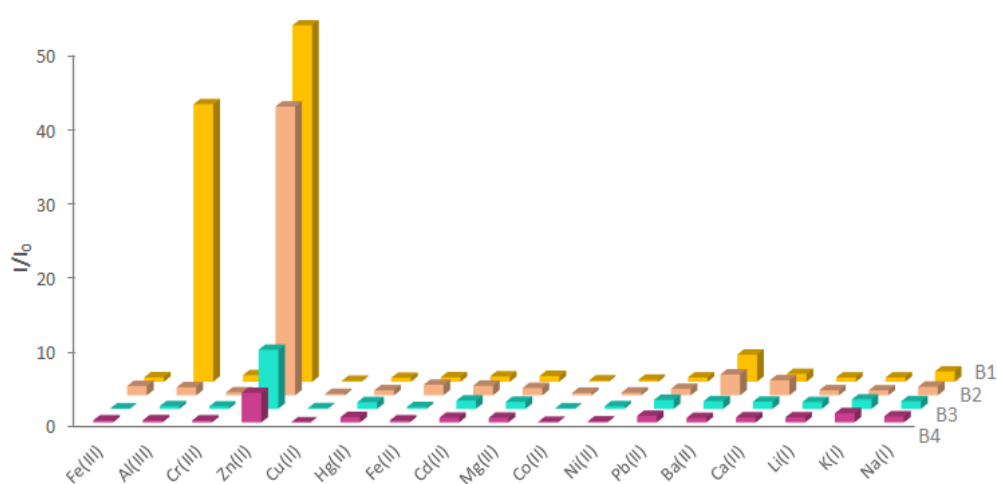
Figure 3.18 Fluorescence enchantment ratios of **B1**-**B4** (20 µM) in EtOH-H_2O (9:1, v/v) upon addition of various metal ions (200 µM), (λ_{ex}= 360 nm and 420 nm for **B1**-**B2** and **B3**-**B4**, respectively).
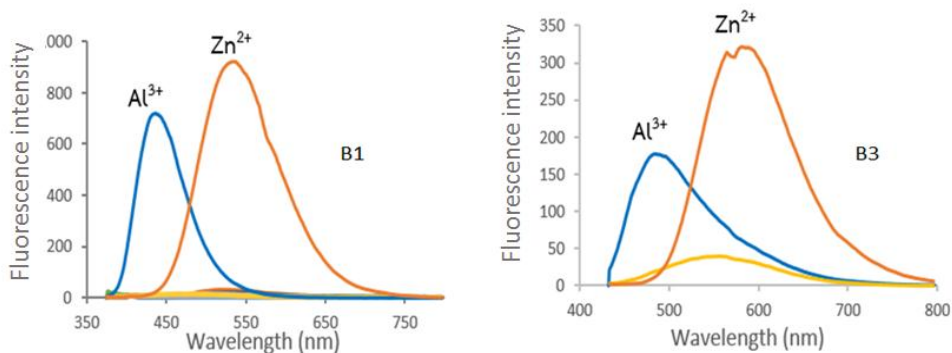
Figure 3.19 The fluorescence spectra upon addition of 10 equiv. Al^{3+} and Zn^{2+} were obtained after mixing for **B1** and after mixing 2 h for **B3**
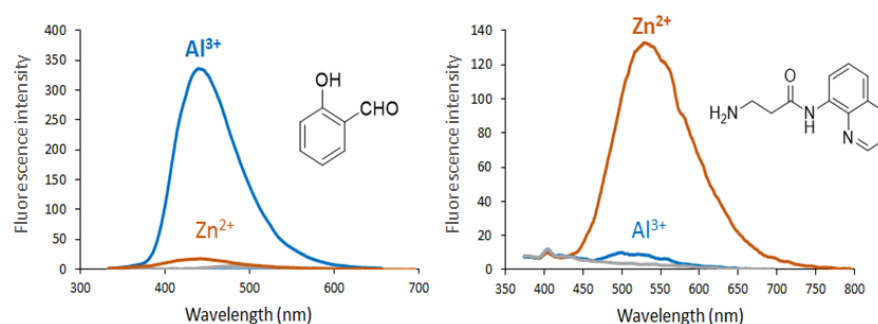
Figure 3.20 Fluorescence spectra of aldehyde and amine compound upon addition of Al^{3+} and Zn^{2+}
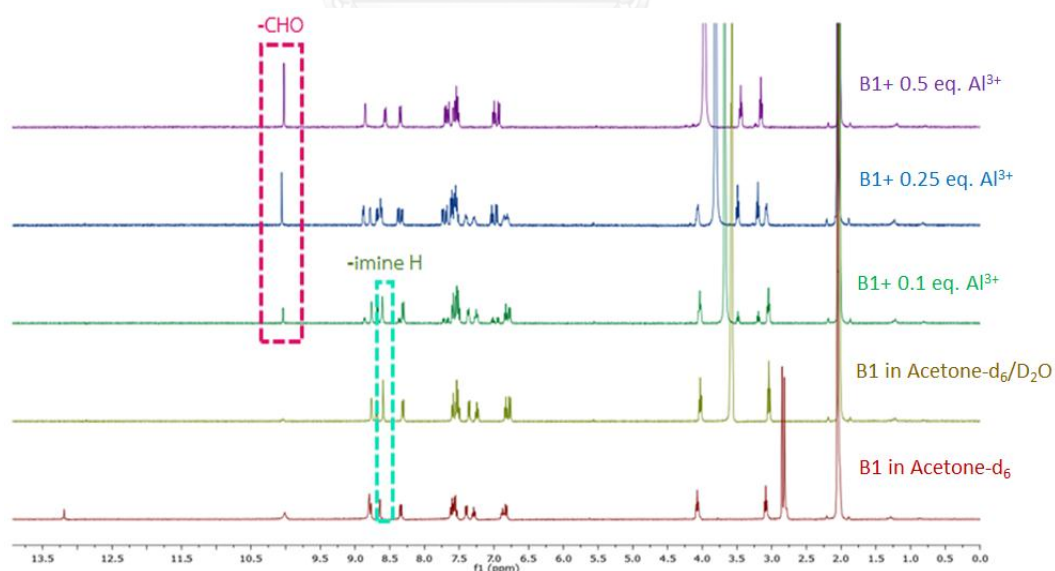
Figure 3.21 ^{1}H NMR titration spectra of **B1** upon addition Al^{3+} (0-0.5 equiv.) in mixing solvent (D$_2$O/Acetone-d$_6$).

3.2.4 Metal binding properties

The fluorescence response of fluorophores for Zn^{2+} in various solvents was first investigate. For example, turn-on fluorescence signal of **B1** is sensitive in some aqueous solvent systems, such as THF, EtOH, CH_3CN, and DMSO-H_2O, among which EtOH shows excellent sensitivity. The effect of water content in ethanol on selectivity was further determined. It should be noted that, the fluorescence enhancement of **B1** depends on the fraction of water. When gradually increased the fraction of aqueous in EtOH from 10% to 90%, fluorescence intensity of **B1** were gradually decreased. Therefore, this mixture of solvents at 10% aqueous fraction was selected for further study.
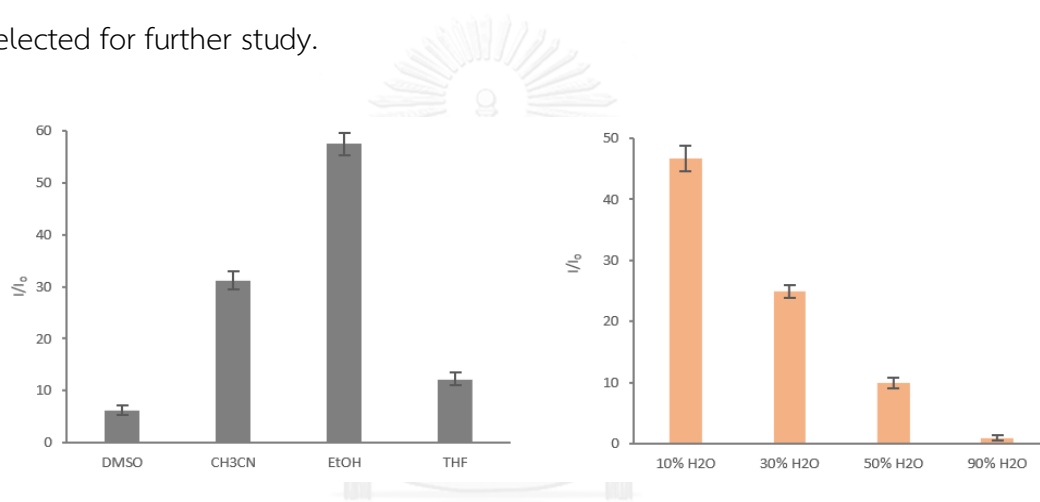
Figure 3.22 Relative fluorescence responses of **B1**-Zn^{2+} complex in the presence of various solvents and water fractions in EtOH

The binding properties of **B1**-**B4** with Zn^{2+} was investigated by UV-vis absorption titration in EtOH-H_2O (9:1, v/v) at room temperature. The UV-vis spectra of free **B1** and **B2** with Zn^{2+} were given in Figure 3.23, which showed the similar spectral shapes and exhibited two absorption regions with band about at 243 nm and 318 nm. Upon titration with Zn^{2+}, these peaks red-shift to 260 and 361 nm, respectively. Similarly, a significant red-shift of absorption band at 389 nm to 418 nm were observed in **B3** and **B4** as shown in Figure 3.23. These new absorbance band might be attributed to the coordination interaction between Zn^{2+} and fluorophores.
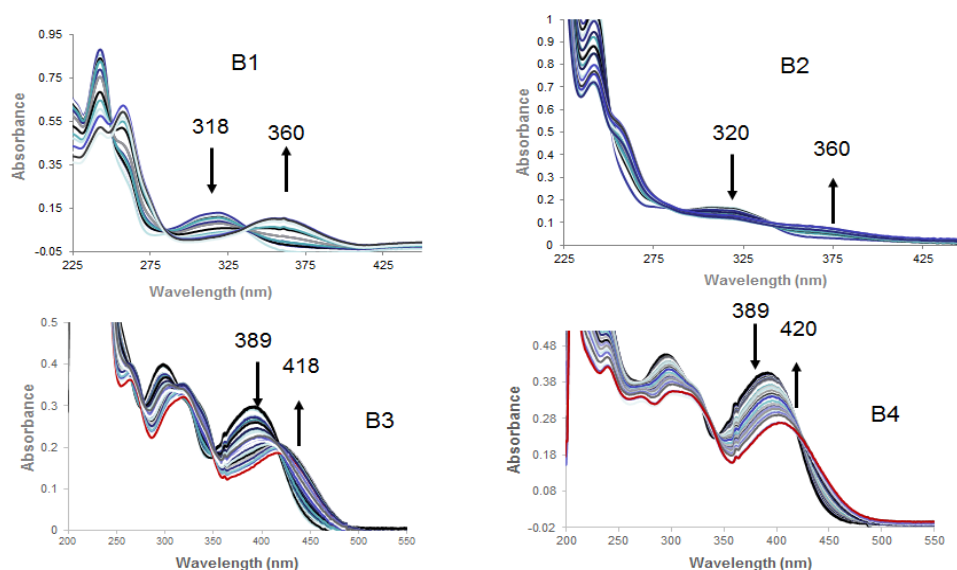
Figure 3.23 Absorption titration spectra of **B1**-**B4** (20 µM) upon addition of various concentrations of Zn^{2+}.

The effect of pH on the fluorescence emission of free fluorophores (**B1**-**B4**) and their complexes with Zn^{2+} were investigated to evaluate their potential applicability. As shown in Figure 3.24, there was no significant difference fluorescence response of sensors under different pH conditions, acidic, neutral and alkaline conditions (pH 4–10). Upon addition of Zn^{2+}, the fluorescent signals were enhanced. However, protonation of nitrogen heterocyclic in aminoquinoline moiety induced their chelation ability to Zn^{2+} decrease and a small increase in fluorescence intensity upon addition of Zn^{2+} in acidic condition. The fluorescence intensity of the complexs increase reaching a steady high reading at around pH 7.0. On the other hand, due to the formation of the less soluble $Zn(OH)_2$ in alkali conditions, fluorescence of the complexs slightly decrease with the increase of pH from 9.0 to 10.0. These results indicate the potential applicability of sensors for Zn^{2+} detection in a wide pH range, covering the physiological pH window. Therefore, subsequent metal binding studies were carried out in HEPES buffer solution at pH = 7.4.
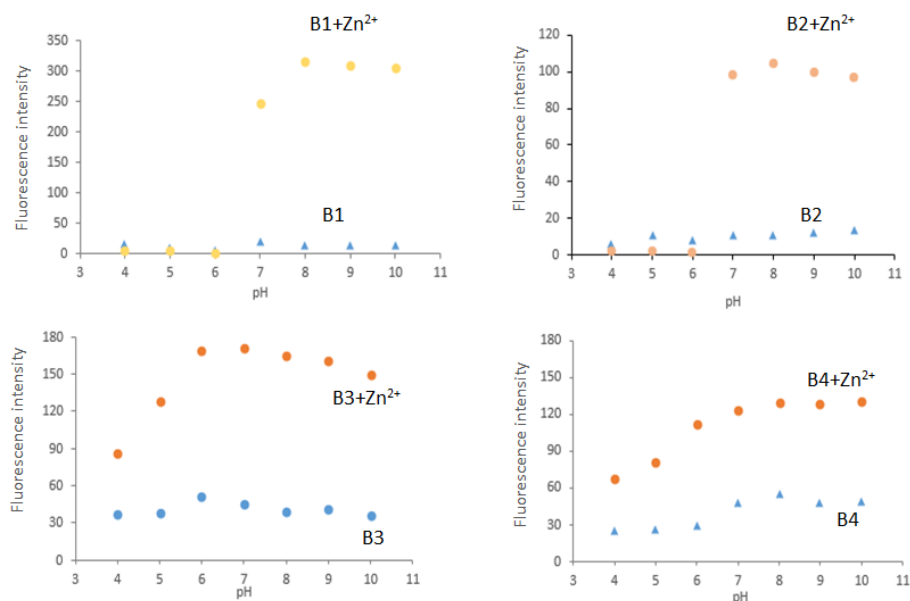
Figure 3.24 Fluorescence intensity of **B1-B4** (20 μM) at various pH in the absence and presence of 10 equiv. Zn^{2+}.

Free fluorphore solutions display weak fluorescence emissions. For example, a weak emission band at 391 nm typical of the aminoquinoline moiety with low fluorescence quantum yield efficiency (Φ_F = 0.0020) of **B1** was observed when excited at 318 nm, this can be attributed to the photoinduced electron transfer (PET) from the amide N atom to the excited singlet state of quinoline [26] and the C=N bond isomerization in the excited state of **B1**. On addition of Zn^{2+} to **B1** solution, the emission at 391 nm of **B1** gradually decreased accompanied with the new appearance of a strong emission band at 535 nm and a remarkable red shift of 144 nm. The Zn^{2+} binding convinced emission enhancement may come from the chelation-enhanced fluorescence (CHEF) effect, which inhibits the PET process and the C=N bond isomerization. After binding metal ions, the intramolecular hydrogen bond of 8-aminoquinoline is broken, and the intramolecular electron-transfer process is forbidden [123], thus enhancing fluorescence emission. Simultaneously, the deprotonation process strengthens the electron-donating ability from the nitrogen atom of the 8-amino group to the quinoline ring. And the electron transfer from the nitrogen atom of the heterocycle to the metal ion further enhances the ICT process.

As a result, a red-shift in both emission and absorption wavelength could be observed [21, 124-126].

Subsequently, fluorescence titration of **B1** by increasing amounts of Zn^{2+} was examined (Figure 3.25). Upon gradual addition of Zn^{2+}, fluorescence changes were observed. The original emission intensity at 391 nm was gradually decreased along with a new red-shift emission band at 535 nm. The intensity ratios at 535 and 391 nm (I_{535} nm/I_{391} nm) increase until the addition of 3 equiv. Zn^{2+} (for **B1** and **B2**) and 2 equiv. Zn^{2+} (for **B3** and **B4**). Moreover, a good linearity between the fluorescence intensity ratios and the concentrations of Zn^{2+} is obtained in the range of 0 - 20 μM (Figure 3.26). From above data, the detection limit of **B1**-**B4** to Zn^{2+} were calculated to be 0.024, 0.276, 0.370, and 0.431 μM, respectively.

A Job's plot analysis was conducted for quantifying the stoichiometry of the complex of fluorophores (**B1**-**B4**) and Zn^{2+}. As shown in Figure 3.27, when molar factions of Zn^{2+} was plotted against fluorescence intensity, the maximum point was observed at a mole fraction of 0.5 for all compounds, which means fluorophore binds Zn^{2+} with a 1:1 stoichiometry. To support above data, the binding between **B1**-**B4** and Zn^{2+} were carried out further by the MALDI-TOF-MS spectroscopic data. In Figure 3.28, the clear m/z peak of all compounds appeared at 381.526, 383.532, 524.807, and 526.854, respectively, which corresponds to the formation of 1:1 complex of each fluorophore with Zn^{2+}. For more information, the binding affinity between fluorophore and Zn^{2+} was determined by Benesi–Hildebrand analysis of the titration profiles based on 1:1 binding mode resulted in a linearity (Figure 3.29), and the association constant (K_a) for Zn^{2+} binding to each fluorophore was calculated to be 7.0×10^3, 7.4×10^3, 1.1×10^4, and 1.2×10^4 M^{-1}, respectively.
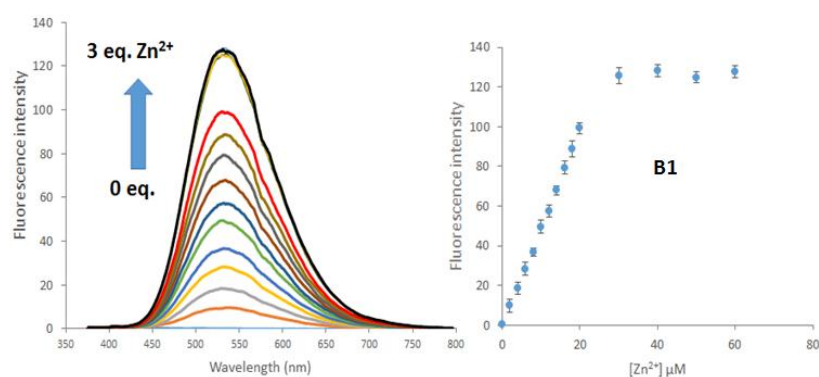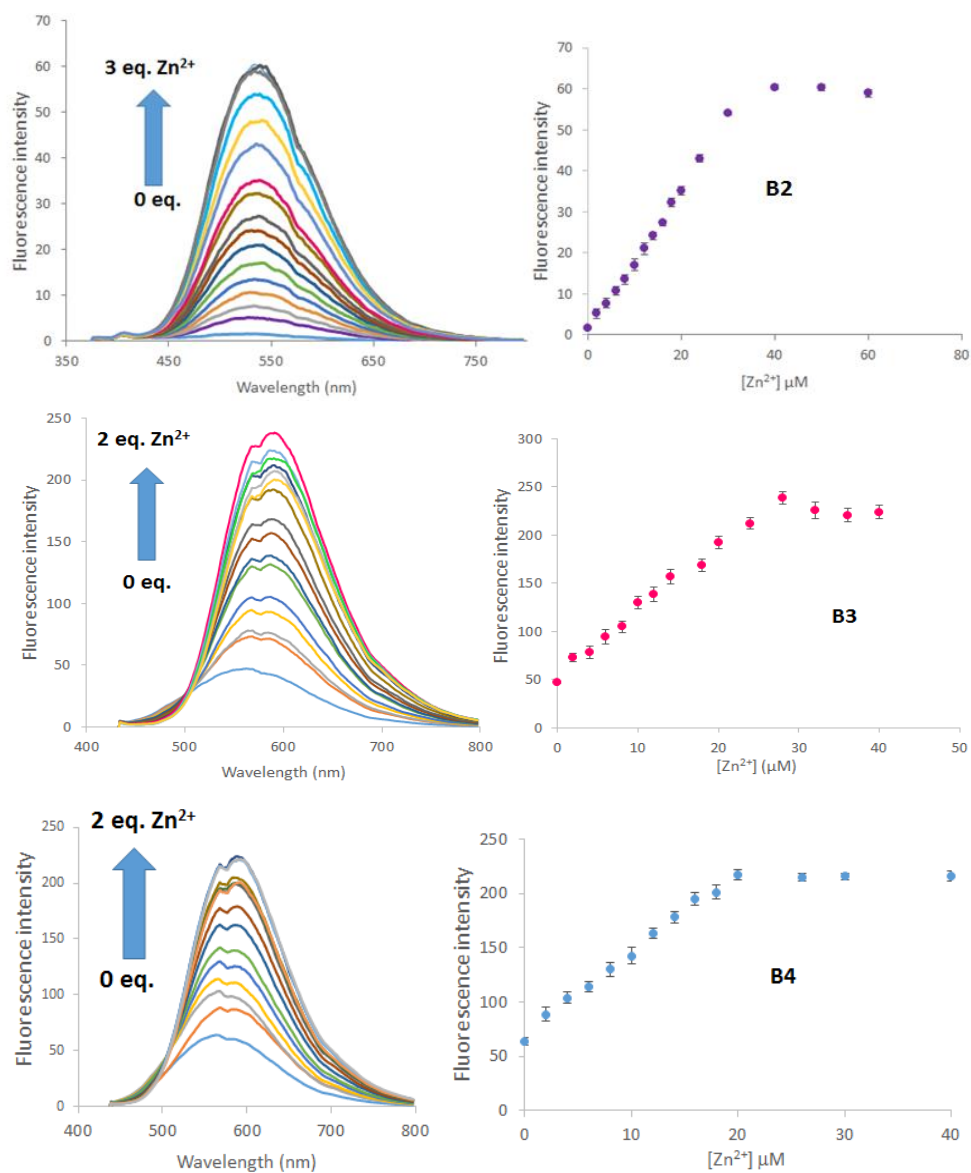
Figure 3.25 Fluorescence titration spectra of **B1**-**B4** (20 µM) upon addition of various concentrations of Zn^{2+}
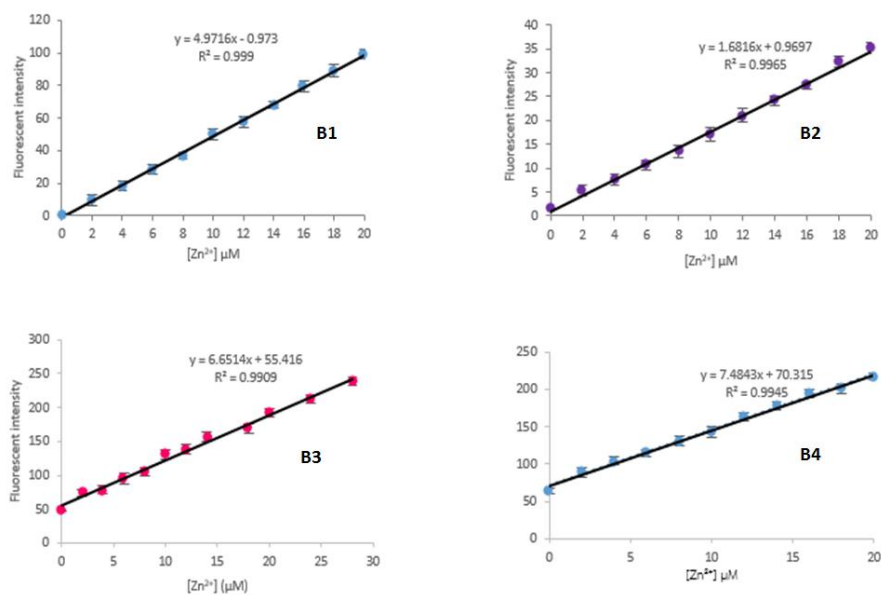
Figure 3.26 Linear calibration lines of **B1**-**B4** for quantitative determination of Zn^{2+} concentration.
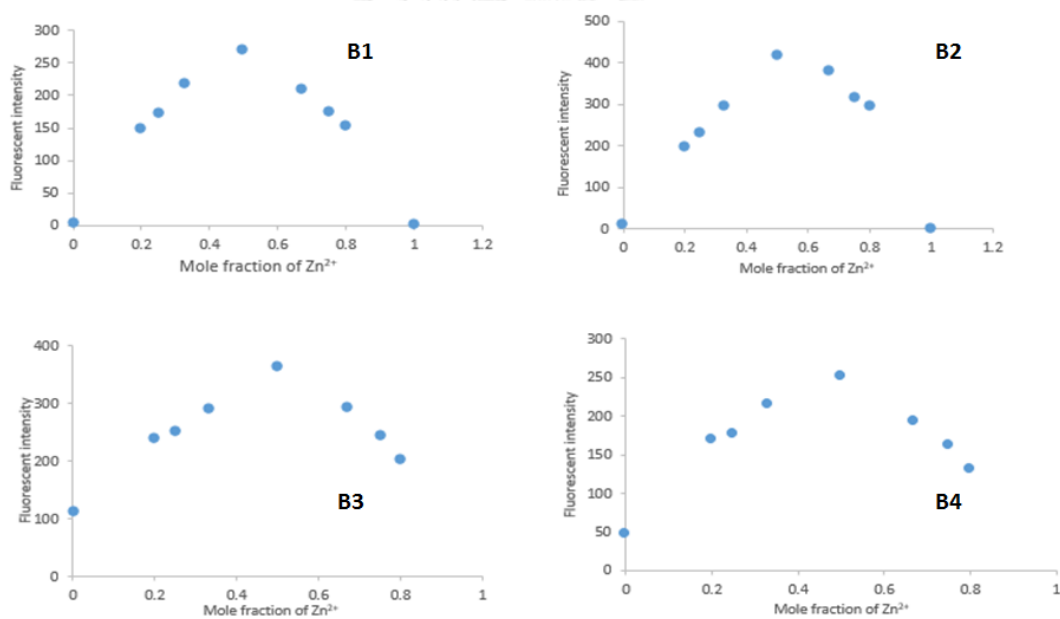
Figure 3.27 The Job's plot investigated between Zn^{2+} and sensors by fluorescence spectroscopy.
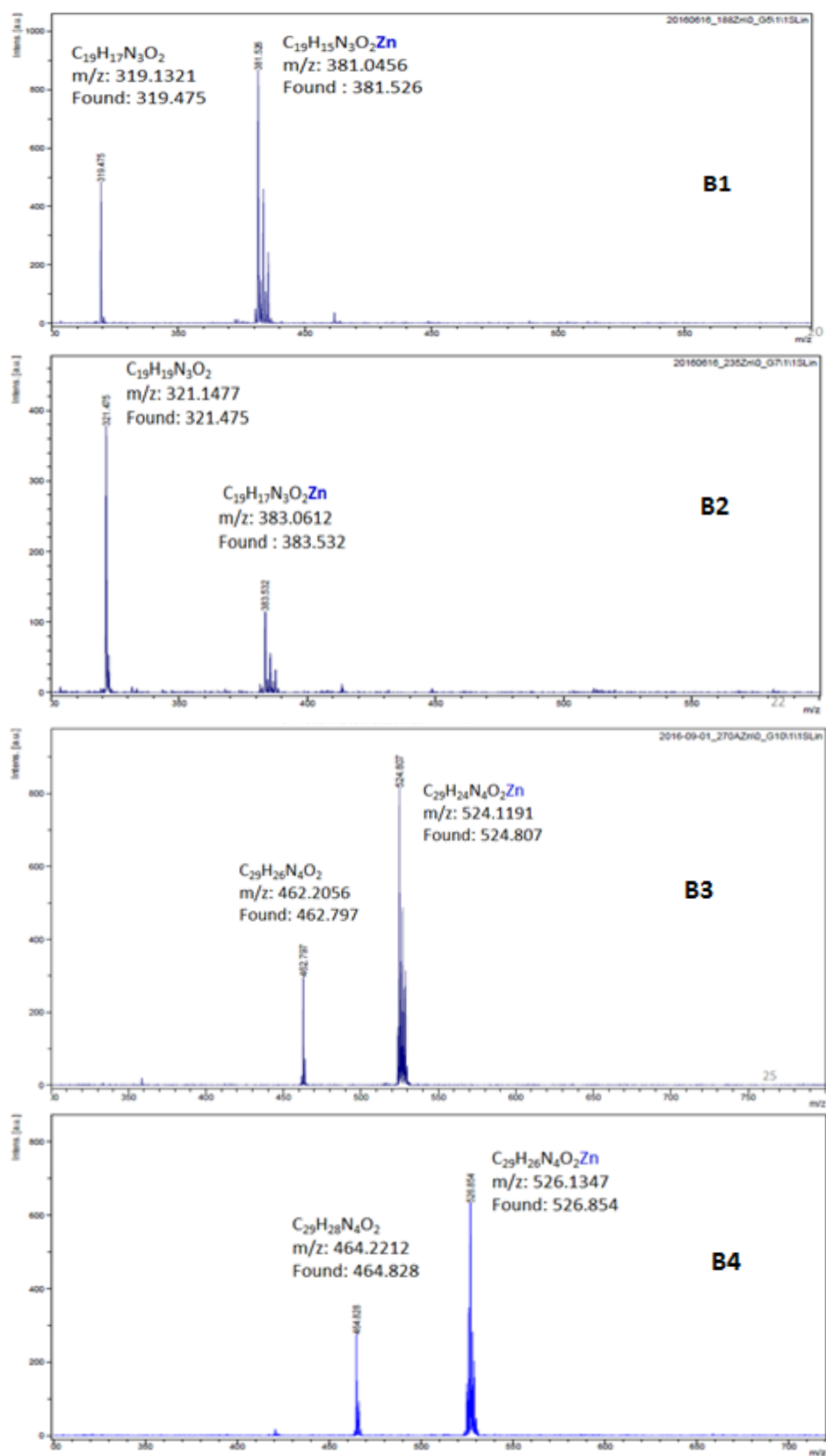
Figure 3.28 MALDI-TOF-MS spectra of **B1**-**B4** with Zn^{2+}
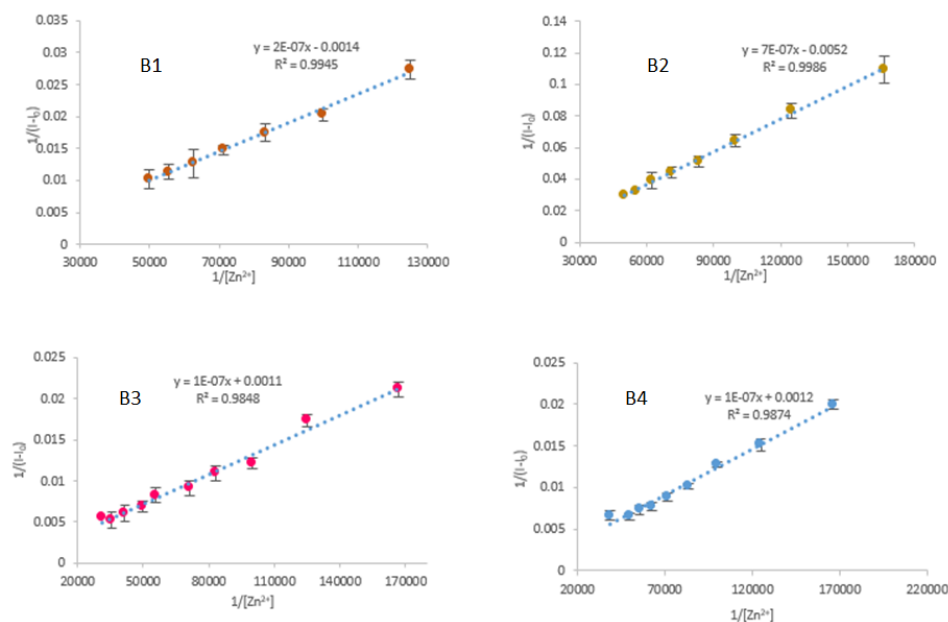
Figure 3.29 Benesi-Hildebrand plots of **B1**-**B4**

For a further study the complexation of fluorophores with Zn^{2+}, ^1H NMR titration were conducted in DMSO-d_6 (Figure 3.30). For instance, the presence of 1.0 equiv. of Zn^{2+} in **B1** solution, the proton of imine (b) was shifted upfield, which was ascribed to the increase in the electron density of the imine moiety upon coordination with metal ion. As for the phenolic fragment, aromatic protons (m,o) display a small upperfield shift accompanied with the disappearance of hydroxyl proton (a) at 13.4 ppm which account for deprotonation of hydroxyl proton and its involvement in metal chelation. On the other hand, the proton signals of quinoline ring were slightly shifted to downfield that mean the nitrogen atom from the pyridyl group was bonded to Zn^{2+}. Besides, amide NH (e) was also disappeared because of deprotonation upon addition of Zn^{2+}. Upon addition of 1.0 equiv. Zn^{2+} to **B2** in DMSO-d_6 solution, all aromatic protons of quinoline moiety were also shifted to downfield as well as protons of phenolic moiety were slightly shifted to upfield. Moreover, deprotonation of hydroxyl OH and amide NH was also observed. The result suggested that oxygen atom, heterocyclic nitrogen atom, and amide nitrogen atom probably involved in metal chelation.
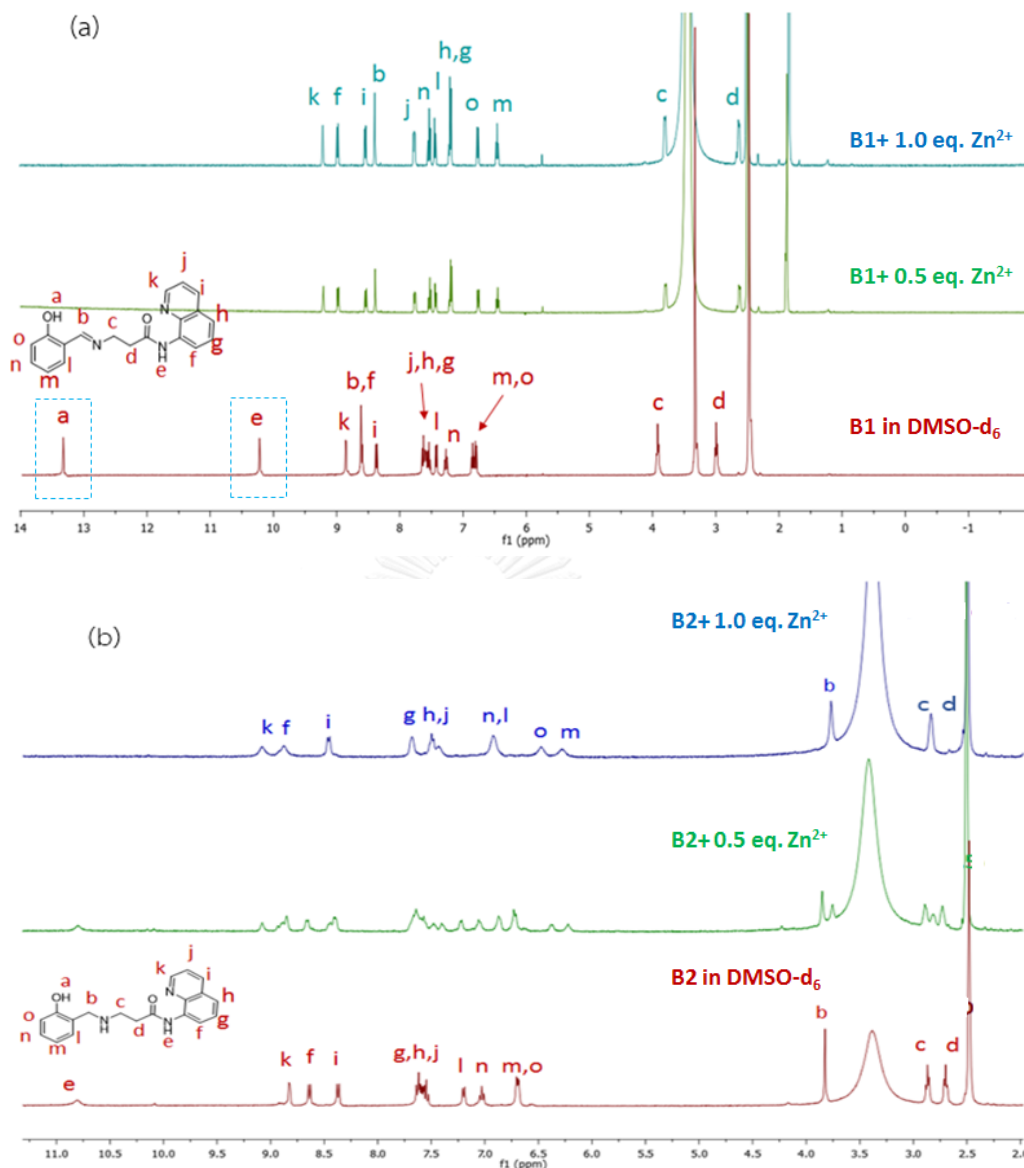
Figure 3.30 ^{1}H NMR titration spectra of **B1** (a) and **B2** (b) in the presence of various equivalents of Zn^{2+}.

For in-depth understanding of the binding mechanism of sensors with Zn^{2+}, we synthesized the crystal of the complex between **B1** and Zn^{2+}. The crystal structure of **B1**-Zn^{2+} complex along with atom numbering scheme at metal coordination sphere is depicted in Figure 3.31. It crystallizes in the monoclinic system with space group P2/n from methanol solvent. Details of crystal data are summarized in Table 3.5, while important bond lengths and angles are given in Table 3.6. The Zn^{2+} ion is four-coordinate with one oxygen atom and three nitrogen atoms

through two deprotonatations of **B1** ligand (amide NH and phenolic proton OH) which lead a distorted ZnON$_3$ coordination environment. The crystal structure shows probably a seesaw geometry around Zn^{2+} center bonded with a receptor. The metal is coordinated to the ligand through the pyridyl nitrogen atom in the quinoline moiety (N3), amide nitrogen atom (N2), imine nitrogen (N1), and the phenolic oxygen atom (O1), forming five-membered (Zn-N2-C11-C16-N3) and two six-membered (Zn-O1-C1-C6-C7-N1) and (Zn-N1-C8-C9-C10-N2) chelate ring. The obvious red shift as well as fluorescence intensity increase upon Zn^{2+} addition can be explained by the binding of sensor to Zn^{2+} produces a five-membered and two six-membered chelate ring, which form a nearly planar structure conformation and a large π-electron conjugation system. Simultaneously, Zn^{2+} induced deprotonation strengthens of the 8-amino residue and hydroxy group in phenolic proton. These deprotonation processes convince electron transfer and further enhance intramolecular charge transfer (ICT).
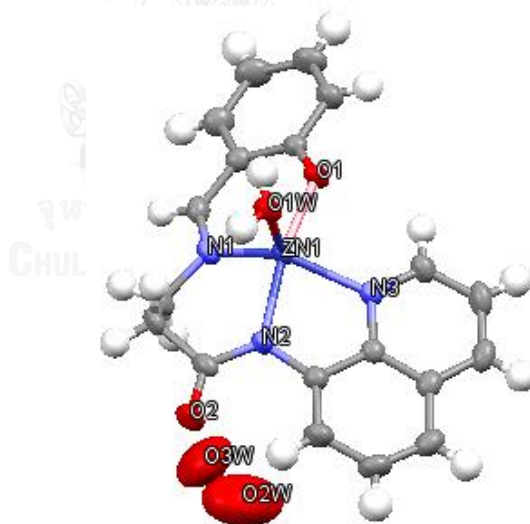
Figure 3.31 X-ray crystal structure of the chemical sensor **B1**-Zn^{2+} complex.

Table 3.5 Crystallographic data for F1–Zn complex

	B1-Zn complex
Empirical formula	$C_{19}H_{15}N_3O_2$**Zn**
Formula weight	381.526
Space group	P 2/n
a (Å)	12.5047(6)
b (Å)	8.6093(4)
c (Å)	16.3830(7)
α (°)	90
β (°)	92.699(1)
γ (°)	90
V (A^3)	1761.78

Table 3.6 Selected bond lengths (Å) and angles (°) for **B1**–Zn complex

	Bond lengths and angle ($^\circ$)
Zn-O1	2.0142
Zn-O1W	2.0523
Zn-N1	2.0544
Zn-N2	2.0804
Zn-N3	2.0949
O1-Zn-O1W	90.85
O1-Zn-N1	90.62
O1-Zn-N2	169.05
O1-Zn-N3	90.56
O1W-Zn-N1	114.08
O1W-Zn-N2	96.81
O1W-Zn-N3	109.88
N1-Zn-N2	93.36

N1-Zn-N3	136.0
N2-Zn-N3	79.49

Fluorescence competition experiments were then conducted to further validate the high selectivity of sensors to Zn^{2+}. As shown in Figure 3.32, the solutions containing Zn^{2+} and various background metal ions, except for Co^{2+}, Ni^{2+}, Cu^{2+}, Fe^{2+}, and Fe^{3+}, showed high fluorescence enhancement similar to that of Zn^{2+} alone. It is noteworthy that the biologically important metal ions of Ca^{2+}, Mg^{2+}, K^+, and Na^+ did not cause any disturbance even they were used as 100 equiv. However, these free cations yielded no false positive signals in the Zn^{2+} measurement because of their fluorescence quenching properties. In addition, they would have little influence because they are present at very low concentration in vivo.
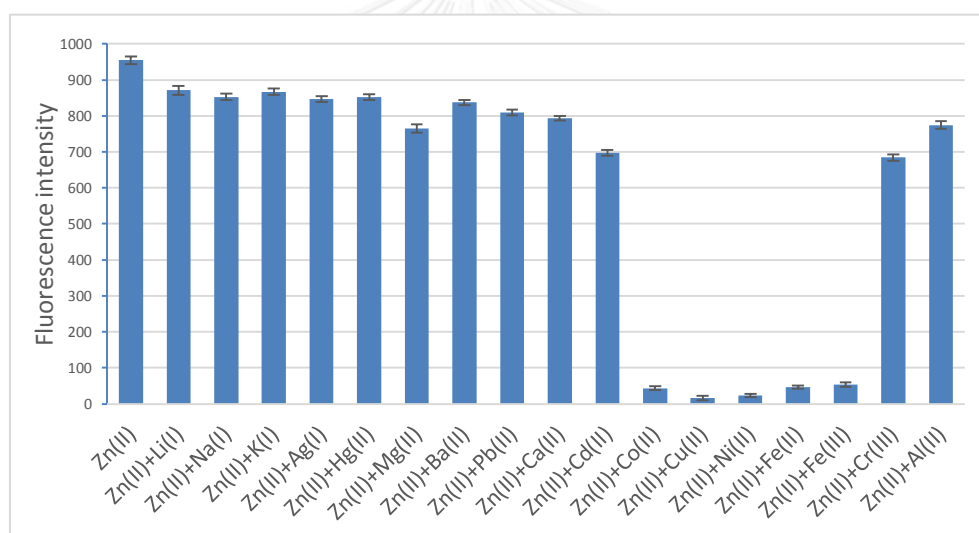
Figure 3.32 Fluorescence responses of **B1** (20 μM) to the addition of Zn^{2+} (10 equivalent) mixed with various metal ions (100 equivalent).

As for reversibility studies, it would be interesting to see whether the enhanced fluorescence signal could be completely restored to initial intensity of sensors (20 μM) by addition of a strong Zn^{2+} chelator. Ethylenediamine tetracarboxylic acid (EDTA) was chosen for this purpose as its complexation constant to Zn^{2+} is extremely high (log K_1 = 16.5). On gradual addition of EDTA, fluorescent intensity of complexes gradually decreases due to chelation of Zn^{2+} with EDTA releasing free sensors. For example, the fluorescence emission restored to initial intensity of **B1** (20 μM) by adding EDTA (140 μM) after **B1** was saturated with Zn^{2+}

(Figure 3.33). For other sensors, the signal could be fully restored when the amount of EDTA was approximately 140 μM.
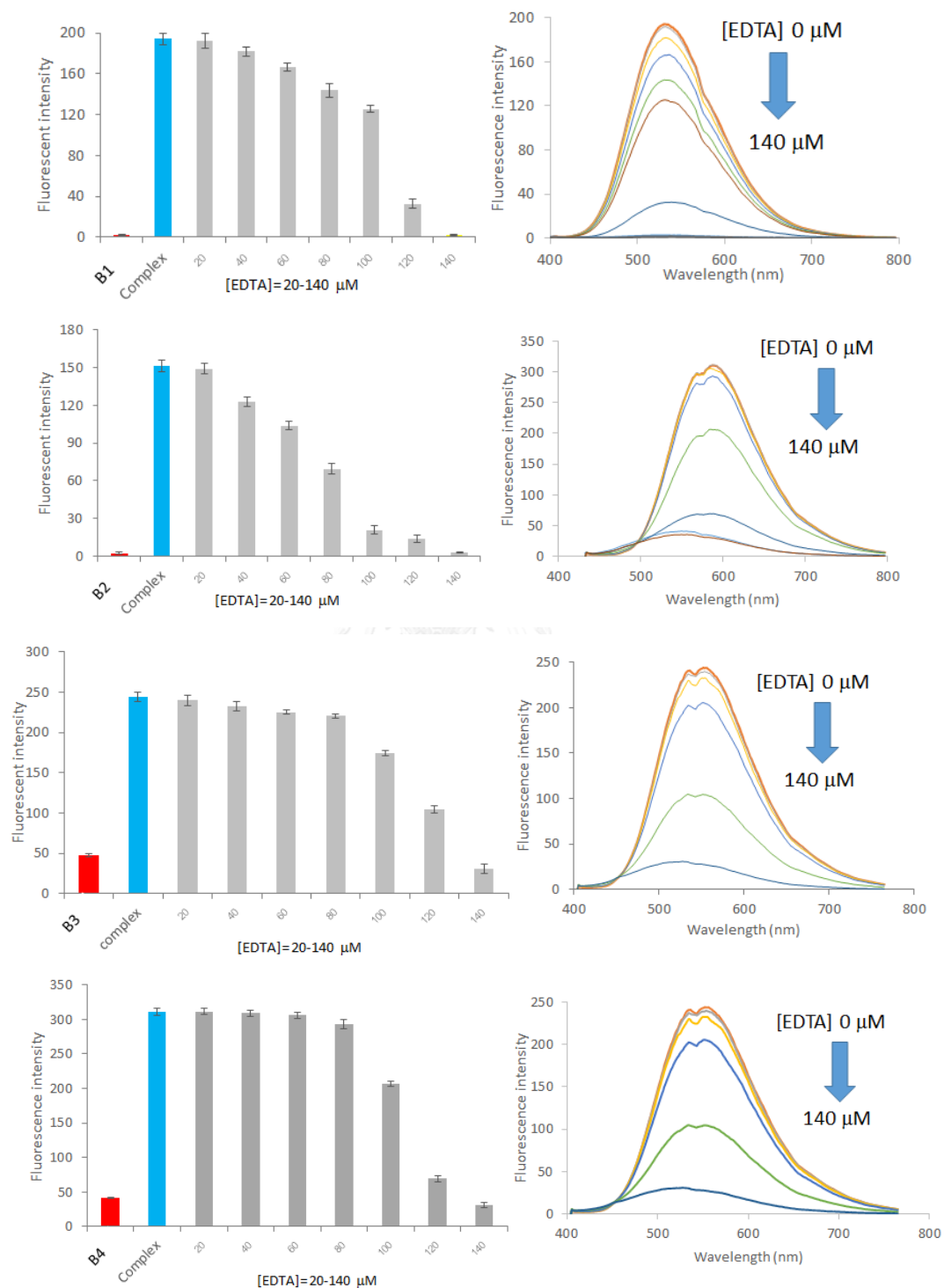
Figure 3.33 Fluorescence signal restoration of **B1**-**B4** by EDTA

CHAPTER IV

CONCLUSIONS

4.1 Conclusion of part A: Glucosamine sensing

In conclusion, we have successfully synthesized three amidoquinoline-naphthalimide dyads, two of which exhibit outstanding selective fluorescence enhancement towards glucosamine. To the best of our knowledge, their association constants with glucosamine at 1.55×10^4 and 1.45×10^4 are the current highest. The proposed sensing mechanism involving the inhibition of PET process between the amidoquinoline and naphthalimide moeities was verified by determination of HOMO-LUMO energy levels using linear sweep voltammetry. We have also demonstrated the use of our compound as a glucosamine probe in living Caco-2 cells. Under the fluorescence microscope, it is apparent that this probe can be used for the qualitative detection of intracellular glucosamine in Caco-2 cells internalized by glucosamine at 1 mM and higher. The application of this fluorescent probe should allow real-time quantitative monitoring of glucosamine level in living Caco-2 cells for the study of bioavailability and permeability enhancement.

4.2 Conclusion of part B: Zn^{2+} sensing

A series of 8-amidoquinoline was successfully synthesized and developed for selectively turn-on detection of Zn^{2+} by extension of the π-conjugated system on the quinoline ring and incorporation of either the salicylaldimine or its reduced amino form. The study illustrates that addition of the salicylaldimine group could induce not only a large CHEF in the complex binding chelation, but also involve in a chelation ring with Zn^{2+} to form a nearly seesaw structure conformation, which was verified by x-ray crystallography. The sensing mechanism is verified by ^{1}H-NMR titration, Mass Spectrometry, and the X-ray crystal structure of the sensor with salicylaldimine and unsubstituted aminoquinoline, which suggests a 1:1 binding stoichiometry between this fluorophore and zinc ion. The detection limits of 0.024 to 0.431 µM and the association constants ranging from 7.0×10^3 to 1.2×10^4 M^{-1} are estimated for the four sensors.

REFERENCES

[1]   Lakowicz, J.R. Principles of Fluorescence Spectroscopy 3rd ed. News York:
        Springer Science, 2006.

[2]   Gunnlaugsson, T., et al. Fluorescent Photoinduced Electron Transfer (PET)
        Sensors for Anions; From Design to Potential Application. Journal of
        Fluorescence 15(3) (2005): 287-299.

[3]   Callan, J.F., de Silva, A.P., and Magri, D.C. Luminescent sensors and switches in
        the early 21st century. Tetrahedron 61(36) (2005): 8551-8588.

[4]   Silva, A.P.d., et al. Signaling Recognition Events with Fluorescent Sensors and
        Switches. Chemical Reviews 97(5) (1997): 1515–1566.

[5]   Martínez-Máñez, R. and Sancenón, F. Fluorogenic and Chromogenic
        Chemosensors and Reagents for Anions. Chemical Reviews 103(11) (2003):
        4419-4476.

[6]   Valeur, B. and Leray, I. Design principles of fluorescent molecular sensors for
        cation recognition. Coordination Chemistry Reviews 205(1) (2000): 3-40.

[7]   Xu, Z., Yoon, J., and Spring, D.R. Fluorescent chemosensors for Zn2+.
        Chemical Society Reviews 39(6) (2010): 1996-2006.

[8]   Kim, J.S. and Quang, D.T. Calixarene-Derived Fluorescent Probes. Chemical
        Reviews 107(9) (2007): 3780-3799.

[9]   Sapsford, K.E., Berti, L., and Medintz, I.L. Materials for Fluorescence Resonance
        Energy Transfer Analysis: Beyond Traditional Donor–Acceptor Combinations.
        Angewandte Chemie International Edition 45(28) (2006): 4562-4589.

[10]   Carlson, H.J. and Campbell, R.E. Genetically encoded FRET-based biosensors
        for multiparameter fluorescence imaging. Current Opinion in Biotechnology
        20(1) (2009): 19-27.

[11]   Wu, J., Liu, W., Ge, J., Zhang, H., and Wang, P. New sensing mechanisms for
        design of fluorescent chemosensors emerging in recent years. Chemical
        Society Reviews 40(7) (2011): 3483-3495.

[12] Peng, X., Wu, Y., Fan, J., Tian, M., and Han, K. Colorimetric and Ratiometric Fluorescence Sensing of Fluoride: Tuning Selectivity in Proton Transfer. The Journal of Organic Chemistry 70(25) (2005): 10524-10531.

[13] Wu, J.-S., et al. Fluorescence Turn On of Coumarin Derivatives by Metal Cations: A New Signaling Mechanism Based on C=N Isomerization. Organic Letters 9(1) (2007): 33-36.

[14] Hong, Y., Lam, J.W.Y., and Tang, B.Z. Aggregation-induced emission: phenomenon, mechanism and applications. Chemical Communications (29) (2009): 4332-4353.

[15] Wang, M., Zhang, G., Zhang, D., Zhu, D., and Tang, B.Z. Fluorescent bio/chemosensors based on silole and tetraphenylethene luminogens with aggregation-induced emission feature. Journal of Materials Chemistry 20(10) (2010): 1858-1867.

[16] Yang, G., Morlet-Savary, F., Peng, Z., Wu, S., and Fouassier, J.-P. Triplet-triplet absorption of 2-(2′-hydroxyphenyl) benzoxazole (HBO) in polar solvents. Chemical Physics Letters 256(4–5) (1996): 536-542.

[17] Li, Z. and Wu, S. The effect of molecular structure on the photophysical behavior of substituted styryl pyrazine derivatives. Journal of Fluorescence 7(3) (1997): 237-242.

[18] Henary, M.M. and Fahrni, C.J. Excited State Intramolecular Proton Transfer and Metal Ion Complexation of 2-(2'-Hydroxyphenyl)benzazoles in Aqueous Solution. The Journal of Physical Chemistry A 106(21) (2002): 5210-5220.

[19] Frederickson, C.J., Kasarskis, E.J., Ringo, D., and Frederickson, R.E. A quinoline fluorescence method for visualizing and assaying the histochemically reactive zinc (bouton zinc) in the brain. J Neurosci Methods 20(2) (1987): 91-103.

[20] Zalewski, P.D., et al. Video image analysis of labile zinc in viable pancreatic islet cells using a specific fluorescent probe for zinc. J Histochem Cytochem 42(7) (1994): 877-84.

[21]   Zhang, Y., Guo, X., Si, W., Jia, L., and Qian, X. Ratiometric and Water-Soluble Fluorescent Zinc Sensor of Carboxamidoquinoline with an Alkoxyethylamino Chain as Receptor. Organic Letters 10(3) (2008): 473-476.

[22]   He, C., Qian, X., Xu, Y., Yang, C., Yin, L., and Zhu, W. A ratiometric fluorescent probe for oxalate based on alkyne-conjugated carboxamidoquinolines in aqueous solution and imaging in living cells. Dalton Transactions 40(5) (2011): 1034-1037.

[23]   Pal, P., Rastogi, S.K., Gibson, C.M., Aston, D.E., Branen, A.L., and Bitterwolf, T.E. Fluorescence Sensing of Zinc(II) Using Ordered Mesoporous Silica Material (MCM-41) Functionalized with N-(Quinolin-8-yl)-2-[3-(triethoxysilyl)propylamino]acetamide. ACS Applied Materials & Interfaces 3(2) (2011): 279-286.

[24]   Zhou, X., et al. Ratiometric fluorescent Zn2+ chemosensor constructed by appending a pair of carboxamidoquinoline on 1,2-diaminocyclohexane scaffold. Tetrahedron 67(19) (2011): 3412-3419.

[25]   Sutariya, P.G., Modi, N.R., Pandya, A., Joshi, B.K., Joshi, K.V., and Menon, S.K. An ICT based "turn on/off" quinoline armed calix[4]arene fluoroionophore: its sensing efficiency towards fluoride from waste water and Zn2+ from blood serum. Analyst 137(23) (2012): 5491-5494.

[26]   Dong, Z., Guo, Y., Tian, X., and Ma, J. Quinoline group based fluorescent sensor for detecting zinc ions in aqueous media and its logic gate behaviour. Journal of Luminescence 134 (2013): 635-639.

[27]   Du, J., Fan, J., Peng, X., Li, H., and Sun, S. The quinoline derivative of ratiometric and sensitive fluorescent zinc probe based on deprotonation. Sensors and Actuators B: Chemical 144(1) (2010): 337-341.

[28]   Xie, G., et al. A Highly Zinc(II)-Selective Fluorescent Sensor Based on 8-Aminoquinoline and Its Application in Biological Imaging. European Journal of Inorganic Chemistry 2011(19) (2011): 2927-2931.

[29]   Li, X.-B., Chen, J.-Y., Niu, Z.-G., and Wang, E.-J. Quinoline based fluorescent chemosensor for Zn2+ in water. in Indian Journal of Chemistry. 2014. 1349-1352.

[30] You, Q.-H., et al. A quinolinyl antipyrine based fluorescence sensor for Zn2+ and its application in bioimaging. RSC Advances 2(29) (2012): 11078-11083.

[31] Ma, Y., Wang, F., Kambam, S., and Chen, X. A quinoline-based fluorescent chemosensor for distinguishing cadmium from zinc ions using cysteine as an auxiliary reagent. Sensors and Actuators B: Chemical 188 (2013): 1116-1122.

[32] Gu, L., Wan, X., Liu, H., Liu, T., and Yao, Y. A novel ratiometric fluorescence sensor for Zn2+ detection. Analytical Methods 6(21) (2014): 8460-8463.

[33] Zhou, X., Li, P., Shi, Z., Tang, X., Chen, C., and Liu, W. A Highly Selective Fluorescent Sensor for Distinguishing Cadmium from Zinc Ions Based on a Quinoline Platform. Inorganic Chemistry 51(17) (2012): 9226-9231.

[34] Ma, Y., et al. A highly sensitive and selective ratiometric fluorescent sensor for Zn2+ ion based on ICT and FRET. Dyes and Pigments 102 (2014): 301-307.

[35] Yue, Y., Dong, Q., Zhang, Y., Sun, Y., and Gong, Y. A highly selective "turn-on" fluorescent chemosensor based on 8-aminoquinoline for detection of Zn2+. Analytical Methods 7(13) (2015): 5661-5666.

[36] Jia, X., et al. A highly selective copper fluorescent indicator based on aminoquinoline substituted BODIPY. Dyes and Pigments 98(2) (2013): 195-200.

[37] Zhang, L., Sun, J., Liu, S., Cui, X., Li, W., and Fang, J. Aminoquinoline-based fluorescent probe for detection of Cu2 + and hydrogen sulfide. Inorganic Chemistry Communications 35 (2013): 311-314.

[38] Jang, Y.J., Yeon, Y.H., Yang, H.Y., Noh, J.Y., Hwang, I.H., and Kim, C. A colorimetric and fluorescent chemosensor for selective detection of Cr3 + and Al3 +. Inorganic Chemistry Communications 33 (2013): 48-51.

[39] Park, H.M., et al. Fluorescent chemosensor based-on naphthol–quinoline for selective detection of aluminum ions. Tetrahedron Letters 52(43) (2011): 5581-5584.

[40] Zhou, X., Yan, W., Zhao, T., Tian, Z., and Wu, X. Rhodamine based derivative and its zinc complex: synthesis and recognition behavior toward Hg(II). Tetrahedron 69(46) (2013): 9535-9539.

[41]   Cheng, R., et al. Optical Turn-On Sensor Based on Graphene Oxide for Selective Detection of d-Glucosamine. Analytical Chemistry 84(13) (2012): 5641-5644.

[42]   Roos, M.D., Han, I.O., Paterson, A.J., and Kudlow, J.E. Role of glucosamine synthesis in the stimulation of TGF-alpha gene transcription by glucose and EGF. Am J Physiol 270(3 Pt 1) (1996): C803-11.

[43]   Reginster, J.-Y., Neuprez, A., Lecart, M.-P., Sarlet, N., and Bruyere, O. Role of glucosamine in the treatment for osteoarthritis. Rheumatology International 32(10) (2012): 2959-2967.

[44]   Hussain, M. A case for glucosamine. European Journal of Endocrinology 139(5) (1998): 472-475.

[45]   Fransen, M., et al. Glucosamine and chondroitin for knee osteoarthritis: a double-blind randomised placebo-controlled clinical trial evaluating single and combination regimens. Annals of the Rheumatic Diseases 74(5) (2015): 851-858.

[46]   McAlindon, T.E., et al. OARSI guidelines for the non-surgical management of knee osteoarthritis. Osteoarthritis and Cartilage 22(3) (2014): 363-388.

[47]   Friedman, S.J. and Skehan, P. Membrane-active drugs potentiate the killing of tumor cells by D-glucosamine. Proceedings of the National Academy of Sciences of the United States of America 77(2) (1980): 1172-1176.

[48]   Krug, E., Zweibaum, A., Schulz-Holstege, C., and Keppler, D. D-glucosamine-induced changes in nucleotide metabolism and growth of colon-carcinoma cells in culture. Biochemical Journal 217(3) (1984): 701-708.

[49]   Liu, B.-Q., et al. Glucosamine induces cell death via proteasome inhibition in human ALVA41 prostate cancer cell. Exp Mol Med 43 (2011): 487-493.

[50]   Sanches-Silva, A., et al. Ultra-high pressure LC determination of glucosamine in shrimp by-products and migration tests of chitosan films. Journal of Separation Science 35(5-6) (2012): 633-640.

[51]   Zhou, J.Z., Waszkuc, T., and Mohammed, F. Determination of Glucosamine in Raw Materials and Dietary Supplements Containing Glucosamine Sulfate and/or Glucosamine Hydrochloride by High-Performance Liquid

Chromatography with FMOC-Su Derivatization: Collaborative Study. Journal of AOAC International 88(4) (2005): 1048-1058.

[52] Ji, D., Zhang, L., Chen, J., and Peng, E. Precolumn Derivatization Liquid Chromatography Method for Analysis of Dietary Supplements for Glucosamine: Single Laboratory Validation Study. Journal of AOAC International 88(2) (2005): 413-417.

[53] Shen, X., Yang, M., and Tomellini, S.A. Liquid chromatographic analysis of glucosamine in commercial dietary supplements using indirect fluorescence detection. Journal of Chromatographic Science 45(2) (2007): 70-75.

[54] Pastorini, E., et al. Development and validation of a HPLC–ES-MS/MS method for the determination of glucosamine in human synovial fluid. Journal of Pharmaceutical and Biomedical Analysis 50(5) (2009): 1009-1014.

[55] Hubert, C., et al. Development and validation of a sensitive solid phase extraction/hydrophilic interaction liquid chromatography/mass spectrometry method for the accurate determination of glucosamine in dog plasma. Journal of Chromatography A 1217(19) (2010): 3275-3281.

[56] Song, M., Hang, T.-J., Wang, C., Yang, L., and Wen, A.-D. Precolumn derivatization LC–MS/MS method for the determination and pharmacokinetic study of glucosamine in human plasma and urine. Journal of Pharmaceutical Analysis 2(1) (2012): 19-28.

[57] Volpi, N. Capillary electrophoresis determination of glucosamine in nutraceutical formulations after labeling with anthranilic acid and UV detection. Journal of Pharmaceutical and Biomedical Analysis 49(3) (2009): 868-871.

[58] Akamatsu, S. and Mitsuhashi, T. Development of a simple capillary electrophoretic determination of glucosamine in nutritional supplements using in-capillary derivatisation with o-phthalaldehyde. Food Chemistry 130(4) (2012): 1137-1141.

[59] Esters, V., et al. Validation of a high-performance thin-layer chromatography/densitometry method for the quantitative determination of

glucosamine in a herbal dietary supplement. <u>Journal of Chromatography A</u> 1112(1–2) (2006): 156-164.

[60] Sullivan, C. and Sherma, J. Development and validation of an HPTLC-densitometry method for assay of glucosamine of different forms in dietary supplement tablets and capsules. <u>Acta Chromatographica</u> 15 (2005): 119.

[61] Priya, G., Vineeta, K., Rajani, S., and Chhaya, G. Spectrophotometric method for determination of glucosamine in tablets. <u>Indian Journal of Phamaceutical Sciences</u> 68(1) (2006): 83-84.

[62] Al-arfaj, N.A. and El-Tohamy, M.F. Carbon Paste and Modified Carbon Nanotubes Paste Sensors for Determination of Reducing-Osteoarthritis Drug Glucosamine Sulphate in Bulk Powder and in its Pharmaceutical Formulations. <u>International Journal of Electrochemical Science</u> 7(11) (2012): 11023-11034.

[63] R. Cooper, C. and D. James, T. Selective d-glucosamine hydrochloride fluorescence signalling based on ammonium cation and diol recognition. <u>Chemical Communications</u> (15) (1997): 1419-1420.

[64] Cooper, C.R. and James, T.D. Synthesis and evaluation of D-glucosamine-selective fluorescent sensors. <u>Journal of the Chemical Society, Perkin Transactions 1</u> (6) (2000): 963-969.

[65] Lin, V.S.Y., Lai, C.-Y., Huang, J., Song, S.-A., and Xu, S. Molecular Recognition Inside of Multifunctionalized Mesoporous Silicas: Toward Selective Fluorescence Detection of Dopamine and Glucosamine. <u>Journal of the American Chemical Society</u> 123(46) (2001): 11510-11511.

[66] Tran, T.M., Alan, Y., and Glass, T.E. A highly selective fluorescent sensor for glucosamine. <u>Chemical Communications</u> 51(37) (2015): 7915-7918.

[67] Bojinov, V. and Grabchev, I. A new method for synthesis of 4-allyloxy-1,8-naphthalimide derivatives for use as fluorescent brighteners. <u>Dyes and Pigments</u> 51(1) (2001): 57-61.

[68] Philipova, T. and Petkov, I. Synthesis, spectral properties, and application of 1,8-naphthalimide fluorophores for modified polymers. <u>Journal of Applied Polymer Science</u> 80(11) (2001): 1863-1869.

[69]   Arunchai, R., et al. Synthesis and characterization of new triphenylamino-1,8-naphthalimides for organic light-emitting diode applications. <u>New Journal of Chemistry</u> 39(4) (2015): 2807-2814.

[70]   Choppawa, T., Sukwattanasinitt, M., Sahasithiwat, S., Ruangpornvisuti, V., and Rashatasakhon, P. Substituent effect on quantum efficiency in 4-aryloxy-N-(2′,6′-diisopropylphenyl)-1,8-naphthalimides: Experimental and computational investigations. <u>Dyes and Pigments</u> 109 (2014): 175-180.

[71]   Chinapang, P., Ruangpornvisuti, V., Sukwattanasinitt, M., and Rashatasakhon, P. Ferrocenyl derivative of 1,8-naphthalimide as a new turn-on fluorescent sensor for Au(III) ion. <u>Dyes and Pigments</u> 112 (2015): 236-238.

[72]   Dai, H. and Xu, H. Selective and Sensitive Fluorescent Chemosensors for Cu2+ Ion Based upon Bis-1,8-naphthalimide Dyads. <u>Chinese Journal of Chemistry</u> 30(2) (2012): 267-272.

[73]   Kumar, M., Kumar, N., Bhalla, V., Singh, H., Sharma, P.R., and Kaur, T. Naphthalimide Appended Rhodamine Derivative: Through Bond Energy Transfer for Sensing of Hg2+ Ions. <u>Organic Letters</u> 13(6) (2011): 1422-1425.

[74]   Lu, C., Xu, Z., Cui, J., Zhang, R., and Qian, X. Ratiometric and Highly Selective Fluorescent Sensor for Cadmium under Physiological pH Range: A New Strategy to Discriminate Cadmium from Zinc. <u>The Journal of Organic Chemistry</u> 72(9) (2007): 3554-3557.

[75]   Zhao, L.Y., et al. 1,8-Naphthalimide-based 'turn-on' fluorescent sensor for the detection of zinc ion in aqueous media and its applications for bioimaging. <u>Tetrahedron Letters</u> 54(26) (2013): 3353-3358.

[76]   Goswami, S., Aich, K., Das, A.K., Manna, A., and Das, S. A naphthalimide-quinoline based probe for selective, fluorescence ratiometric sensing of trivalent ions. <u>RSC Advances</u> 3(7) (2013): 2412-2416.

[77]   Pais, V.F., Remón, P., Collado, D., Andréasson, J., Pérez-Inestrosa, E., and Pischel, U. OFF-ON-OFF Fluorescence Switch with T-Latch Function. <u>Organic Letters</u> 13(20) (2011): 5572-5575.

[78] Liu, Z., Zhang, C., Wang, X., He, W., and Guo, Z. Design and Synthesis of a Ratiometric Fluorescent Chemosensor for Cu(II) with a Fluorophore Hybridization Approach. Organic Letters 14(17) (2012): 4378-4381.

[79] Chereddy, N.R., Thennarasu, S., and Mandal, A.B. A Photo-Induced Electron Transfer Based Chemosensor for the Selective Detection of Zn2+ Ions. Biochemistry & Analytical Biochemistry 2(1) (2013): 126-131.

[80] Zhang, X., Shen, Y., Zhang, H., Jin, J., and Zhou, S. A new bifunctional fluorescent sensor based on naphthalimide-functionalized silica nanoparticles for detection and adsorption of Cu2+ in aqueous solution. Analytical Methods 7(20) (2015): 8925-8930.

[81] Xie, X. and Smart, T.G. A physiological role for endogenous zinc in rat hippocampal synaptic neurotransmission. Nature 349(6309) (1991): 521-524.

[82] Berg, J.M. and Shi, Y. The Galvanization of Biology: A Growing Appreciation for the Roles of Zinc. Science 271(5252) (1996): 1081-1085.

[83] Vallee, B.L. and Falchuk, K.H. The biochemical basis of zinc physiology. Physiol Rev 73(1) (1993): 79-118.

[84] Cuajungco, M.P. and Lees, G.J. Zinc and Alzheimer's disease: is there a direct link? Brain Res Brain Res Rev 23(3) (1997): 219-36.

[85] Bush, A.I. The metallobiology of Alzheimer's disease. Trends Neurosci 26(4) (2003): 207-14.

[86] Bush, A.I. Metals and neuroscience. Curr Opin Chem Biol 4(2) (2000): 184-91.

[87] Voegelin, A., Pfister, S., Scheinost, A.C., Marcus, M.A., and Kretzschmar, R. Changes in Zinc Speciation in Field Soil after Contamination with Zinc Oxide. Environmental Science & Technology 39(17) (2005): 6616-6623.

[88] Callender, E. and Rice, K.C. The Urban Environmental Gradient: Anthropogenic Influences on the Spatial and Temporal Distributions of Lead and Zinc in Sediments. Environmental Science & Technology 34(2) (2000): 232-238.

[89] Becker, J.S., Zoriy, M., Pickhardt, C., Przybylski, M., and Becker, J.S. Investigation of Cu-, Zn- and Fe-containing human brain proteins using

isotopic-enriched tracers by LA-ICP-MS and MALDI-FT-ICR-MS. <u>International Journal of Mass Spectrometry</u> 242(2–3) (2005): 135-144.

[90]   Chen, J. and Teo, K.C. Determination of cadmium, copper, lead and zinc in water samples by flame atomic absorption spectrometry after cloud point extraction. <u>Analytica Chimica Acta</u> 450(1–2) (2001): 215-222.

[91]   Binet, M.R.B., Ma, R., McLeod, C.W., and Poole, R.K. Detection and characterization of zinc- and cadmium-binding proteins in Escherichia coli by gel electrophoresis and laser ablation-inductively coupled plasma-mass spectrometry. <u>Analytical Biochemistry</u> 318(1) (2003): 30-38.

[92]   Li, Z., Yang, G., Wang, B., Jiang, C., and Yin, J. Determination of transition metal ions in tobacco as their 2-(2-quinolinylazo)-5-dimethylaminophenol derivatives using reversed-phase liquid chromatography with UV–VIS detection. <u>Journal of Chromatography A</u> 971(1–2) (2002): 243-248.

[93]   Pradhan, A.B., et al. A highly selective fluorescent sensor for zinc ion based on quinoline platform with potential applications for cell imaging studies. <u>Polyhedron</u> 94 (2015): 75-82.

[94]   Sarkar, D., Pramanik, A., Jana, S., Karmakar, P., and Mondal, T.K. Quinoline based reversible fluorescent 'turn-on' chemosensor for the selective detection of Zn2+: Application in living cell imaging and as INHIBIT logic gate. <u>Sensors and Actuators B: Chemical</u> 209 (2015): 138-146.

[95]   Hirano, T., Kikuchi, K., Urano, Y., and Nagano, T. Improvement and Biological Applications of Fluorescent Probes for Zinc, ZnAFs. <u>Journal of the American Chemical Society</u> 124(23) (2002): 6555-6562.

[96]   Walkup, G.K., Burdette, S.C., Lippard, S.J., and Tsien, R.Y. A New Cell-Permeable Fluorescent Probe for Zn2+. <u>Journal of the American Chemical Society</u> 122(23) (2000): 5644-5645.

[97]   Komatsu, K., Urano, Y., Kojima, H., and Nagano, T. Development of an Iminocoumarin-Based Zinc Sensor Suitable for Ratiometric Fluorescence Imaging of Neuronal Zinc. <u>Journal of the American Chemical Society</u> 129(44) (2007): 13447-13454.

[98]   Xu, Z., Liu, X., Pan, J., and Spring, D.R. Coumarin-derived transformable
         fluorescent sensor for Zn2+. Chemical Communications 48(39) (2012): 4764-
         4766.

[99]   Xu, Z., et al. Zn2+-Triggered Amide Tautomerization Produces a Highly Zn2+-
         Selective, Cell-Permeable, and Ratiometric Fluorescent Sensor. Journal of the
         American Chemical Society 132(2) (2010): 601-610.

[100]   Lu, X., et al. Near-IR Core-Substituted Naphthalenediimide Fluorescent
         Chemosensors for Zinc Ions: Ligand Effects on PET and ICT Channels.
         Chemistry – A European Journal 16(28) (2010): 8355-8364.

[101]   Wu, Y., et al. Boron dipyrromethene fluorophore based fluorescence sensor
         for the selective imaging of Zn(ii) in living cells. Organic & Biomolecular
         Chemistry 3(8) (2005): 1387-1392.

[102]   Cao, J., Zhao, C., Wang, X., Zhang, Y., and Zhu, W. Target-triggered
         deprotonation of 6-hydroxyindole-based BODIPY: specially switch on NIR
         fluorescence upon selectively binding to Zn2+. Chemical Communications
         48(79) (2012): 9897-9899.

[103]   Guo, Z., Kim, G.-H., Shin, I., and Yoon, J. A cyanine-based fluorescent sensor
         for detecting endogenous zinc ions in live cells and organisms. Biomaterials
         33(31) (2012): 7818-7827.

[104]   Wang, F., et al. Zn2+-induced conformational changes in a binaphthyl-pyrene
         derivative monitored by using fluorescence and CD spectroscopy. Chemical
         Communications 49(65) (2013): 7228-7230.

[105]   Lee, H.G., et al. Zinc selective chemosensors based on the flexible
         dipicolylamine and quinoline. Inorganica Chimica Acta 394 (2013): 542-551.

[106]   Goswami, S., Sen, D., Das, N.K., Fun, H.-K., and Quah, C.K. A new rhodamine
         based colorimetric 'off-on' fluorescence sensor selective for Pd2+ along with
         the first bound X-ray crystal structure. Chemical Communications 47(32)
         (2011): 9101-9103.

[107]   Hurley, R. and Testa, A.C. Triplet-state yield of aromatic nitro compounds.
         Journal of the American Chemical Society 90(8) (1968): 1949-1952.

[108]   Persiani, S., Roda, E., Rovati, L.C., Locatelli, M., Giacovelli, G., and Roda, A. Glucosamine oral bioavailability and plasma pharmacokinetics after increasing doses of crystalline glucosamine sulfate in man. Osteoarthritis and Cartilage 13(12) (2005): 1041-1049.

[109]   Qian, S., et al. Bioavailability enhancement of glucosamine hydrochloride by chitosan. International Journal of Pharmaceutics 455(1–2) (2013): 365-373.

[110]   Simon-Assmann, P., Turck, N., Sidhoum-Jenny, M., Gradwohl, G., and Kedinger, M. In vitro models of intestinal epithelial cell differentiation. Cell Biol Toxicol 23(4) (2007): 241-56.

[111]   Shah, P., Jogani, V., Bagchi, T., and Misra, A. Role of Caco-2 cell monolayers in prediction of intestinal drug absorption. Biotechnol Prog 22(1) (2006): 186-98.

[112]   Press, B. and Di Grandi, D. Permeability for intestinal absorption: Caco-2 assay and related issues. Curr Drug Metab 9(9) (2008): 893-900.

[113]   Meulyzer, M., et al. Comparison of pharmacokinetics of glucosamine and synovial fluid levels following administration of glucosamine sulphate or glucosamine hydrochloride. Osteoarthritis Cartilage 16(9) (2008): 973-9.

[114]   Han, J. and Burgess, K. Fluorescent indicators for intracellular pH. Chem Rev 110(5) (2010): 2709-28.

[115]   Vendrell, M., Zhai, D., Er, J.C., and Chang, Y.T. Combinatorial strategies in fluorescent probe development. Chem Rev 112(8) (2012): 4391-420.

[116]   Carter, K.P., Young, A.M., and Palmer, A.E. Fluorescent sensors for measuring metal ions in living systems. Chem Rev 114(8) (2014): 4564-601.

[117]   Yao, J., Yang, M., and Duan, Y. Chemistry, biology, and medicine of fluorescent nanomaterials and related systems: new insights into biosensing, bioimaging, genomics, diagnostics, and therapy. Chem Rev 114(12) (2014): 6130-78.

[118]   Xu, L., He, M.-L., Yang, H.-B., and Qian, X. A simple fluorescent probe for Cd2+ in aqueous solution with high selectivity and sensitivity. Dalton Transactions 42(23) (2013): 8218-8222.

[119]   Xu, L., Xu, Y., Zhu, W., Sun, X., Xu, Z., and Qian, X. Modulating the selectivity by switching sensing media: a bifunctional chemosensor selectivity for Cd2+

and Pb2+ in different aqueous solutions. RSC Advances 2(15) (2012): 6323-6328.

[120] Hanaoka, K., Kikuchi, K., Kojima, H., Urano, Y., and Nagano, T. Development of a zinc ion-selective luminescent lanthanide chemosensor for biological applications. J Am Chem Soc 126(39) (2004): 12470-6.

[121] Meng, X., Wang, S., Li, Y., Zhu, M., and Guo, Q. 6-Substituted quinoline-based ratiometric two-photon fluorescent probes for biological Zn2+ detection. Chemical Communications 48(35) (2012): 4196-4198.

[122] Kim, J.H., et al. Zinc sensors with lower binding affinities for cellular imaging. Dalton Transactions 42(15) (2013): 5500-5507.

[123] Jiang, P. and Guo, Z. Fluorescent detection of zinc in biological systems: recent development on the design of chemosensors and biosensors. Coordination Chemistry Reviews 248(1–2) (2004): 205-229.

[124] Zhou, X., Yu, B., Guo, Y., Tang, X., Zhang, H., and Liu, W. Both Visual and Fluorescent Sensor for Zn2+ Based on Quinoline Platform. Inorganic Chemistry 49(9) (2010): 4002-4007.

[125] Zhang, N., Chen, Y., Yu, M., and Liu, Y. Benzenesulfonamidoquinolino-beta-cyclodextrin as a cell-impermeable fluorescent sensor for Zn2+. Chem Asian J 4(11) (2009): 1697-702.

[126] Chen, X.-Y., et al. Two-Photon Fluorescent Probes of Biological Zn(II) Derived from 7-Hydroxyquinoline. Organic Letters 11(19) (2009): 4426-4429.
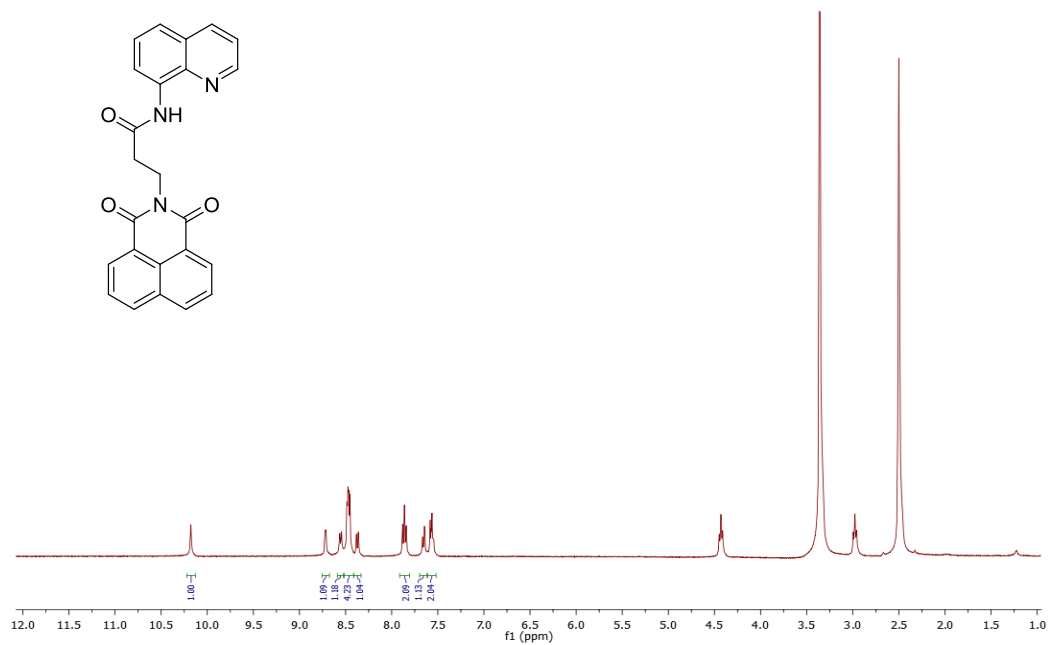
Figure A.1 ^{1}H NMR spectrum of **A1** in DMSO-d$_6$
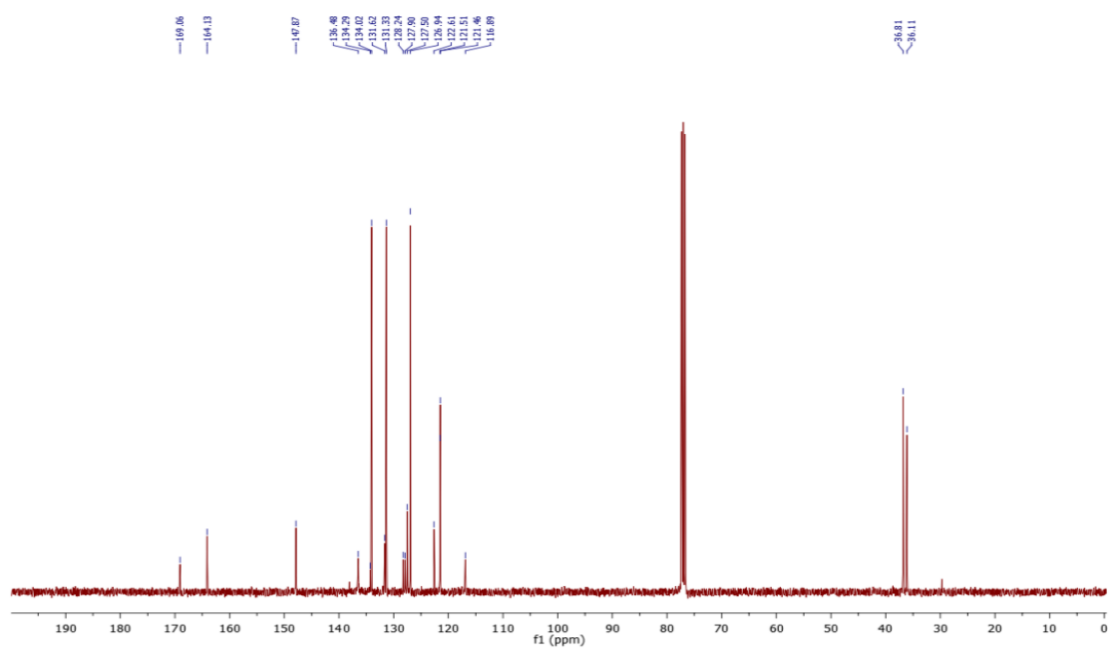
Figure A.2 ^{13}C NMR spectrum of **A1** in CDCl$_3$
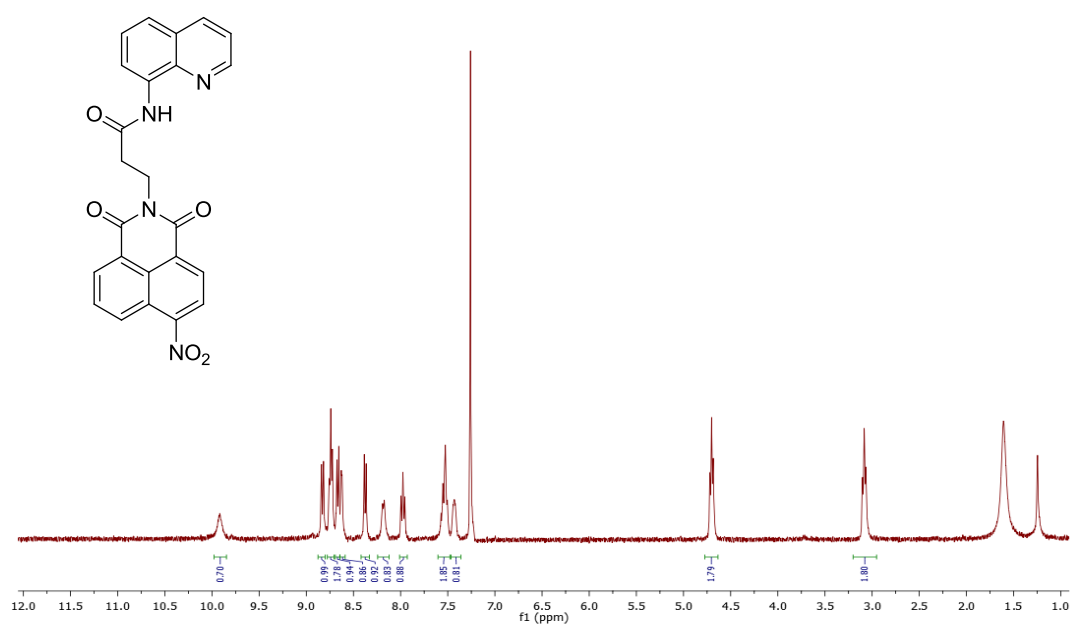
Figure A.3 ^{1}H NMR spectrum of **A2** in CDCl$_3$
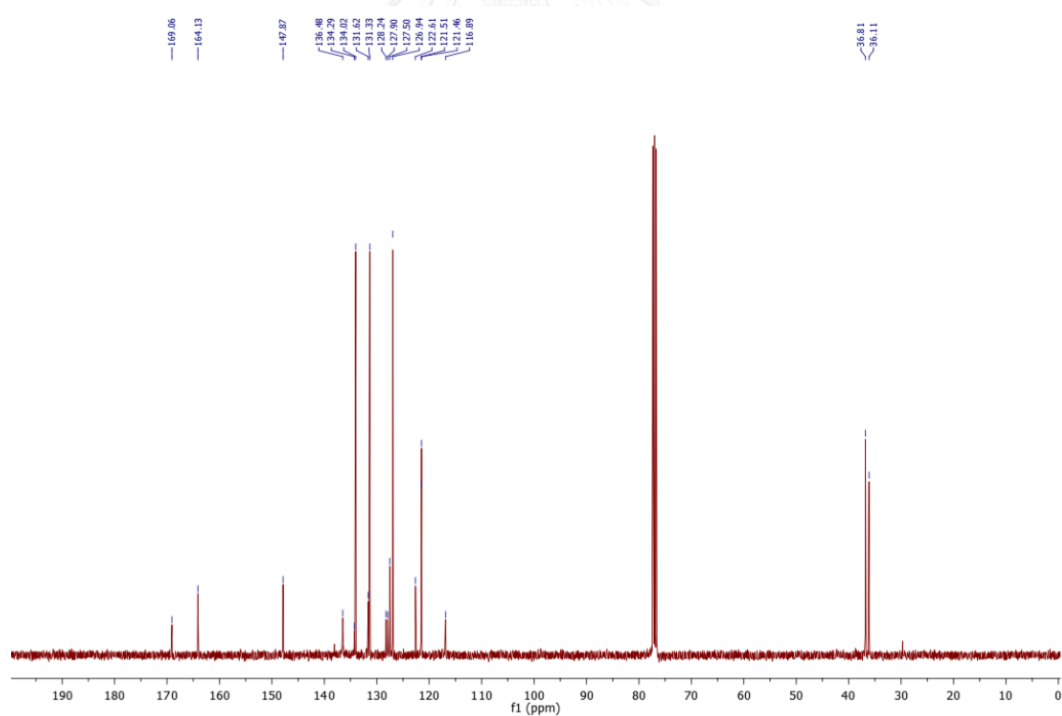
Figure A.4 ^{13}C NMR spectrum of **A2** in CDCl$_3$
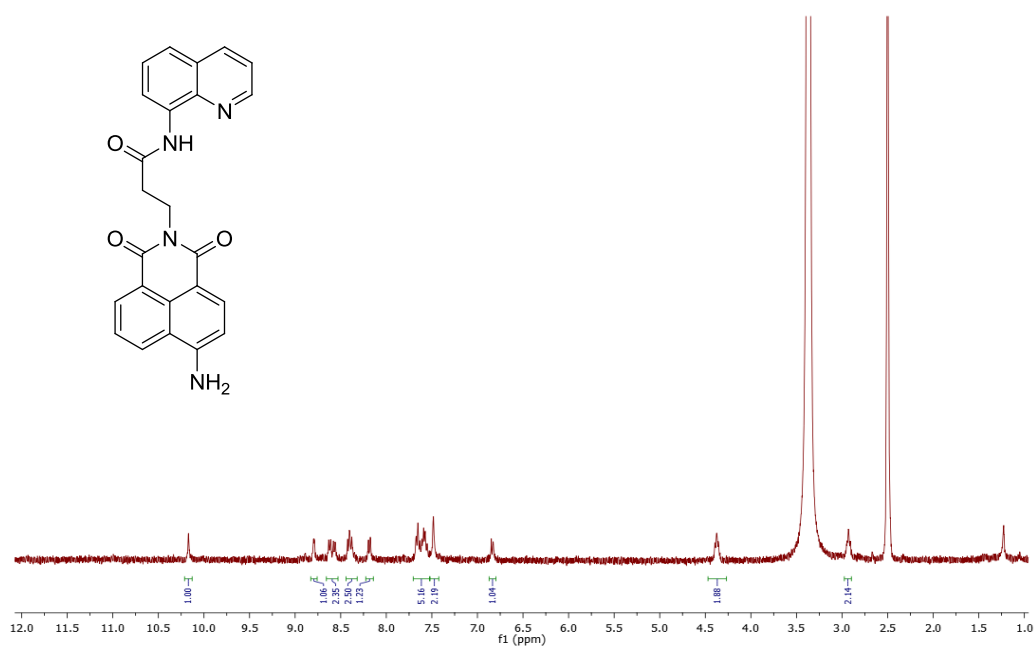
Figure A.5 ^{1}H NMR spectrum of **A3** in DMSO-d$_6$
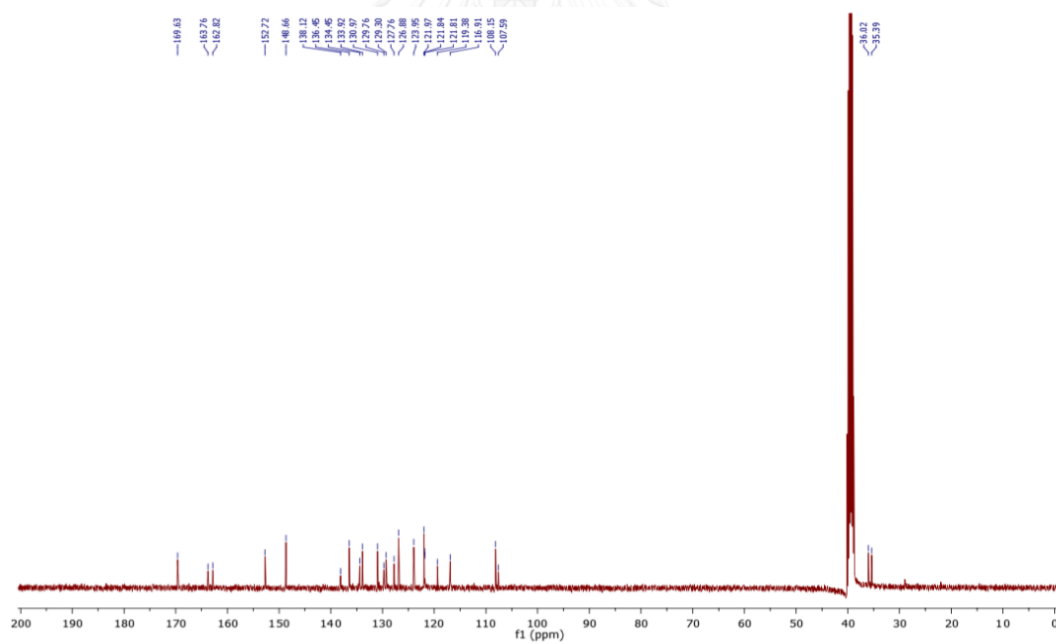
Figure A.6 ^{13}C NMR spectrum of **A3** in DMSO-d$_6$
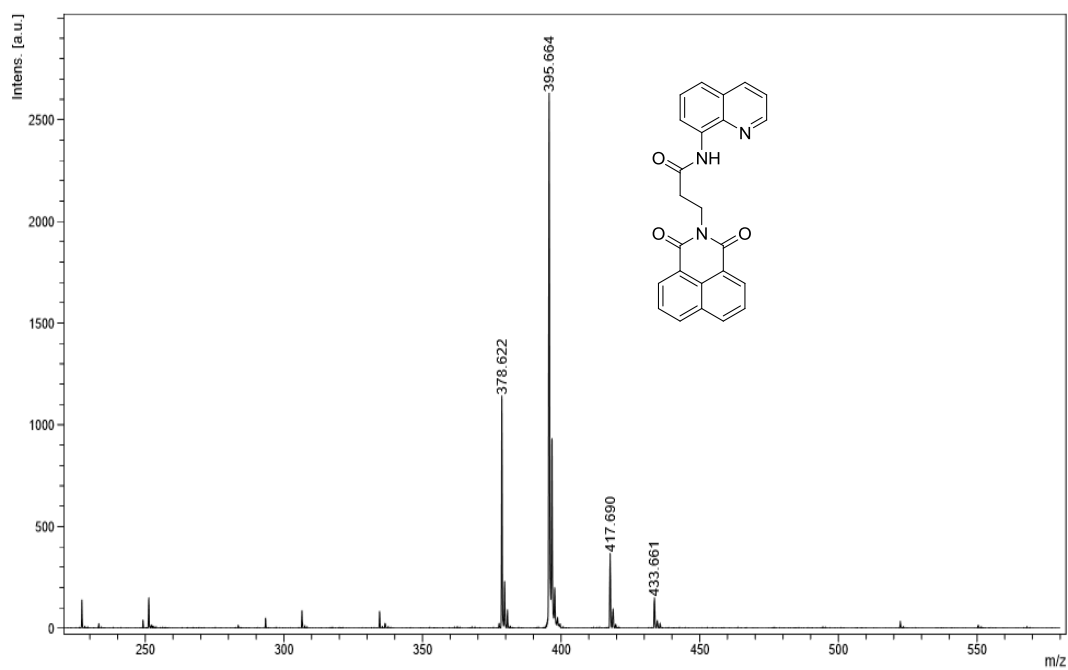
Figure A.7 MALDI-TOF-Mass spectrum of **A1**
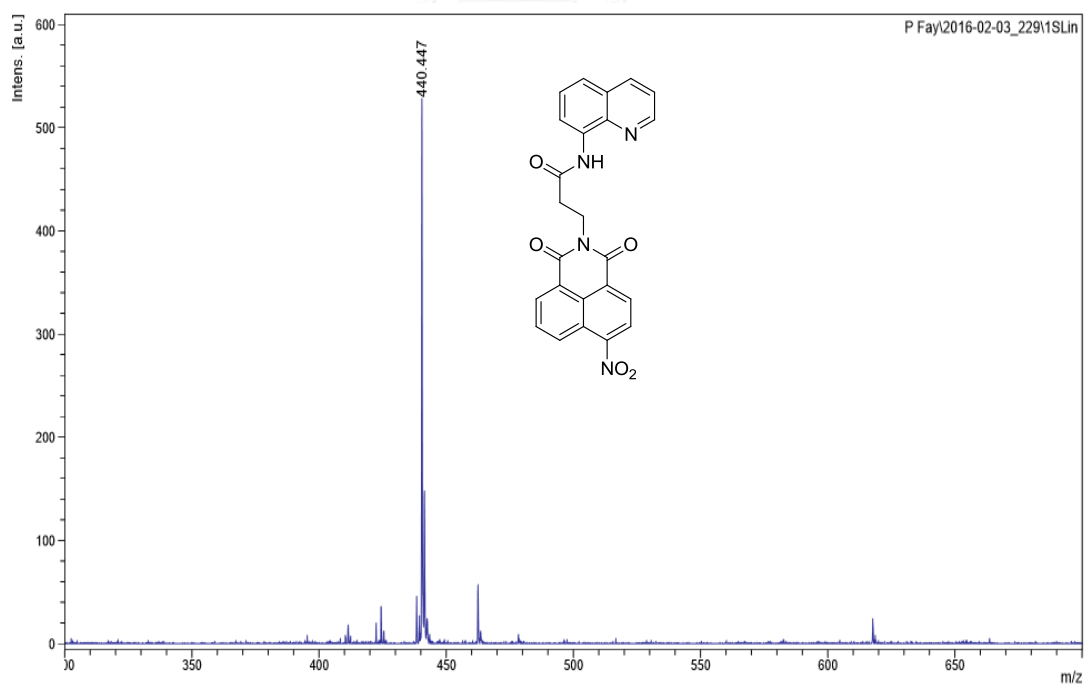
Figure A.8 MALDI-TOF-Mass spectrum of **A2**
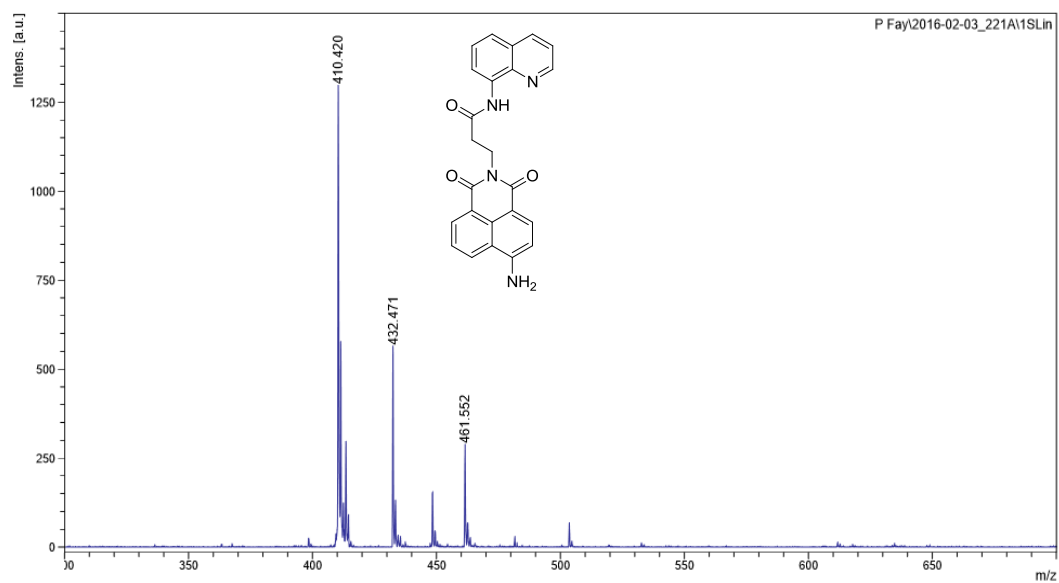
Figure A.9 MALDI-TOF-Mass spectrum of **A3**
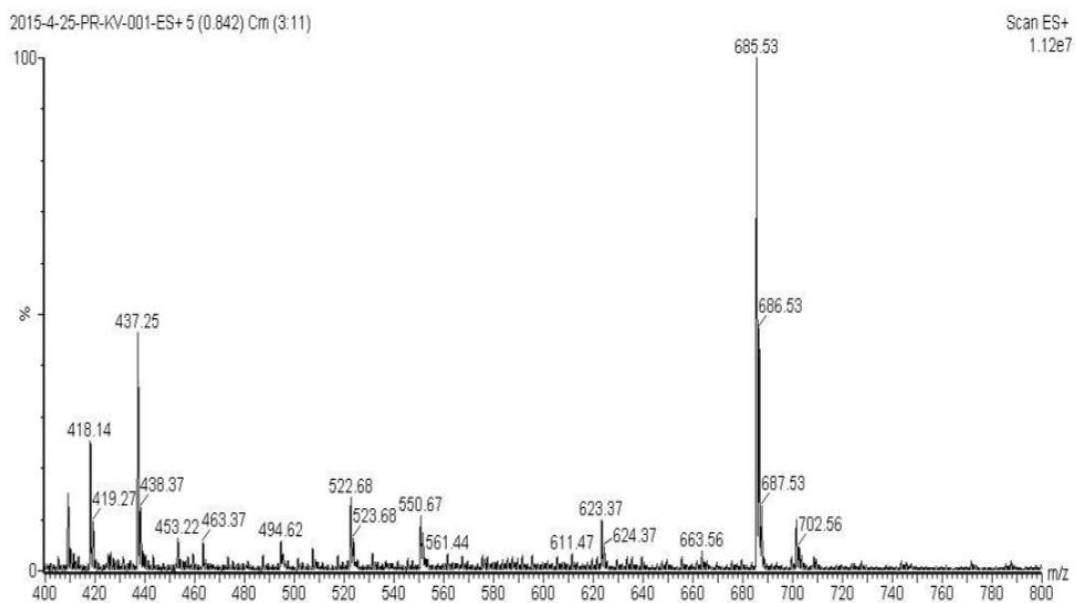
Figure A.10 ESI-Mass spectrum of **A1**-glucosamine complex

Table A.1 Electrochemical properties of amidoquinoline A and compounds **A1-A3**

	E^a_{ox} (V)	E_g^b (eV)	HOMO^c (eV)	LUMO^d (eV)
A	0.39	3.14	-5.10	-1.96
A1	0.69	3.37	-5.40	-2.03
A2	0.74	3.13	-5.45	-2.32
A3	0.36	2.53	-5.07	-2.54

^{a}Onset oxidation potential obtained from linear sweep voltammogram;

^{b}HOMO-LUMO energy gap estimated from the onset absorption wavelength using a formula: $E_g = 1242/\lambda$onset;

^{c}HOMO energy level calculated from Eox using a formula: HOMO = $-$ (E_{ox} + $E_{FC/FC+}$) where $E_{FC/FC+}$ is the corrected oxidation potential of ferrocene (4.71 eV);

^{d}LUMO energy level calculated using a formula: LUMO = HOMO + E_g.

Figure A.11 ^{1}H NMR spectrum of **2a** in acetone-d$_6$
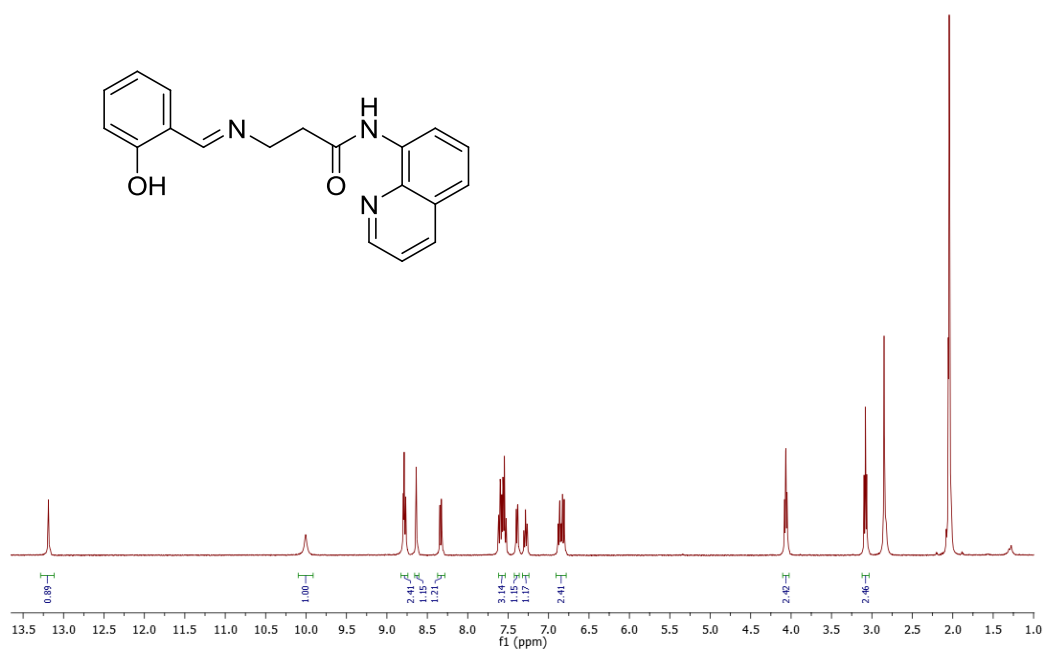
Figure A.12 ^{1}H NMR spectrum of **B1** in acetone-d$_6$
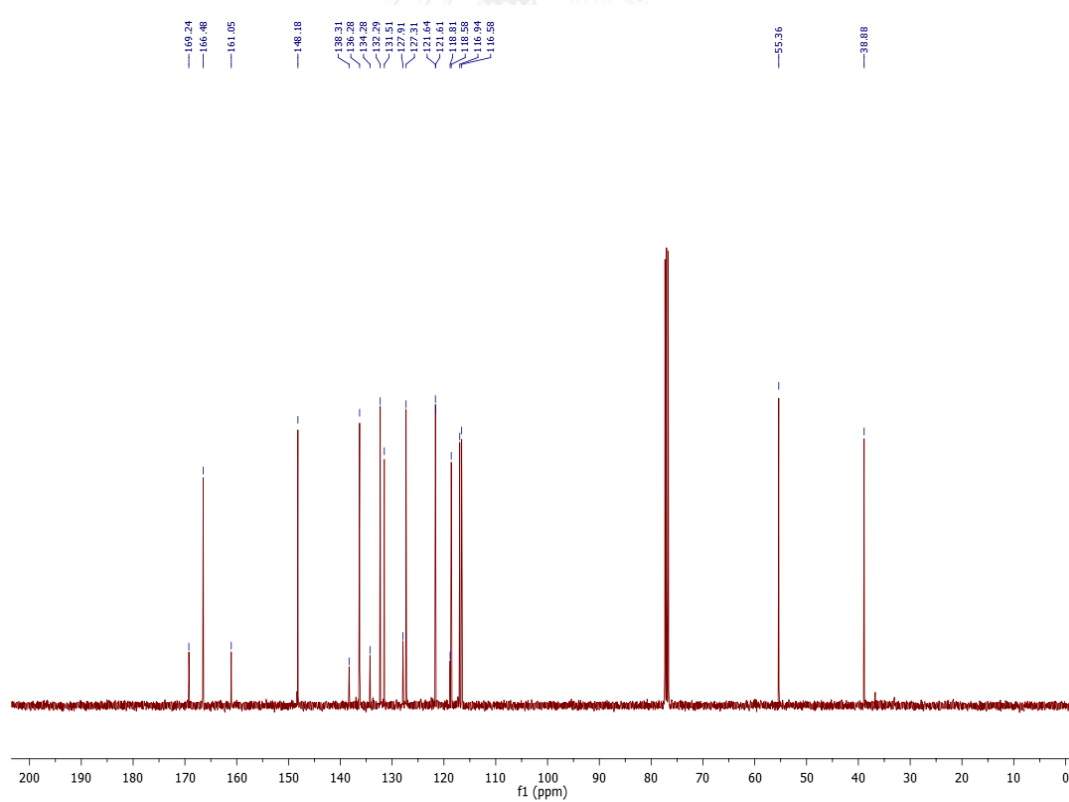
Figure A.13 ^{13}C NMR spectrum of **B1** in CDCl$_3$
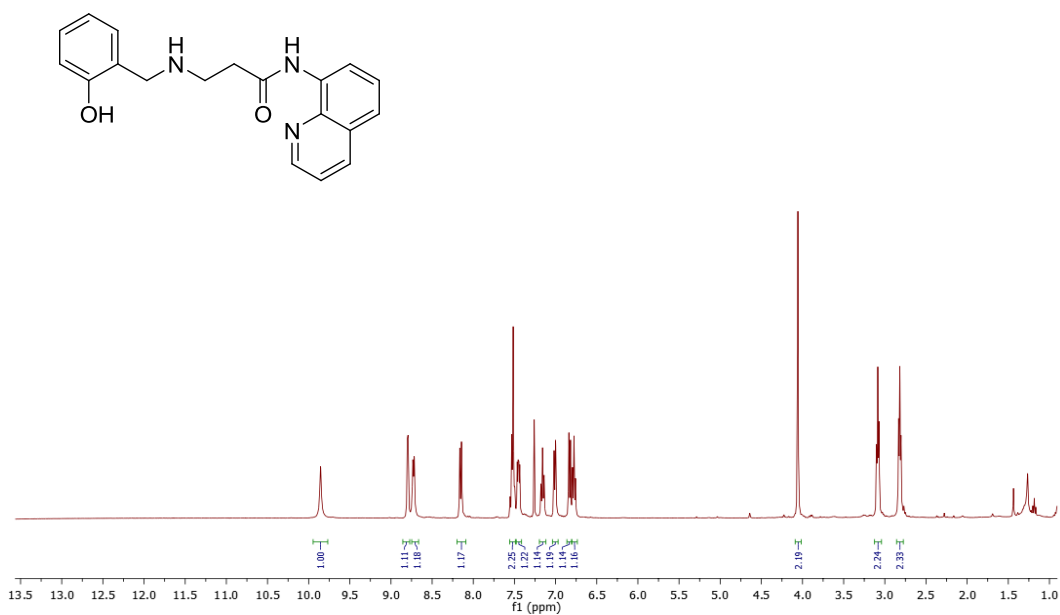
Figure A.14 ^{1}H NMR spectrum of **B2** in CDCl$_3$
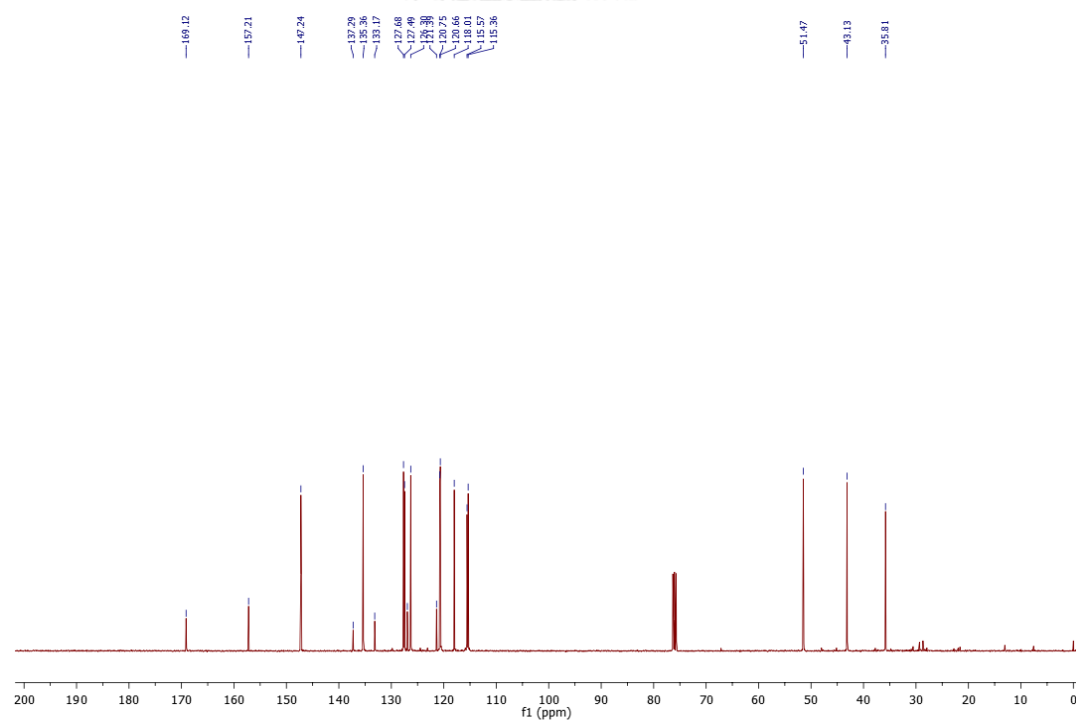
Figure A.15 ^{13}C NMR spectrum of **B2** in CDCl$_3$
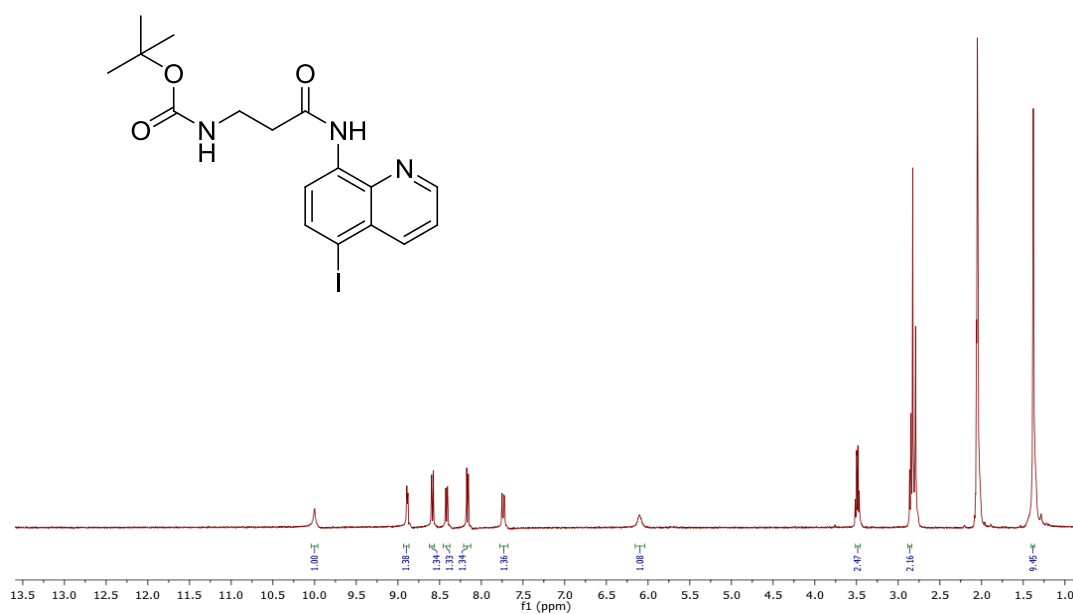
Figure A.16 ^{1}H NMR spectrum of **2A** in acetone-d[6]
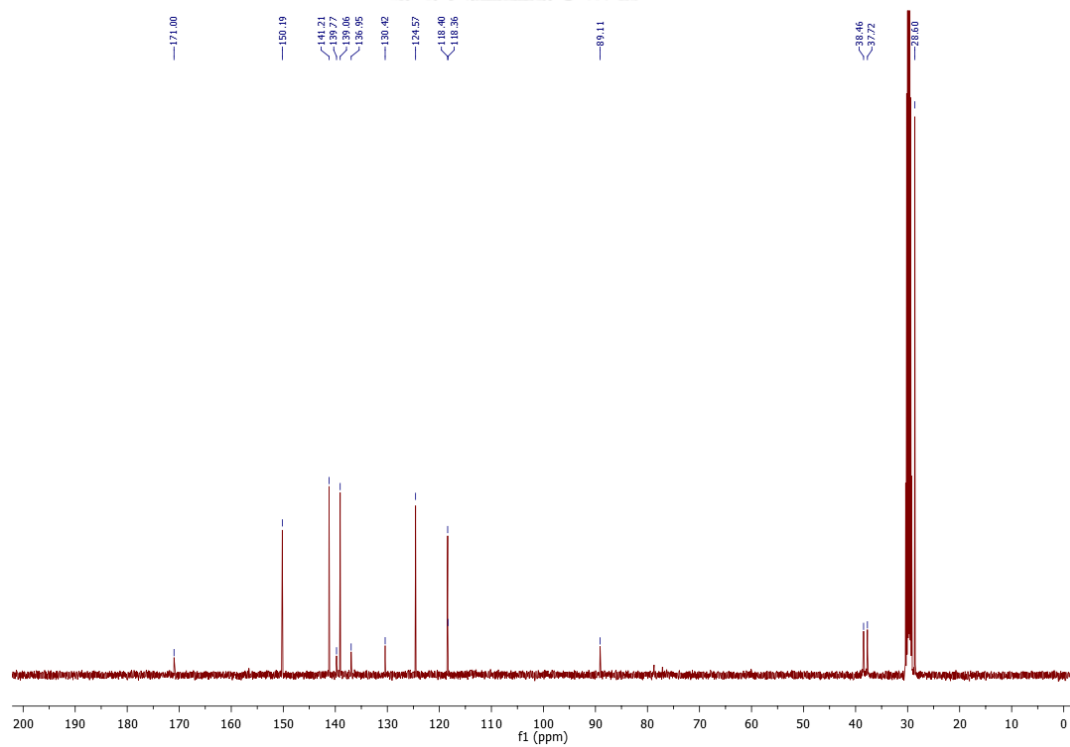
Figure A.17 ^{13}C NMR spectrum of **2A** in acetone-d[6]
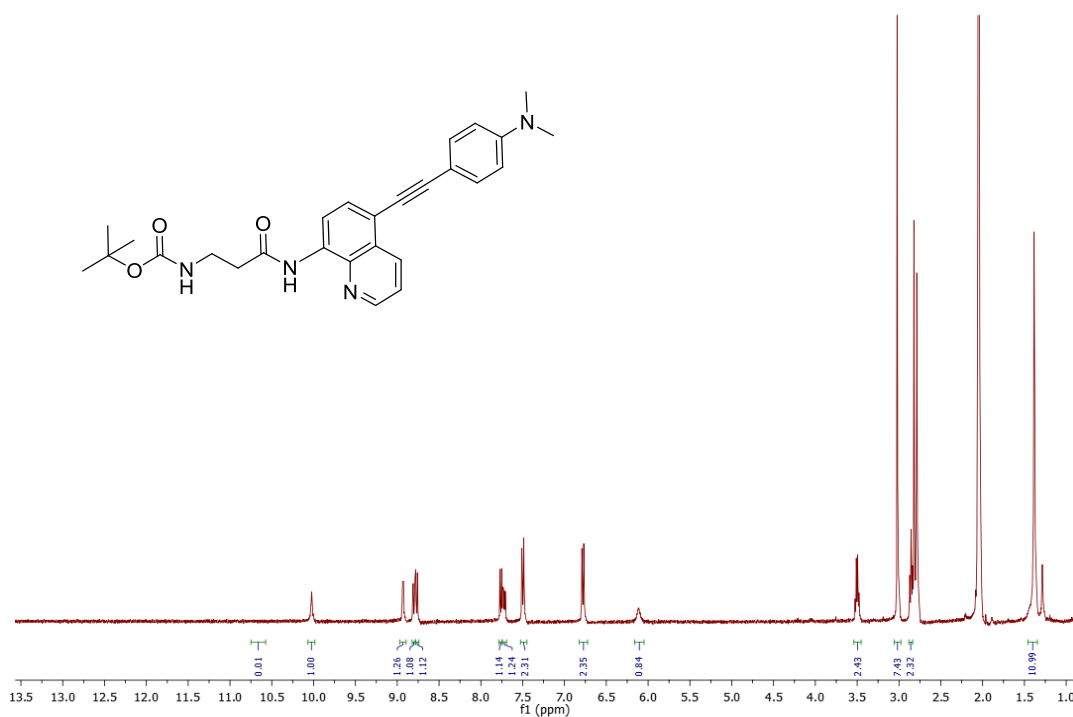
Figure A.18 ^{1}H NMR spectrum of **3a** in acetone-d$_6$
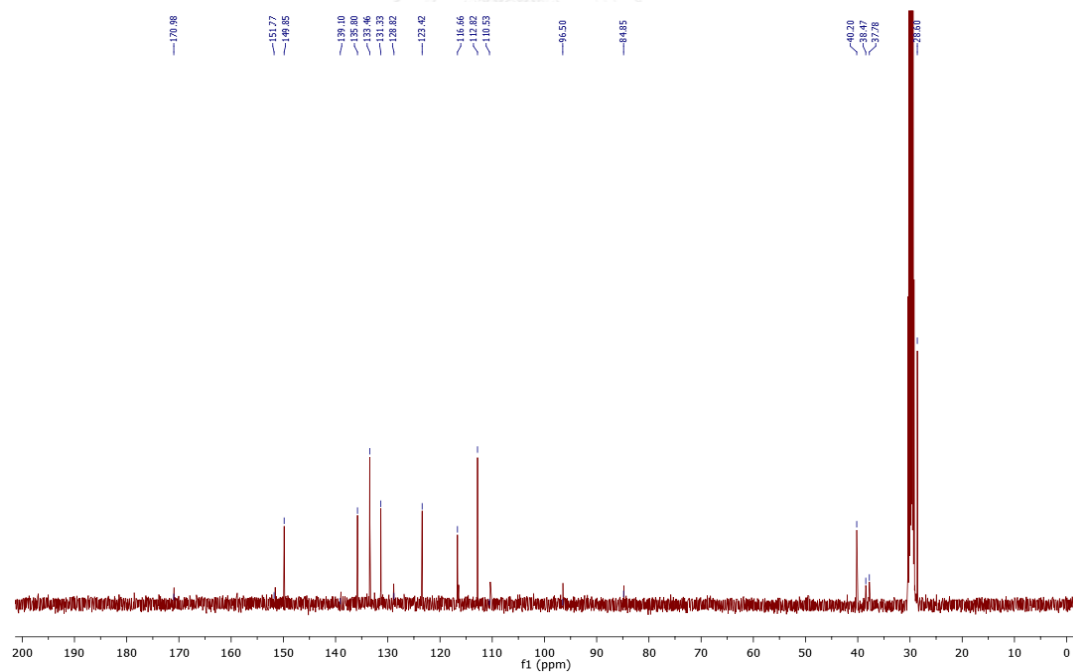
Figure A.19 ^{13}C NMR spectrum of **3a** in acetone-d$_6$
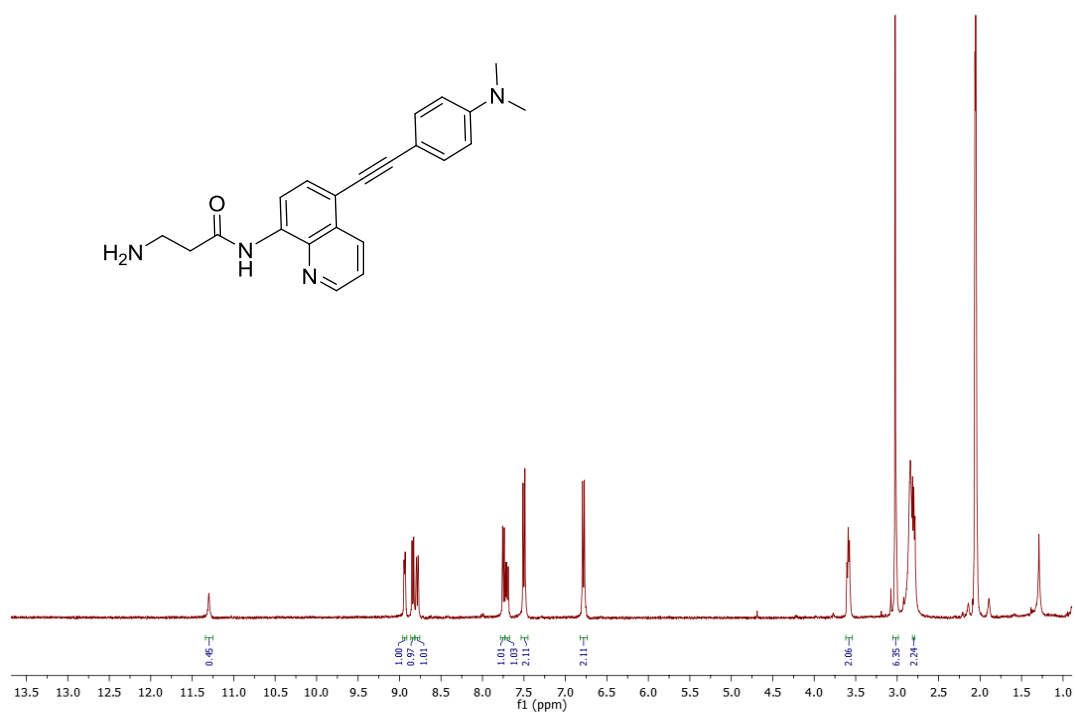
Figure A.20 ^{1}H NMR spectrum of **3A** in acetone-d$_{6}$
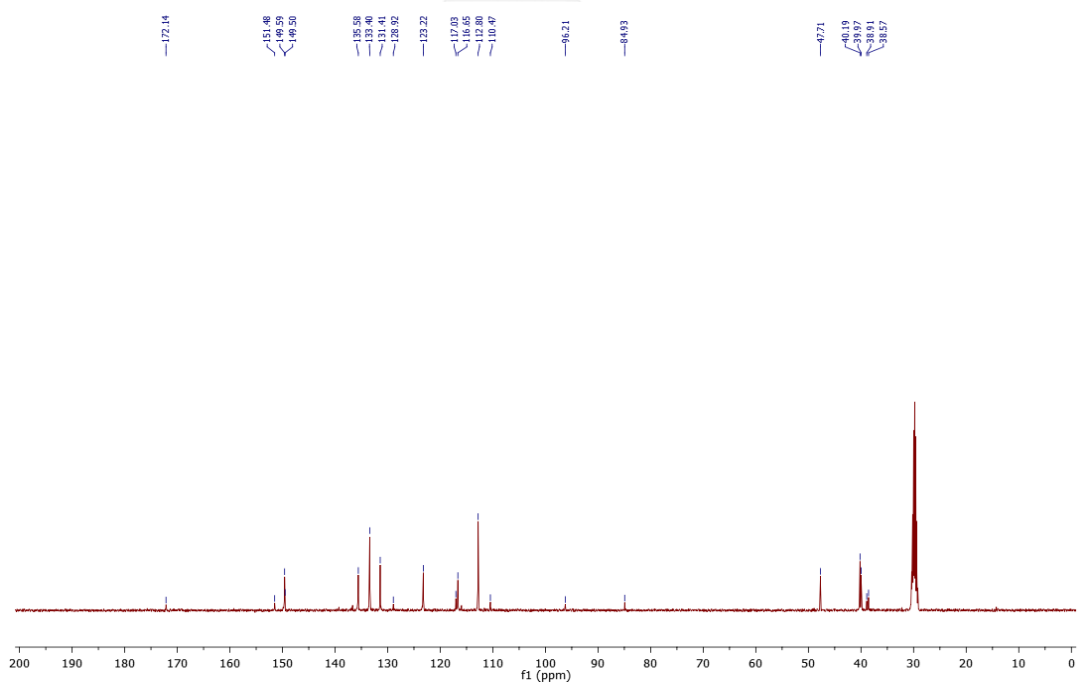
Figure A.21 ^{13}C NMR spectrum of **3A** in acetone-d$_{6}$
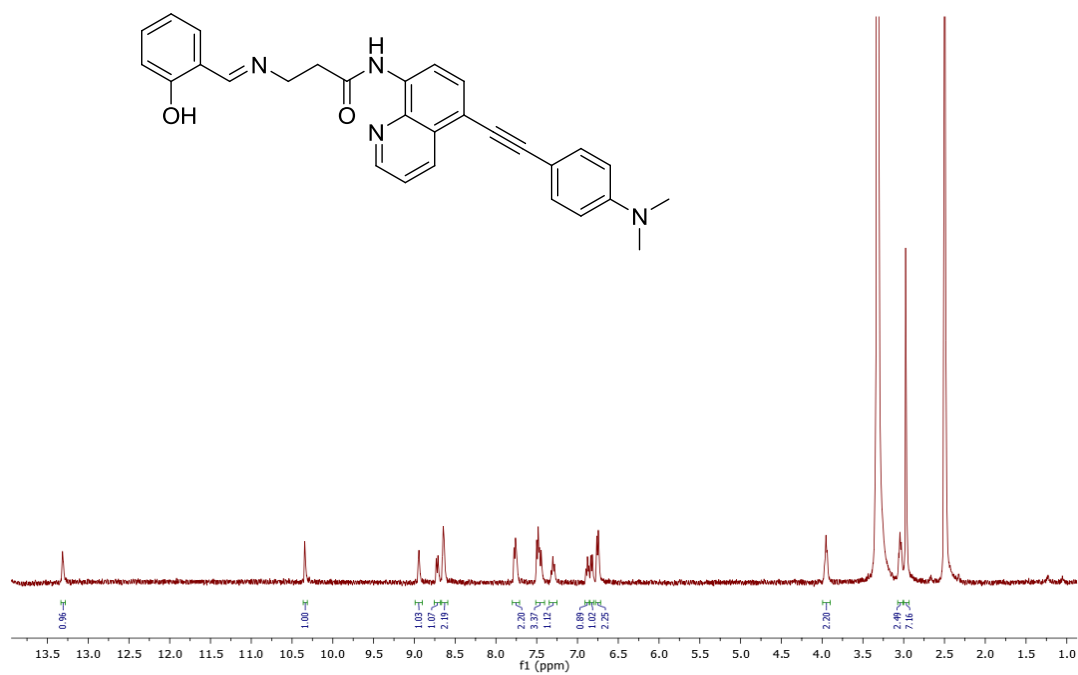
Figure A.22 ^{1}H NMR spectrum of **B3** in DMSO-d$_6$
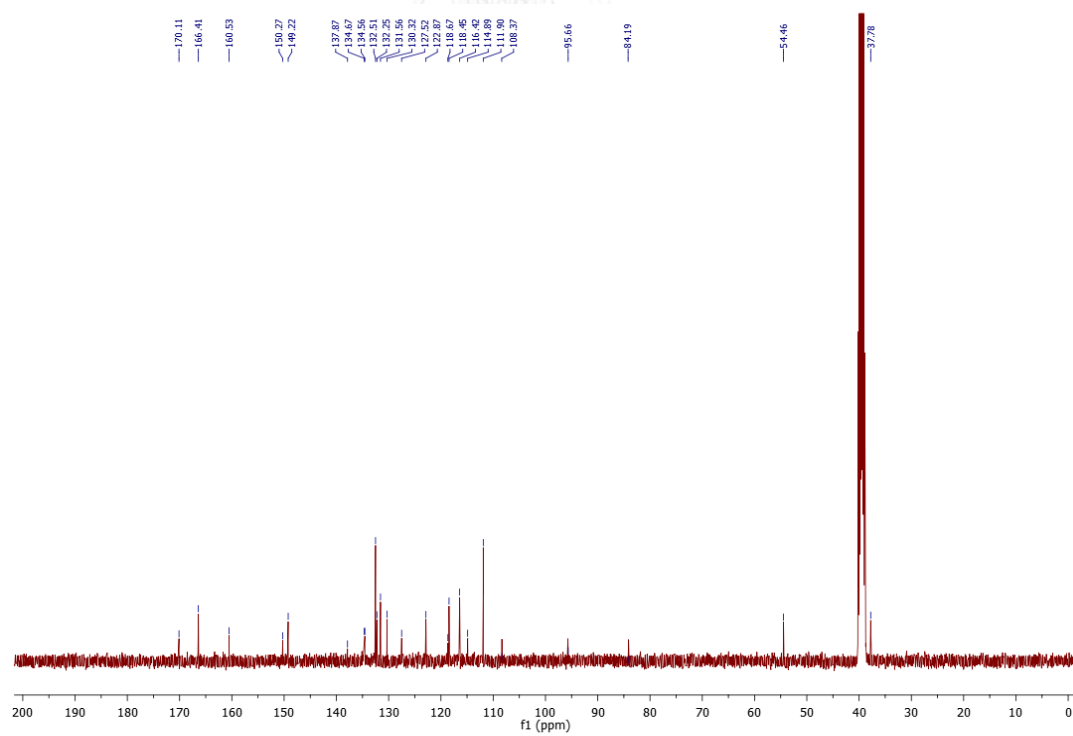
Figure A.23 ^{13}C NMR spectrum of **B3** in DMSO-d$_6$
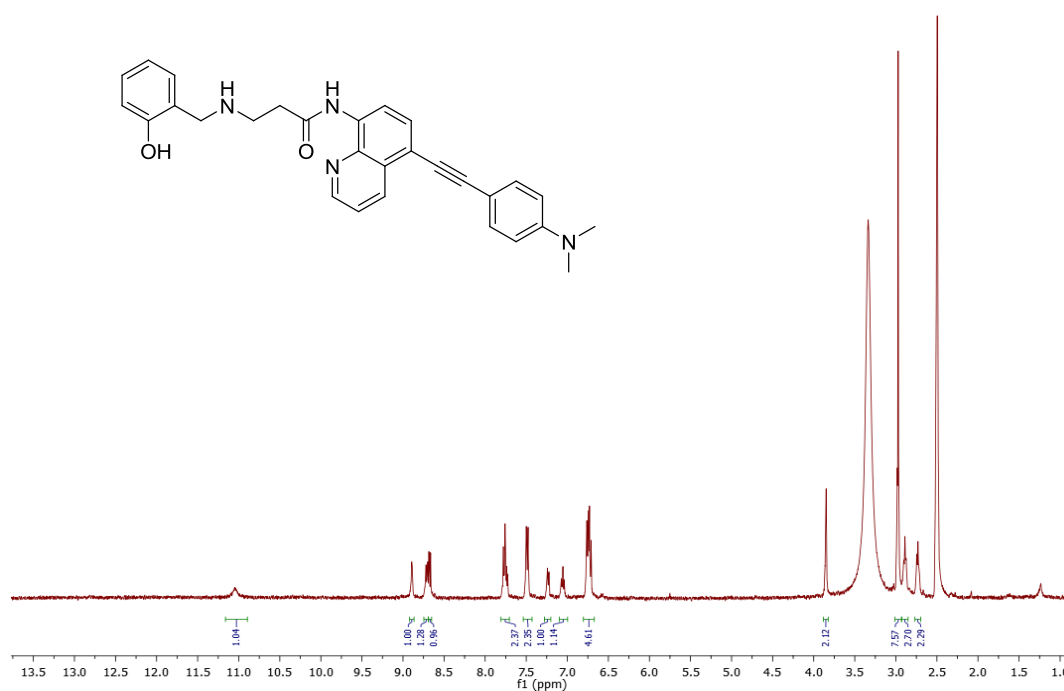
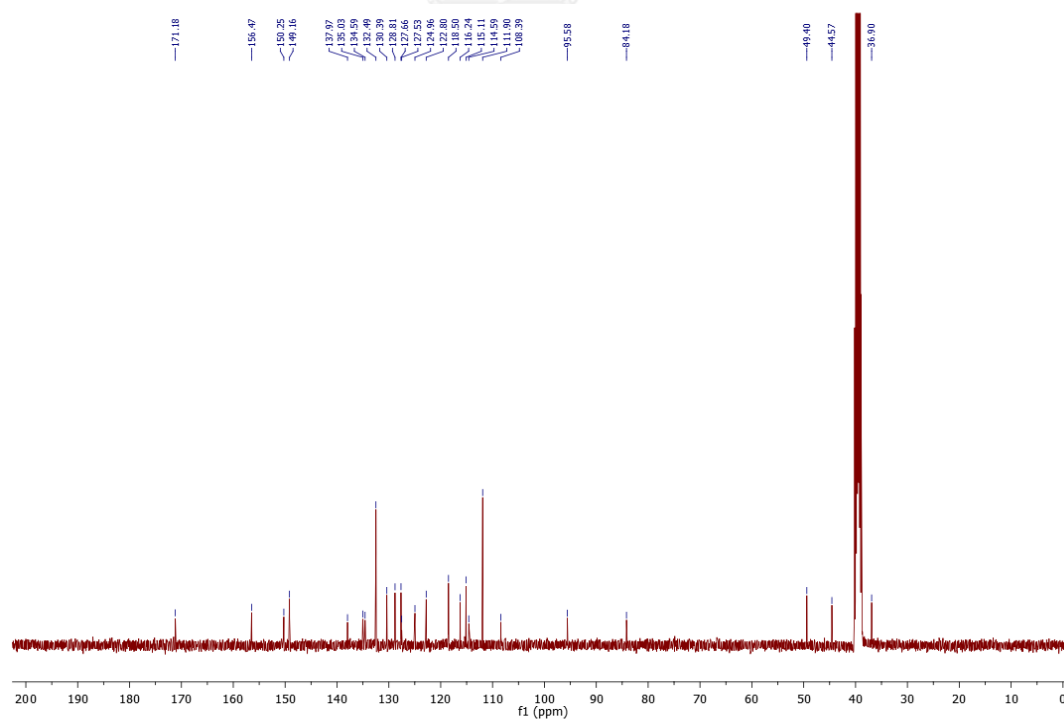**Figure A.24** ^{1}H NMR spectrum of **B4** in DMSO-d[6]

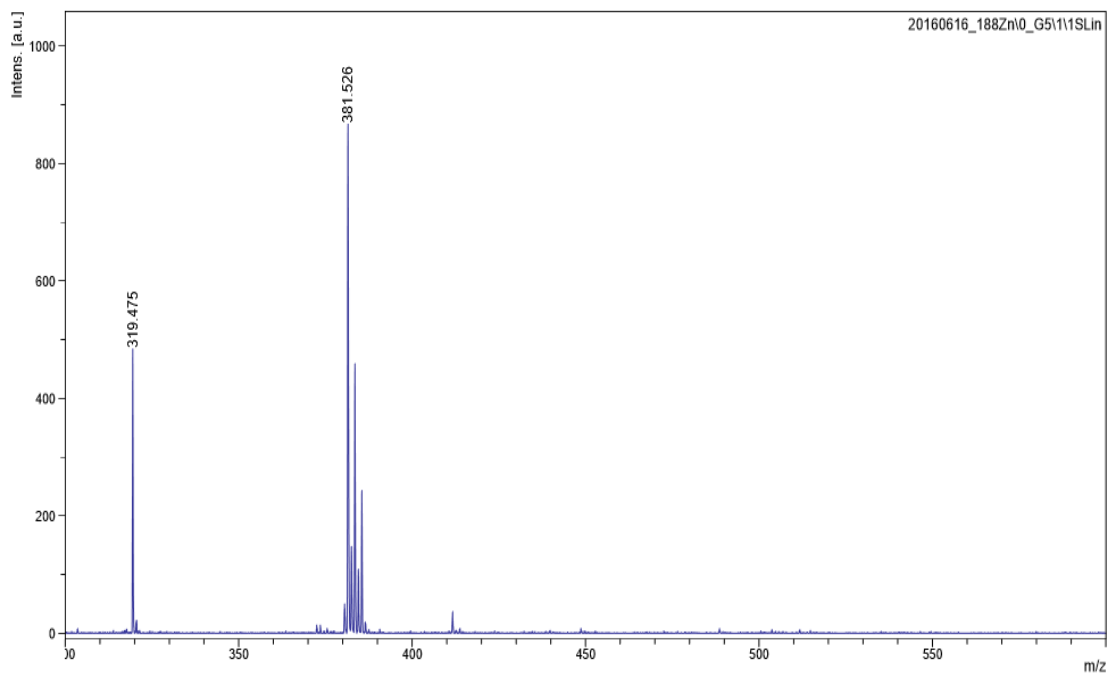**Figure A.25** ^{13}C NMR spectrum of **B4** in DMSO-d[6]

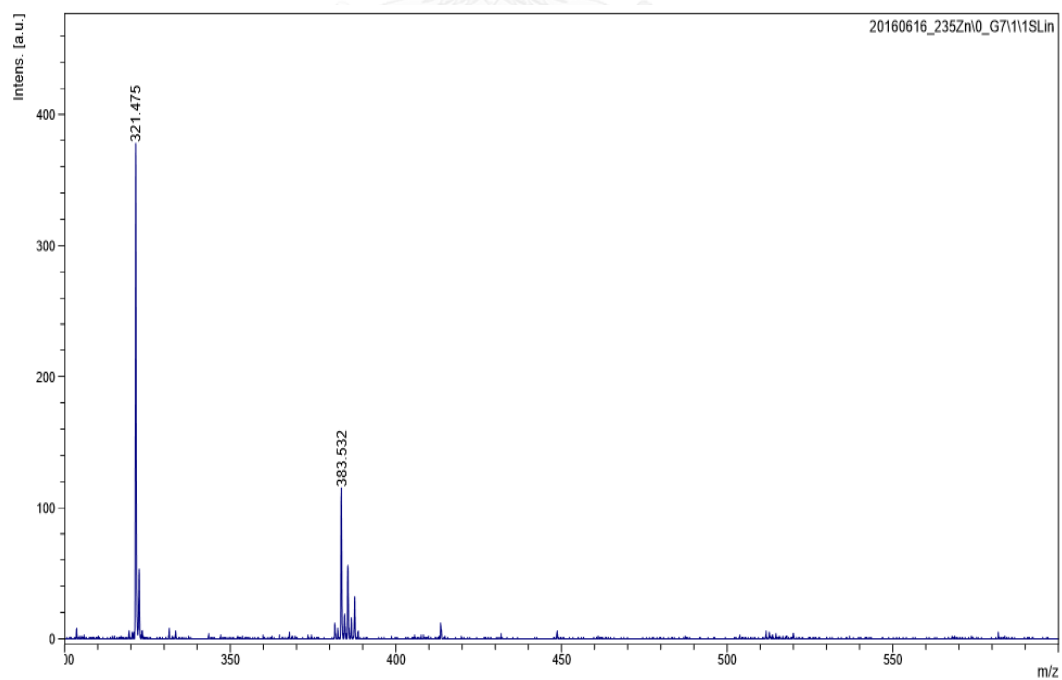**Figure A.26** MALDI-TOF-Mass spectrum of **B1**-Zn complex

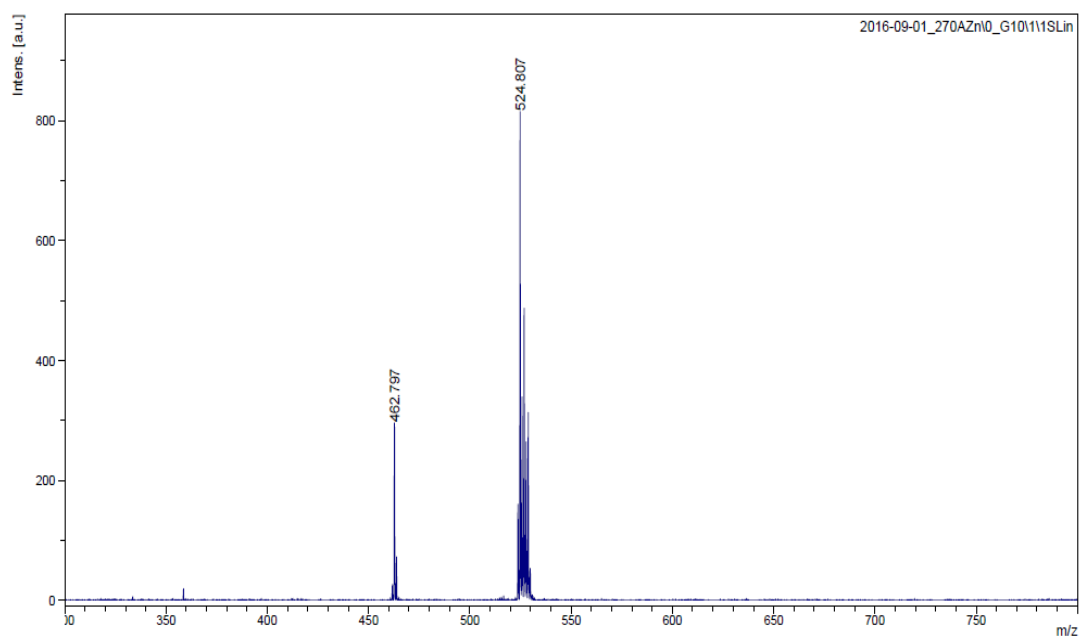**Figure A.27** MALDI-TOF-Mass spectrum of **B2**-Zn complex

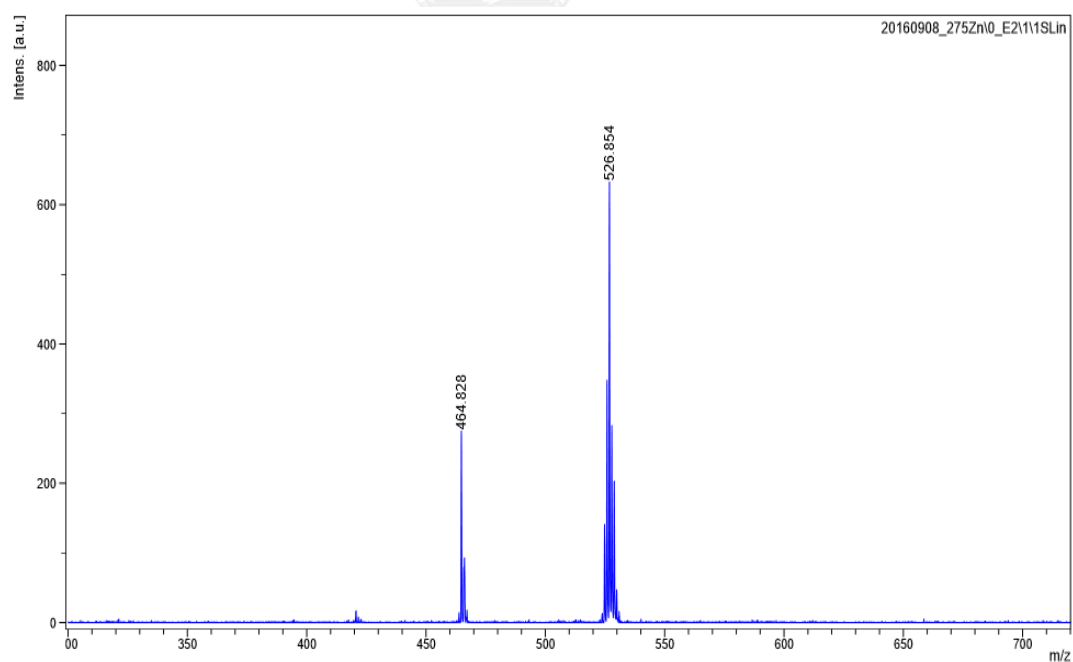**Figure A.28** MALDI-TOF-Mass spectrum of **B3**-Zn complex

Figure A.29 MALDI-TOF-Mass spectrum of **B4**-Zn complex

APPENDIX B

PUBLICATIONS

- Vongnam, K., Muangnoi, C., Rojsitthisak, P., Sukwattanasinitt, M., and Rashatasakhon, P. A highly selective turn-on fluorescent sensor for glucosamine from amidoquinoline-napthalimide dyads. Biosens Bioelectron 86 (2016): 472-476.

จุฬาลงกรณ์มหาวิทยาลัย
CHULALONGKORN UNIVERSITY

VITA

Miss Kunnigar Vongnam was born on November 30th, 1983 in Udonthani, Thailand. She received a Bachelor's Degree of Science, majoring in Chemistry from Faculty of Science, Silpakorn University in 2006. In 2011, she further received a Master Degree in Petrochemical and Polymer Science program, Chulalongkorn University. Since 2013, she has been a graduate student in Petrochemistry and become a member of Material Advancement and Proficient Synthesis (MAPS) GROUP under supervision of Associate Professor Dr. Paitoon Rashatasakhon. She graduated with a Ph. D. Degree in Petrochemistry in academic year 2016. Her present address is 2 Moo 13, Polaboon Road, Kuddu, Nonsang, Nongbualamphu, Thailand 39140.